Comparative Study on Low Voltage Ride Through Techniques for Double Fed Induction Generator in Wind Energy Conversion System Under Fault Conditions

Kidist Berhane Zergaw

A Thesis Submitted to the Department of Electrical Power and Control Engineering

School of Electrical Engineering and Computing

Presented in Partial Fulfillment of the Requirement for the Degree of Master's in Electrical Power and Control Engineering

(Power System Engineering)

Office of Graduate Studies

Adama Science and Technology University

October 2022

Adama, Ethiopia

Comparative Study on Low Voltage Ride Through Techniques for Double Fed Induction Generator in Wind Energy Conversion System Under Fault Conditions

Kidist Berhane Zergaw

Advisor: Dr. Milkias Berhanu

A Thesis Submitted to the Department of Electrical Power and Control Engineering

School of Electrical Engineering and Computing

Presented in Partial Fulfillment of the Requirement for the Degree of Master's in Electrical Power and Control Engineering

(Power System Engineering)

Office of Graduate Studies

Adama Science and Technology University

October 2022

Adama, Ethiopia

DECLARATION

I hereby declare that this Master Thesis entitled "**Comparative Study on Low Voltage Ride Through Techniques for Double Fed Induction Generator in Wind Energy Conversion System Under Fault Conditions**" is my original work. That is, it has not been submitted for the award of any academic degree, diploma, or certificate in any other university. All sources of materials that are used for this thesis have been duly acknowledged through citation.

______________________	______________________	______________
Name of student	Signature	Date

RECOMMENDATION

I, the advisor of this thesis, hereby certify that I have read the revised version of the thesis entitled "**Comparative Study on Low Voltage Ride Through Techniques for Double Fed Induction Generator in Wind Energy Conversion System Under Fault Conditions**" prepared under my guidance by **Kidist Berhane Zergaw** submitted in partial fulfillment of the requirements for the degree of Masters of Science in Electrical Power and Control Engineering (Power System Engineering). Therefore, I recommend the submission of a revised version of the thesis to the department following the applicable procedures.

____________________	____________________	______________
Advisor	Signature	Date

APPROVAL PAGE

I, the advisor of the thesis entitled "**Comparative Study on Low Voltage Ride Through Techniques for Double Fed Induction Generator in Wind Energy Conversion System Under Fault Conditions**" and developed by **Kidist Berhane Zergaw**, hereby certify that the recommendation and suggestions made by the board of examiners are appropriately incorporated into the final version of the thesis.

______________________	______________________	______________
Advisor	Signature	Date

We, the undersigned, members of the Board of Examiners of the thesis by **Kidist Berhane Zergaw** have read and evaluated the thesis entitled "**Comparative Study on Low Voltage Ride Through Techniques for Double Fed Induction Generator in Wind Energy Conversion System Under Fault Conditions**" and examined the candidate during the open defense. This is, therefore, to certify that the thesis is accepted for partial fulfillment of the requirement of the degree of Master of Science in Electrical Power and Control Engineering (Power System Engineering).

______________________	______________________	______________
Chairperson	Signature	Date
______________________	______________________	______________
Internal Examiner	Signature	Date
Dr. Yeshitela Shiferaw	______________________	10/28/2022
External Examiner	Signature	Date

Finally, approval and acceptance of the thesis is contingent upon submission of its final copy to the Office of Postgraduate Studies (OPGS) through the Department Graduate Council (DGC) and School Graduate Committee (SGC).

______________________	______________________	______________
Department Head	Signature	Date
______________________	______________________	______________
School Dean	Signature	Date
______________________	______________________	______________
Office of Graduate Studies, Dean	Signature	Date

ACKNOWLEDGMENTS

First and foremost, I want to praise the Almighty God and his mother, Virgin St. Mary, for guiding me in overcoming numerous challenges to attain this goal. Then, I would like to extend my sincere gratitude to my advisor, Dr. Milkias Berhanu, for his constant guidance, invaluable assistance, helpful comments, and supervision throughout the entire process of this thesis. Along with that, I would like to thank my entire family, especially my mother, Fantaye Bogale, for her support and encouragement throughout my entire life. I am also very grateful to my friends for their insightful comments. Last but not least, I'd like to express my gratitude to Adama Science and Technology University for giving me this scholarship opportunity.

TABLES OF CONTENTS

LIST OF TABLES

LIST OF FIGURES

LIST OF ABBREVIATIONS

AC	Alternating Current
ANFIS	Adaptive Neuro Fuzzy Inference System
BP	Back Propagation
COG	Center of Gravity
DFIG	Double Fed Induction Generator
DVR	Direct Voltage Regulator
EE	Electrical Energy
FACTS	Flexible AC Transmission System
FIS	Fuzzy Inference System
FLC	Fuzzy Logic Controller
GB	Gear Box
GC	Grid Code
GSC	Grid Side Converter
GVOVC	Grid Voltage Oriented Vector Control
HAWT	Horizontal Axis Wind Turbine
KE	Kinetic Energy
LVRT	Low Voltage Ride Through
LSM	Least Square Method
ME	Mechanical Energy
MF	Membership Function
MPPT	Maximum Power Point Tracking
NN	Neural Network
PEC	Power Electronics Converters

PCC	Point of Common Coupling
PF	Power Factor
PI	Proportional Integral
PID	Proportional Integral Derivative
PMSG	Permanent Magnet Synchronous Generator
PWM	Pulse Width Modulation
RES	Renewable Energy Source
RSC	Rotor Side Converter
SCIG	Squirrel-Cage Induction Generator
SFOVC	Stator Flux Oriented Vector Control
STATCOM	Static Synchronous Compensator
VAWT	Vertical Axis Wind Turbine
VC	Vector Control
WECS	Wind Energy Conversion System
WRIG	Wound Rotor Induction Generator
WT	Wind Turbine
WTG	Wind Turbine Generator

ABSTRACT

Due to the technological advancement of wind turbines (WTs) from fixed to variable speed, wind energy is now becoming one of the most accessible and exploitable types of renewable energy. Large wind power stations frequently use Double Fed Induction Generator (DFIG) based Wind Energy Conversion Systems (WECSs). DFIG has several advantages, including a lower rated power converter, lower costs, lower losses, improved efficiency, variable speed operation, and independent active and reactive power control capabilities. However, connecting this wind farm to the current grid poses significant power system difficulties. This is due to DFIG's vulnerability to grid faults such as voltage dip. This fault causes the flow of excess current across both the stator and the rotor terminals, which may consequently lead to some serious damage of the generator, power converters, and also DC Link capacitor. However, in spite of all of this, the current Grid Code (GC) requires the system to stay connected to the grid during this fault condition and support it in retaining its nominal voltage. This capacity of the system is also known as Low Voltage Ride Through (LVRT) capacity. For the system to archive such capacity, some appropriate protection mechanisms or controlling strategies must be utilized. Therefore, in this thesis, the crowbar protection technique and the Adaptive Neuro Fuzzy Inference System (ANFIS) controller are employed. Furthermore, the performance of the system while employing the PI controller, crowbar protection technique, and ANFIS controller is analyzed and compared under grid fault conditions, i.e., a voltage dip with a magnitude of 0.1pu (worst case) using MATLAB/Simulink 2021a software and based on actual data obtained from Adama II wind farm. The settling time of ANFIS for controlling the rotor currents in d and q axes (idr and iqr) and DC link voltage is 3.6 seconds, 3.57 seconds, and 3.4 seconds, respectively. On the other hand, the settling times of the PI controller for the controlling the rotor currents in d and q axis and the DC link voltage are 4 seconds, 3.91 seconds, and 45.2 seconds, respectively, while the crowbar protection technique's settling times are 4, 6, and 4.9 seconds, respectively. According to these simulation results, the ANFIS controller provided the best performance of the three strategies since it allowed both the rotor currents and the DC link voltage to return to their steady state values faster than the remaining two techniques.

Keywords: Adaptive Neuro Fuzzy Logic Controller, Crowbar, Double Fed Induction Generator, Grid Code, Low Voltage Ride Through, MATLAB/Simulink

CHAPTER ONE

1. INTRODUCTION

1.1. Background

Nowadays, more focus is being placed on renewable energy sources (RES) mainly due to the developing environmental issues associated with the usage of traditional energy sources (*Energy Statistics Course – Paris – 2nd of March 2015*, 2015). RES are nonpolluting energy sources, derived from naturally replenished materials or processes. Fossil fuels' finite nature, the increase in the cost of existing energy sources, and the emission of toxic pollutants after combustion are the motivating factors behind their utilization (Jagadeeshwaran & Kumar, 2017). Among different RES, wind energy is the most rapidly expanding source of electricity. Its production and usage have been aided by factors such as technological developments in the field of engineering and a rising understanding of energy security (Mengistu, 2017) .

The Wind Energy Conversion System (WECS) is a system that generates electricity by extracting the kinetic energy (K.E) in the air and converting it to Electrical Energy (E.E) via an electrical generator (Echiheb & Ghamrasni, 2022). Wind Turbines (WTs) are the basic components of WECS that can be categorized, mainly based on their axes of rotation and rotor speed. Based on the axis of rotation, they can be classified as Horizontal Axis Wind Turbines (HAWTs) and Vertical Axis Wind Turbines (VAWTs). On the other hand, depending on the rotor speed, they can also be classified as variable or fixed speed wind turbines, which are then further classified into Type I, Type II, Type III, and Type IV WTs. A variable-speed wind turbine is more advantageous than a fixed-speed wind turbine for a variety of reasons. The ability to generate a large amount of energy over a wide range of wind speeds, the reduction of acoustic noise and the provision of broad active and reactive power management, power fluctuation reduction, and the ability to control power independently are just a few of them (Haq et al., 2016).

The WT with Double Fed Induction Generator (DFIG) is a widely used WECS for the production of electrical energy (Controllers & Al-zabin, 2019). This is due to its wide-range operation speeds, with converters having lower power ratings. As a result, the converter's overall cost and loss are reduced (Zheng et al., 2013).

Fundamentally, the stator and rotor of DFIG are both connected to the grid. As illustrated in Figure 1.1, its stator is directly tied to the grid. The rotor, on the other hand, is coupled to the grid through back-to-back converters, i.e., the Rotor Side Converter (RSC) and the Grid Side Converter (GSC). Depending on the rotor speed, these converters allow the flow of power from the system to the grid and vice versa. In addition, each converter has its unique advantage in terms of system regulation. The RSC is primarily in charge of regulating the active and reactive power of the system. GSC, on the other hand, is used to keep the DC Link's voltage constant. A DC Link Capacitor is employed between these two converters for energy storing purpose (Falehi & Rafiee, 2017).

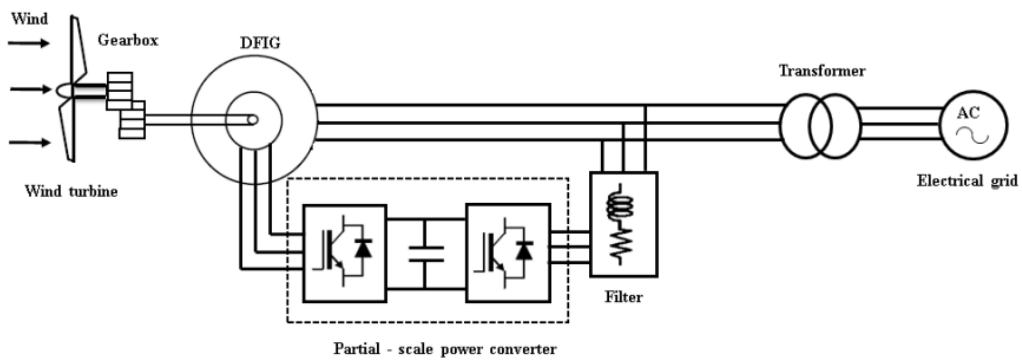

Figure 1.1: DFIG Based WECS (Hamdan & Noureldeen, 2021)

However, in spite of all of its advantages, DFIG-based WECS is extremely sensitive to grid faults, particularly voltage dip. This is mainly due to the direct coupling of the stator of the generator to the grid and also due to the limited capacity of converters. Voltage dips in a weak grid will generate undesirable dynamics in the controller of DFIG-based wind turbines, possibly resulting in signal instability (Rao & Nanajee, 2016). Furthermore, it may also cause rotor overcurrent and DC link fluctuation, which leads to some serious damages on semiconductors in the RSC as well as on the DC link capacitor. However, in spite of all this, the current Grid Code (GC) requires the system to stay coupled to the grid during this fault scenario and offer support to the grid to retain its nominal voltage within a short period of time, which is also known as Low Voltage Ride Through (LVRT) capacity. For the system to archive with such capacity, different protection techniques and control strategies must be employed (Madan & Kumar, 2019).

1.2. Statement of the Problem

DFIG based WECS is extremely susceptible to grid disturbances/faults. One of the most frequent faults likely to occur in the power system is the voltage drop across the grid terminal. When a voltage dip occurs on the grid side, the voltage at the stator terminal also lowers due to the direct connection of the DFIG's stator to the grid. This causes an abrupt change in the DFIG's stator flux, which eventually leads to an overcurrent in the rotor windings due to the magnetic coupling. This overcurrent could damage semiconductors on the rotor-side converter. In addition to this, the occurrence of this fault disables the GSC from supplying power to the grid, which subsequently leads to the concentration of high voltage across the DC Link terminals, causing some serious damage to the DC link's capacitor due to overcharging. The grid, on the other hand, typically requires the wind generator to remain connected to the grid regardless of the fault and supports it to retain its nominal voltage. This can be accomplished by employing either the proper control mechanisms or protection techniques.

Therefore, in this thesis, DFIG-based WECS is modeled using MATLAB-Simulink software, and then its performance is analyzed under grid fault circumstances, i.e., voltage dip. Furthermore, an Adaptive Neuro Fuzzy Inference System (ANFIS) Controller and crowbar are also employed to protect the converters and generator from being damaged by the fault and also to allow the system to enhance its Low Voltage Ride Through (LVRT) capacity as required by the Grid Code (GC).

1.3. Objective

1.3.1. General Objective

The general objective of this thesis is to compare the Low Voltage Ride Through Techniques for DFIG in WECS Under Fault Conditions.

1.3.2. Specific Objectives

- To model WECS, which consists of DFIG, back-to-back converter, filter, and DC Link using MATLAB-Simulink software.
- To evaluate and analyze the performance of the system during the occurrence of a voltage dip on the grid side.
- To improve the LVRT capacity of the system by using a crowbar protection technique, PI controller and an Adaptive Neuro Fuzzy Inference System (ANFIS) controller.

- To compare the performance of the system under voltage dip employing PI, crowbar and ANFIS LVRT enhancement techniques.

1.4. Scope of the Thesis

The scope of this thesis is to study the performance of DFIG in WECS under different dynamic conditions. It mainly involves the collection of different data through reading of different papers; proper modeling of DFIG and back-to-back converter; evaluating and analyzing the system's performance under dynamic conditions by adequately modeling the entire system, which is tied with the grid in MATLAB software and finally developing a system with fault-tolerating capacity by using an appropriate controller and protection techniques.

1.5. Significance of the Thesis

When the voltage on the grid side drops, the current on the rotor terminal increases, causing severe damage to the RSC. In addition to this, the GSC is unable to transfer or supply power to the grid, which leads to the concentration of high voltage at the DC Link terminals causing some serious damage to the DC link's capacitor due to overcharging. The Grid Code, on the other hand, requires that the system remain connected in both normal and fault scenarios. So, to achieve this in this thesis, an Adaptive Neuro Fuzzy Inference System (ANFIS) is used to protect the system from being damaged during the occurrence of the fault. It is also used to keep the RSC connected to the grid during a fault. This enables the system to support the grid during a voltage dip, allowing it to maintain its nominal voltage in a short amount of time without the use of any additional auxiliary devices, which makes it more cost-effective.

1.6. Thesis Outline

In total, this thesis has five chapters. Background information, objectives, and significance of the study, as well as a statement of the problem, are all included in the current chapter. The second chapter discusses the theoretical background of DFIG-based WECS, including several WT types. In addition, a review of the GC requirements, several relevant literatures, and techniques for enhancing LVRT capabilities are also included in this chapter. The third chapter is entirely devoted to the modeling of the system under study. It consists of a mathematical model of DFIG, including all of its operational modes. The design of control strategies for the system under study is also covered in this chapter. On the other hand, the simulation results from DFIG's performance under normal and grid fault scenarios are covered in the fourth chapter. In addition to this, the performance of the DFIG employing the PI controller, crowbar, and also the Adaptive Neuro Fuzzy Inference System (ANFIS) is analyzed and compared under the grid fault condition. Finally, chapter five presents the conclusions drawn from the simulation results, along with some future works.

CHAPTER TWO

2. LITERATURE REVIEW AND RELATED WORKS

2.1. Theoretical Background

Due to their ability to operate at a wide speed range, Double-Fed Induction Generators (DFIGs) are the most widely utilized generators for variable-speed WECS. Power converters are mostly in charge of this. Fundamentally, the stator of DFIG and the grid are directly coupled, while its rotor is tied to the grid through power converters (i.e., RSC and GSC). RSC is employed to regulate the active and reactive power exchange of the DFIG, whereas GSC is employed to maintain the DC link's voltage constant (Falehi & Rafiee, 2017).

Furthermore, using these converters has the advantage of enabling the import and export of power to the grid. This enables the system to support the grid in the event of faults like voltage dips and also enhances the system's stability. In addition, the machine's synchronization with the grid can be maintained by adjusting the rotor voltages and currents even when the wind speed changes. On the other hand, the system provides only 20–30% of the generated power to the grid through the power converter, whereas the remaining is fed directly from the DFIG's stator to the grid. Therefore, the converter's cost, size, and loss are minimum, and the DFIG's efficiency is high (Karad & Thakur, 2021).

When it comes to grid concerns, DFIGs have a significant disadvantage. When grid-side failures like voltage dips occur, the voltage across the generator's stator terminal drops as well, resulting in an overcurrent at the rotor terminal due to magnetic coupling. This overcurrent may cause severe damage to the RSC as well as voltage fluctuations in the DC link [8]. Generators had to be withdrawn from the grid promptly if such problems existed for decades to protect the generator, power converters, and DC-link's capacitor. However, nowadays, numerous power system strategies modify their requirements for wind farms with various models, known as Grid Codes (GC). According to these GCs, Low Voltage Ride-Through (LVRT) is the ability of a Wind Turbine Generator (WTG) to remain connected to a grid in the event of voltage dip and to support it in retaining its nominal voltage within a short period. LVRT is the major challenge to WECS, which is coupled to the grid (Vats et al., 2018).

2.2. Wind Energy Conversion System (WECS)

It is a system that extracts Kinetic Energy (K.E) from the air to drive the rotor of a Wind Turbine (WT), which is subsequently converted to electrical energy by an electrical generator. However, since the M.E. gained by turning the rotor of the WT may not always be sufficient to drive the generator, so, a Gear Box (GB) is employed to increase the rotational speed of the generator. Then the generated power is transported through a transformer, which converts the electricity to the grid (GANTHIA et al., 2021).

The relationship between WT's output power and wind speed is demonstrated by the power curve. Figure 2.1 displays a graph between wind speed and generated power.

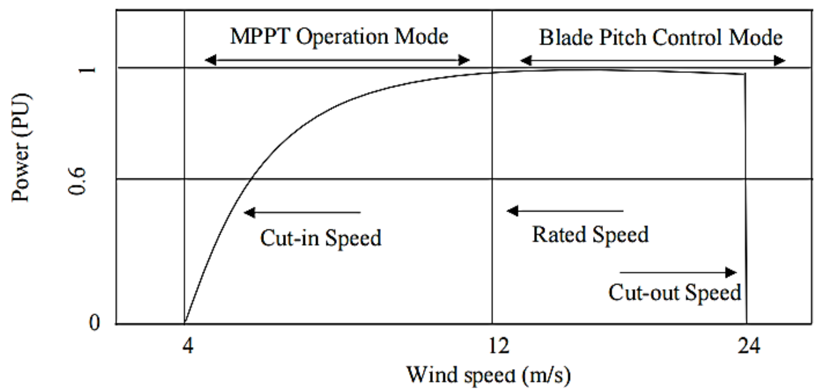

Figure 2.1: Power Curve (Salem Molla, 2021)

Depending on the wind speed, the power curve has three distinct operating regions. The first region is called the Cut in wind speed region, where useful power is generated by the system operating with the lowest wind. The region where rated (maximum) power is generated by the generator is known as the Rated Speed region. The speed of operation in this region is mostly 12 m/s. Finally, there is the Cut-Out region, which is the final region. It operates with a maximum wind speed that a WT can transport useful power or it can operate safely (Janssens et al., 2016).

2.3. Components of Wind Turbines (WT)

Wind turbines contain rotor blades, generators, a nacelle, a tower, a Gear Box (GB), a foundation, and a protection and control system.

The rotor blade is responsible for converting the Kinetic Energy (KE) stored in the wind to Mechanical Energy (ME) using a shaft. This M.E is converted into E.E in the generator. However, when the M.E produced is insufficient for the operation of the generator, it is occasionally essential to use GB. The generator, GB, drive train, and brake assembly is all housed within a nacelle. On the other hand, a tube that is used to connect the rotor of WT to the foundation is called a tower. It is employed to increase blade's height to enhance the volume of air drawn by the WT. The foundation is used to support the entire WT by properly fixing it to the ground. A protection and control system is the final component of WT. This system is utilized to protect the WT from being damaged by prohibiting it from operating in hazardous situations. It has a brake system that sends a signal to stop the rotor from turning during higher wind speeds (Singh, 2015).

2.4. Types of Wind Turbines (WTs)

Wind turbines are classified depending on their axis of rotation and rotor speed.

2.4.1. WT Classification as Per Axis of Rotation

WTs are divided into Horizontal Axis Wind Turbines (HAWT) and Vertical Axis Wind Turbines (VAWT) depending on their axis of rotation.

2.4.1.1. Horizontal Axis Wind Turbine (HAWT)

In this WT, the rotating axis is horizontal to the ground and parallel to the wind stream. When wind hits the blades, they begin to rotate, but at a low rpm due to noise and mechanical strength concerns. As a result, GB is employed to archive fast rotation. The system is protected by a braking system during high-wind conditions. Finally, the generated electricity is delivered through the cables to the base, where the step-up transformer is located and then fed to the grid (Johari et al., 2018).

In the case of HAWT, to produce maximum power the WT should always face the wind's direction which is not possible all the time. As a result, a velocity sensor is mounted on the nacelle's top for measuring the wind's direction and speed (Vivek, 2017). HAWTs are categorized into upwind and downwind WTs based on their rotor's orientation.

i. Upwind Wind Turbines

These are wind turbine where the blades are exposed to the wind first before the nozzle. The main benefit of employing this type of turbine is that it eliminates wind shading behind the tower, and allows the blade to receive the wind without the tower getting in the way. However, they have some drawbacks due to the requirement rigid or inflexible rotor which should be placed at some distance from the tower. Otherwise, if the rotor is flexible, it may be deflected to some extent and may strike the tower, causing severe damages. A yaw mechanism is necessary for aligning the turbine with the wind's direction (Johari et al., 2018).

ii. Downwind Wind Turbines

It's a HAWT with a rotor on the tower's back. A yawing device is not necessary because the nacelle is designed to seek the wind or the nozzle naturally moves in the desired direction. The rotor blades can be flexible because there is no threat from the tower striking in this case. However, tower shading, which produces power variations, is the main drawback of this type of turbine (Johari et al., 2018).

2.4.1.2. Vertical Axis Wind Turbine (VAWT)

In this type of wind turbine, the rotor axis blade rotates perpendicular to the wind's direction. Its operation is similar to that of HAWT, although there are a few differences, as shown in Table 2.1. In high wind operations, they are less efficient than HAWT, but they are more efficient in low-wind activities.

Table 2.1: Comparison Between HAWT and VAWT (Johari et al., 2018)

Horizontal Axis Wind Turbine (HAWT)	Vertical Axis Wind Turbine (VAWT)
✓ Tower requirement	✓ No need for a tower
✓ Have more WT speed	✓ Have lower speed
✓ Have more cost	✓ Less cost
✓ Components are located at the top of the tower	✓ Components are located on the ground
✓ Need more maintenance	✓ Less maintenance requirement
✓ Require yaw control to track wind direction	✓ No need for yaw control
✓ More power generation	✓ Lower power production

VAWTs are further classified into two which are Darrieus VAWTs and Savonius VAWTs.

i. Darrieus VAWTs

They're lift-type WTs that require a little engine to get started. Their direction contributes to the emergence of several drag fighting concerns when returning blades are used (i.e returning side's torque fights the advancing side). As a result, they can only produce around half of Betz's maximal energy (i.e maximum theoretical power) (E.A.D. Kumara K.G.R.M. Jayathilake, 2017).

ii. Savonius VAWTs

Unlike the darrieus type, Savonius VAWTs are drag-based type WTs. It contains two or three scoops that move when dragging force is applied. The primary advantage of utilizing this type of turbine is that it can spin in any direction of the wind. Their configuration enables them to absorb some more energy from the downwind blade in addition to the energy obtained by the upper wind blade. In comparison to the darrieus VAWTs, they are more complicated and efficient. Even though they move slowly, they may generate higher torque (E.A.D. Kumara K.G.R.M. Jayathilake, 2017).

2.4.2. Classification of Wind Turbines based on the Rotor Speed

Wind turbines are categorized as fixed speed or variable speed based on the rotor speed, which is then further divided into four categories. These are:

- Fixed Speed Wind Turbine (Type I)
- Partial (Limited) Speed Wind Turbine (Type II)
- Variable Speed Wind Turbines:
  - ✓ Variable Speed Wind Turbine with a Partial Scale Power Converter (Type III)
  - ✓ Variable Speed Wind Turbine with a Full-Scale Power Converter (Type IV)

2.4.2.1. Fixed Speed Wind Turbines (Type I)

In this type of WT, the generator and grid are directly coupled through a transformer. A soft starter is utilized to minimize the in-rush current during startup (A. Kumar, 2013).

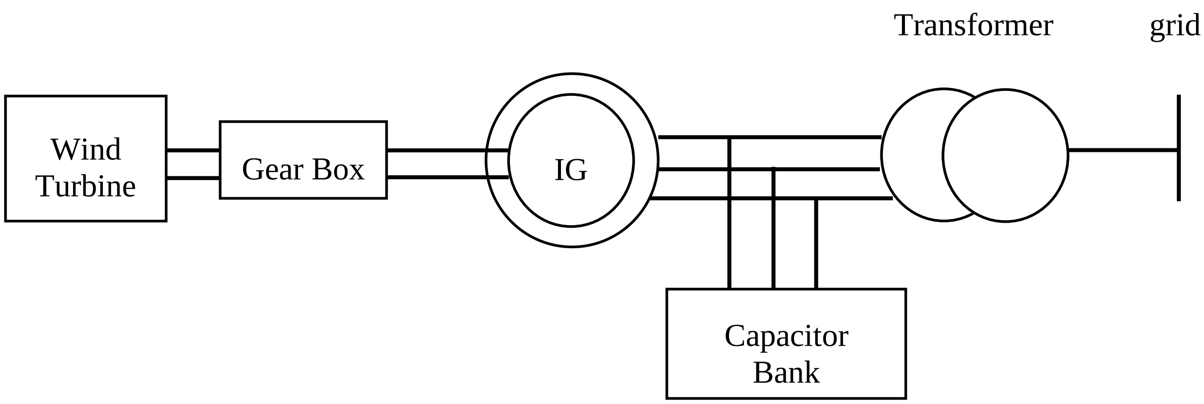

Figure 2.2: Fixed Speed Wind Turbines (Singh, 2015)

A compensator (i.e capacitor bank) is also employed to minimize the reactive power requirement from the wind generator. Since the speed of the wind is almost fixed to the grid frequency, it is impossible to store turbulence as rotational energy. So, to maximize the total system's performance, aerodynamic control of the blades is required. This makes the system to become more sophisticated, and costy. Fixed WT has the advantage of being quite simple, which lowers the investment cost (A. Kumar, 2013).

2.4.2.2. Partial (Limited) Speed Wind Turbine (Type II)

Similar to that of Type I WT, this type of WT employs a generator (i.e., a wound rotor induction generator) which is coupled with the gird through a transformer. The rotor winding of a generator is coupled in series with variable resistance, allowing torque characteristics and operating speed to be modified within a specific range (Salem Molla, 2021).

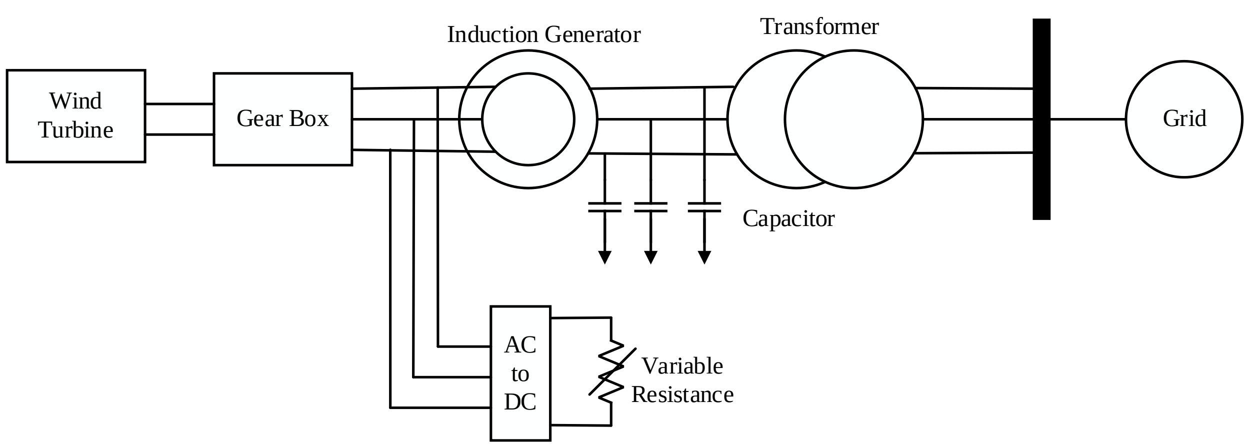

Figure 2.3: Partial Speed Wind Turbines (Salem Molla, 2021)

2.4.2.3. Variable Speed Wind Turbines

Unlike fixed speed WT, variable speed WT operates over a wide range of rotor speed. This enables the system to generate maximum power as wind speed varies. Even though wind variation generates power fluctuation, it can be controlled by adjusting the rotor speed. This approach improves the system's power quality compared to the fixed type. Another advantage of the variable-speed turbine is that it uses power electronic devices to enable bidirectional power flows from the grid to the system and vice versa (Thapa, 2021). Variable speed WT are classified into two. These are:

i. Variable Speed Wind Turbine with Partial-Scale Power Converter

ii. Variable Speed Wind Turbine with Full-Scale Power Converter

i. Variable Speed Wind Turbine with Partial Scale Power Converter (Type III)

A DFIG with a partially rated converter is employed in this type of WT. As illustrated in Figure 2.4, the generator's stator is directly tied to the grid, while its rotor is connected to the grid via a power converter (Singh, 2015).

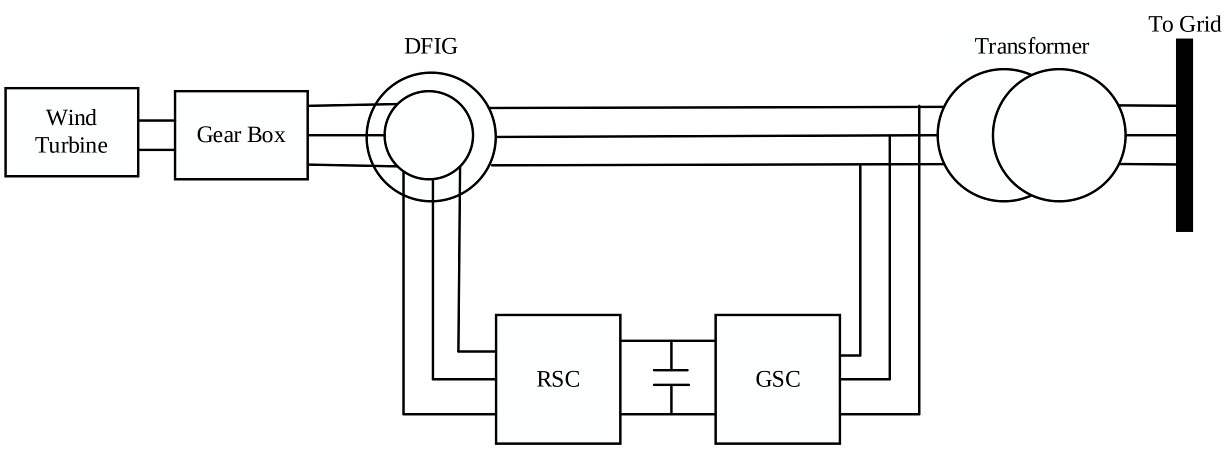

Figure 2.4: Variable Speed WT with Partial Scale Power Converter (Singh, 2015)

ii. Variable Speed Wind Turbine with Full-Scale Power Converter (Type IV)

A Permanent Magnet Synchronized Generator (PMSG) with a full-rated converter is employed in this type of WT. The electrical generator's features and dynamics are effectively separated from the power grid since the static power converter processes all of the power from the turbine [18].

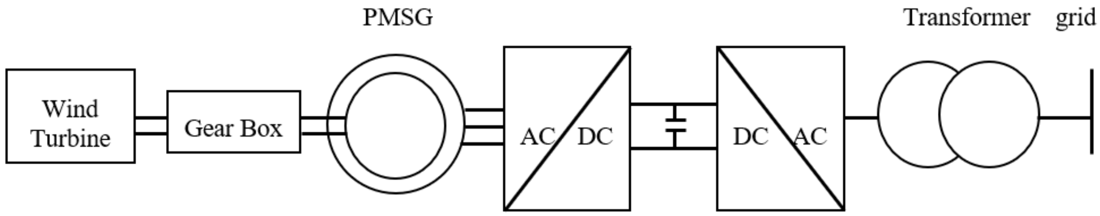

Figure 2.5: Variable Speed WT with Full-Scale Power Converter (Singh, 2015)

2.5. Operation of DFIG under Normal and Fault Condition

2.5.1. DFIG under Normal Operation

As previously stated, the DFIG's stator and grid are directly coupled, whereas its rotor is connected to the grid by back-to-back converters, i.e., RSC and GSC (Madan & Kumar, 2019). The control of both converters in this study is carried out using a vector control strategy. As stated in the preceding section, the primary goal of RSC is decoupled regulation of stator's active and reactive power. This is archived by converting the rotor current (ir) into the d-q components (idr and iqr) in the stator frame of reference. Stator active power is controlled by regulating the rotor current in the quadrature axis (iqr), whereas stator reactive power is controlled by regulating the rotor current in the direct axis (idr). Furthermore, controlling the dq component of these currents can also be used to maintain a steady DC Link voltage (Nafar et al., 2016).

2.5.2. DFIG under Fault Conditions

DFIG is extremely vulnerable to grid faults since its stator is directly connected to the grid. Faults in the grid arise for a variety of reasons, including insulation failure, tree branches falling on power wires, and other natural disturbances (Sitharthan et al., 2018).

Grid faults can be classified as: symmetrical and asymmetrical faults. Symmetrical faults are faults that affect each phase simultaneously. Since each phase carries the same fault current, the system stays balanced. Short circuits (three phases) and three phases to the ground fault (LLLG) are the major types of symmetrical faults. Unsymmetrical faults, on the other hand, harm only one or two phases, causing the system to become unbalanced. The line to ground (LG), double line to ground (LLG), and line to line (LL) are the main categories of these faults (Liu et al., 2020).

A voltage dip is one of the most frequent grid faults. If the drop is the same across all three phases, it's called a balanced or symmetrical fault. Faults caused by inrush currents during the start-up of the motor are examples of this type of fault. On the other hand, an unsymmetrical voltage dip happens when the faults that cause the voltage dip do not evenly influence each phase (Gholizadeh et al., 2018).

When a voltage dip occurs in the stator winding, the stator flux decreases. Furthermore, if this voltage is not restored within a short amount of time, it may result in the flow of a huge amount of current through the rotor winding due to the magnetic coupling between DFIG’s stator and rotor windings. However, the conductors are unable to handle such a large amount of current due to their reduced size. Therefore, this may damage the semiconductors of RSC. In addition to this, it also inhibits the GSC from supplying power, causing the concentration of a high amount of voltage at the DC Link terminal. Therefore, the application of a protection or controlling mechanism is mandatory for the consistent operation of the system (Rashid & Hasan, 2017).

2.6. Grid Code Requirements

Most countries' grid codes attempt to ensure that their consumers have continuous access to power. This necessitates not only the appropriate level of generation to fulfill the load demand but also the capacity of users since both load and generation are responsible for the system's security. For this, the following critical technical criterias, which appear to be common across most countries due to their grid nature, are necessary. These are (Thapa, 2021):

- Frequency and voltage tolerance,
- Reactive power control and voltage support,
- Active power control and
- Fault ride-through capability

2.6.1. Frequency and Voltage Tolerance

Due to its dynamic nature, the network's electrical behavior changes frequently in terms of frequency and voltage. On the other hand, as the power system's frequency determines whether generation and load are balanced or not, users of the transmission system are required to operate within a specific range of frequency and voltage. However, unplanned generation loss and fluctuations may result in under-frequency and over-frequency in the system. This leads to supply instability, electrical equipment overloading, poor power quality, and other issues (Tuka & Leidhold, 2017)(Shukla & Tripathi, 2012).

Therefore, to avoid these problems, a certain wind farm must operate continuously within the limited range of voltage and frequency variations. For a 50 Hz system, this would be in the range of 49 to 51 Hz in terms of frequency and 10% of the nominal value in terms of voltage. However, there are times when this range must be expanded to allow the system to operate in an extreme state for a specified period. In Italy, for example, the wind turbine must operate between 47.5 and 51.5 Hz, while in the UK it must function between 47.5 and 52 Hz, including at least 20 seconds between 47 Hz and 47.5 Hz. Beyond these limits, the user would generally be required to disconnect from the system, as this would endanger the generating plant and result in total power loss (Sourkounis & Tourou, 2013).

2.6.2. Reactive Power Control and Voltage Support

The grid code explains the reactive power control in terms of power factor and voltage support as follows.

2.6.2.1. Power Factor Control

It is highly recommended for networks to operate with voltage and current in phase (i.e power factor = 1) to eliminate losses and maintain high levels of efficiency. However, users of electrical systems utilize inductive loads that cause voltage and current to be out of phase. Since the current precedes the voltage, inductive load's power factor is leading. To put it another way, there is high consumption of reactive power by the user (L. Chen et al., 2020). Therefore, to balance the network's reactive power, the user must have the capacity to adjust their reactive power consumption or production (Shukla & Tripathi, 2012).

2.6.2.2. Voltage Support

The voltage across the local's network is maintained within its defined limits by regulating reactive power output or consumption. Reactive power must be supplied to the network if the network voltage falls below a predetermined range. On the other hand, if the network voltage exceeds a specified limit, reactive power must be consumed to reduce the voltage to allowable limits. In such a way, wind farms can maintain the grid voltage stable during voltage swings (Ismail & Bendary, 2016).

2.6.3. Active Power Control

It is the capacity of WTG to adjust the active power output by system requirements. It is used to provide system stability, prevent transmission line overloading, and avoid high voltage steps and in-rush currents during WT's startup and shutdown. The rate of change of active power can be limited by controlling the pitch angle of the turbine's blade. This is required due to the limited capacity of generators and transmission lines. In Denmark, the rate of active power limit is set at between 10% and 100% of normal power per unit time. The major goal of this restriction is to prevent frequency variations caused by high voltage and current at the start and end of a WECS's operation (Shukla & Tripathi, 2012).

2.6.4. Fault Ride Through (FRT)

As previously stated, the modern GC requires the WTG to stay connected to the grid during various fault scenarios. There are different types of faults that occur across the grid terminal. Some of them are line to ground fault, three phase to ground fault, line to line fault, three phase or short circuit fault, etc. A short circuit fault across the grid's terminal can generate 5-8 times the rated stator current, resulting in a strong inrush rotor current that can cause stress on the mechanical drive and shaft, overcurrent in a RSC, and overvoltage in a DC bus. Therefore, to prevent this harm and enhance the ability to ride faults (FRT capability), various protection and control mechanisms must be implemented (Ismail & Bendary, 2016).

2.6.4.1. Low Voltage Ride Through (LVRT)

Despite its numerous advantages, DFIG is highly vulnerable to faults at the grid terminal. This is owing to the stator's direct connection to the grid. The most common fault in the power system is a voltage dip at the grid terminal. During this fault, the WTGs are required to remain connected to the grid and support it in maintaining its nominal value within a short period, which can be termed as Low Voltage Ride Through Capability (LVRT) (Benali et al., 2018).

The GC requirements for voltage dips across the grid terminals vary among countries. According to Spain GC, the system must be able to handle a voltage loss of up to 0.2pu caused by three-phase and single-phase voltage faults for 0.5 seconds and retain its nominal voltage to 0.8pu for the following 0.5 seconds. While in the case of a two-phase fault, the system must continue its operation despite the voltage dip and maintain 0.6pu of its nominal voltage within 0.8s (Tohidi & Behnam, 2016).

According to Denmark's grid code, below a 20% voltage drop, the generator must be detached from the grid within 100 milliseconds, and the system must restore 75% of its voltage within 750 milliseconds. The grid code in Ireland enables the system to run continuously with voltage sags of 0.15pu at 0.625 seconds caused by symmetrical and unsymmetrical faults, but it must regain 0.9pu of its nominal voltage within 3 seconds. When the voltage drops to zero due to symmetrical and asymmetrical faults, the system should remain linked to the grid for 140 milliseconds and 400 milliseconds, respectively, according to Australian GC requirements. However, it must retain 0.7pu of its nominal voltage in 2s and 0.8pu in 10s. Of all the GCs, the German GC is the most suitable one for practical applications. It requires the wind turbine to stay connected to the grid for at least 150 milliseconds for a voltage sag of 0.1pu and to maintain 90 percent of its nominal voltage within 1500 milliseconds after the fault has been cleared (Benali et al., 2018).

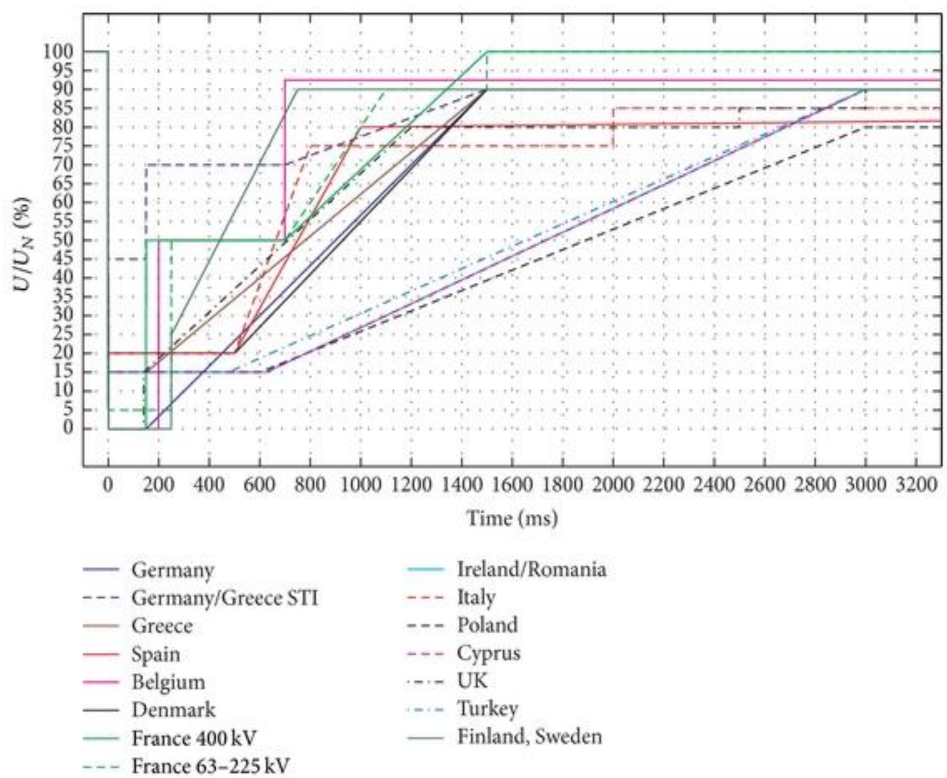

Figure 2.6: National Grid Low Voltage Requirement for Different Countries (Sourkounis & Tourou, 2013)

To improve the LVRT of a WECS, hardware (protection) devices or software (control) based techniques are used. Hardware (protection) devices include a crowbar, DC chopper, energy storage battery system, FACT devices, etc. On the other hand**,** Controller-based methods include conventional controllers, fuzzy controllers, ANFIS controllers etc. In this thesis, a crowbar and Adaptive Neuro Fuzzy Inference System (ANFIS) controller are employed to provide this capability to the system.

i. Crowbar

A crowbar is a bank of resistors that are connected between the DFIG's rotor and the RSC. During steady state operation, the rotor current passes through the RSC. However, when the voltage dips occur in the system, the crowbar isolates the RSC, creating a low-resistance path for the high amount of rotor current that appears due to the fault. The RSC will be connected back to the system when the rotor over-current decays. And since the RSC is withdrawn from the system during the crowbar operation, the machine is adequately safe (Madan & Kumar, 2019)**.**

Nevertheless, blocking RSC has its drawbacks, such as a loss of power control that leads to a significant transient occurring after the fault and ultimately causes the system to be unplugged from the grid. Moreover, during the crowbar action, the generator is converted to a squirrel-cage induction generator, absorbing a significant amount of reactive power from the grid and extending the recovery time. It's also difficult to determine the exact timing and value of crowbar's resistance. If the crowbar action takes a longer time, more reactive power is absorbed, which results in a lengthening of the recovery time. However, a short period may not be enough to protect the system from being damaged by the over-current. On the other hand, a high crowbar resistance causes a high torque value, whereas a low crowbar resistance causes a higher current during the fault (Jayanthi & Devaraj, 2019a).

ii. Fuzzy Logic Controller (FLC)

A Fuzzy logic controller (FLC) is a controller that uses a systematic method to control a non-linear system based on the implementation of human knowledge. Using FLC is more advantageous than using conventional controllers such as PI controllers. The main advantage of FLC is that exact mathematical modeling of the plant is not necessary. It also has the capability to control nonlinear and uncertain systems with limited information input. In addition, it is robust, more efficient, reliable, and simple to design. However, the main drawback of FLC is the requirement of expert knowledge to determine the range of inputs and outputs as well as the rules (Rached et al., 2019).

iii. Adaptive Neuro Fuzzy Inference System (ANFIS) Controller

An ANFIS controller is a Sugeno fuzzy inferenced neural network that integrates the reasoning ability of FLC and the learning capability of a Neural Network (NN) into a single frame of work. Using ANFIS is more advantageous over the FLC since it determines the ranges of inputs and outputs, including the rules, without the requirement of expert's knowledge. In such a way, it reduces the time it takes to determine these ranges and rules and also provides optimized results (V. Kumar et al., 2020).

Rotor overcurrent and DC link overvoltage are the major challenges to address while controlling DFIG during a fault scenario since they should not exceed their limits during the restoring time. Therefore, in this thesis, ANFIS controller is employed to enhance the LVRT capacity of the system by regulating the rotor current and DC link voltage within their limits both during and after fault with the elimination of external devices like the crowbar and without disconnecting the RSC from the system. This will minimize the amount of reactive power absorbed during the fault period and also allow the system to recover within a short period (Kuzhali et al., 2019).

2.7. Related Works

Several studies have been conducted over the past few years to improve the LVRT capability of the DFIG wind turbine by utilizing various methods. For instance, in (Jayanthi & Devaraj, 2019b), Crowbar is utilized to improve the system's LVRT capability. In this paper, asymmetrical faults such as LG and LLG faults are taken into consideration. The results show both the rotor current and DC Link voltage are effectively suppressed. However, since the RSC is blocked during the crowbar operation, power loss occurs. The fault also generates large transients, which cause the isolation of the system from the grid. In addition to this, when the crowbar comes into operation, the DFIG is transformed into a conventional squirrel-cage induction generator (SCIG), absorbing a considerable amount of reactive power from the grid and delaying the grid voltage recovery process. Another drawback of utilizing a crowbar is that the value of its resistance should be sufficiently high to limit the rotor current effectively, but the high value of this resistance produces a high voltage drop in the rotor circuit.

In (Naderi et al., 2019), The performance of the proposed technique during symmetrical and asymmetrical faults is evaluated by using PSCAD/EMTDC software. The results demonstrate that by employing a modified DC chopper with sufficient resistance, both the stator and rotor currents are maintained within their limits without the need for any extra voltage sag compensation techniques or fault current limiting techniques. In comparison to a crowbar, this approach is better since it enables the system to function in both fault current limiting and DC link voltage controlling modes. It also allows the grid to recover its nominal voltage within a short period since the RSC is not blocked during its action. However, the usage of additional switches for current limiting purposes creates harmonics in the system, resulting in some power quality issues. As a result, extra solutions are necessary to resolve this problem, increasing the system's cost. In addition to this, it also requires a properly designed chopper circuit; otherwise, it may cause some serious damage to the DC link capacitor.

In (Ganthia, 2020), the activity of shunt FACTS devices in the improvement of the LVRT ability of DFIG-based WTs is examined. These devices were compared based on their performance, the time taken for controller action, their cost, and augmented application reliability. And based on the results obtained, it is concluded that because of its better voltage compensation and faster settling time than other shunt devices, STATCOM is the most effective and reliable in terms of LVRT capability enhancement.

In (GANTHIA et al., 2021), the activity of a series FACTS devices for LVRT ability improvement of WTs is presented in this study. These devices were compared based on their performance, complexity, cost, and augmented application reliability. And from the results obtained, it is concluded that the DVR improves the system's LVRT capability better than the other series devices.

Although these final two arrangements are feasible in some instances, their applicability is limited due to the utilization of an auxiliary device, which makes the system more complex and more expensive.

2.8. Summary of Related Works

Table 2.2: Summary of Related Works

Authors	LVRT Techniques	Findings	Gaps
(Jayanthi & Devaraj, 2019b)	Crowbar	The DC link voltage is effectively suppressed. The nominal value of the rotor current is retained.	Power loss and transient generation. Delays recovery process of the grid voltage.
(Naderi et al., 2019)	Modified DC Chopper with Sufficient Resistance	Keeps both stator and rotor current within their limit.	Rise of power quality issues.
(Ganthia, 2020)	Shunt FACT devices	Better LVRT enhancement by STATCOM	Complexity and additional cost (due to the use of an auxiliary device)
(GANTHIA et al., 2021)	Series FACT devices	Better LVRT enhancement by DVR	

In earlier work, researchers use crowbar protection technique to improve the LVRT capacity of the system. However, blockage of the RSC results in the loss of power control which consequently leads to the unplugging of the system from the grid. In addition to this, during the crowbar operation the machine is converted into Squirrel cage induction generator which results the consumption of more reactive power from the grid delaying the recovery process. In order to solve such issue some researcher uses modified DC chopper with suitable resistance. By employing such approach, it is possible to damp both the rotor overcurrent and DC link overvoltage that appears during the fault period without the additional compensation devices and also without disconnecting the RSC. However, the usage of additional switches for current limiting purposes creates harmonics in the system, resulting in some power quality issues. As a result, extra solutions are necessary to resolve this problem, increasing the system's cost. On the other hand, some researchers employ shunt and series FACT device to improve the LVRT capacity of the system. Although these final two arrangements are feasible in some instances, their applicability is limited due to the utilization of additional auxiliary device, which makes the system more complex and more expensive. Therefore, the thesis ANFIS controller is employed overcome most of the problem mentioned in the above section since it improves the LVRT capacity of system without disconnecting the RSC and also without employing any additional auxiliary devices. Table 2.2 illustrates the summary of related works.

CHAPTER THREE

3. METHODOLOGY AND SYSTEM DESCRIPTION

3.1. Introduction

In this chapter, methodologies to achieve the general and specific objectives of the study are discussed. In addition, the modeling of the DFIG and the power converter are also covered in detail.

3.2 Materials

Materials such as Microsoft Office 2019, Microsoft Visio, MathType6.0, MATLAB/2021a, and Mendeley reference manager are employed to write and edit the thesis document, draw various figures, write different mathematical equations, simulate the system, and cite the references used in this thesis, respectively.

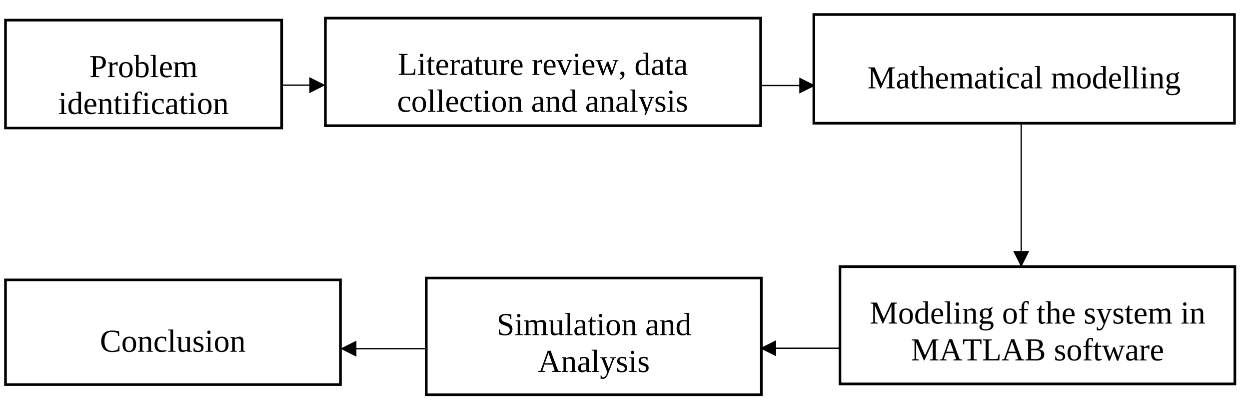

Figure 3.1: System Methodology Flow Diagram

Firstly, many papers that are related to DFIG-based WECS are reviewed. In addition to this, several methods that are employed to improve the system's LVRT capacity are also examined. Secondly, various data that are necessary for modeling the system are gathered and examined using the appropriate methods. These data consist of WT specifications, converter specifications, generator’s parameters, and more. Thirdly, the mathematical models of the DFIG, converters and DC Link are archived. The complete system that is interconnected with the grid is then modeled in the MATLAB-Simulink 2021a software to assess the performance of the system under both normal and fault scenarios. Furthermore, protection and control techniques (i.e., crowbar and ANFIS, respectively) are also employed to enhance the LVRT performance of the system under fault conditions, i.e voltage dip. Finally, a conclusion is drawn based on the results obtained.

3.3 System Block Diagram

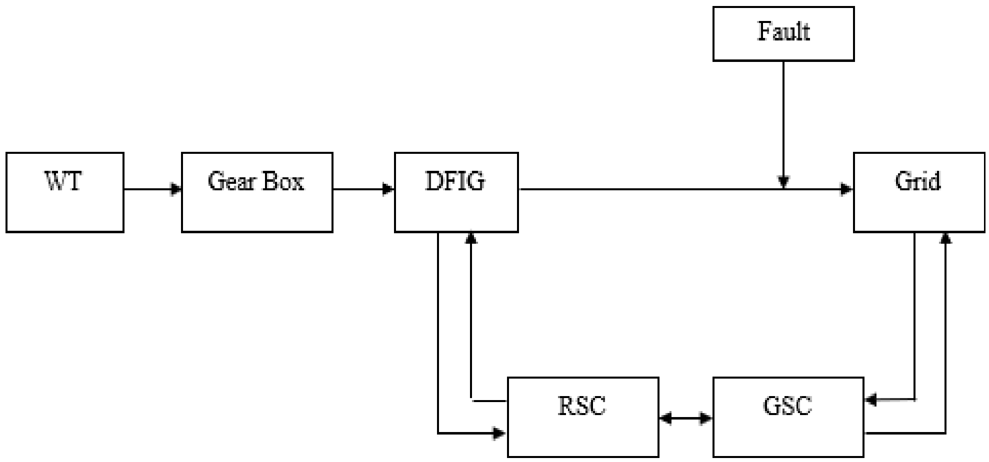

Figure 3.2: System Block Diagram

Description of the block diagram

The mechanical energy of the air is extracted to drive the rotor of the wind turbine, and this energy is converted to electrical energy by an electrical generator. The WT's rotor spins a shaft coupled to a gearbox. The gearbox is utilized to increase the generator's rotational speed, and electricity is generated by converting rotational energy to electrical energy via a magnetic field. As the shown in the figure 3.2 the stator of DFIG is directly coupled to the grid whereas the rotor, is connected to the grid via two electronic power converters (i.e., RSC and GSC). Rotor Side Converter (RSC) is responsible for controlling active and reactive power from DFIG to the grid by adjusting the rotor current, whereas the Grid Side Converter (GSC) is utilized to maintain the DC link voltage constant regardless of power direction. However, a DFIG based WECS are extremely vulnerable to grid disturbances/faults, particularly voltage dips. During grid voltage dips or sag and short circuit on grid side consequently rotor current rises. This leads to damage to DFIG, converter switches, DC-link capacitors and electromagnetic torque fluctuations which cause mechanical stress on the drive-train system of wind turbine. Therefore, in order to archive the LVRT capacity for the system and also to protect the system from damage the crowbar protection technique and also ANFIS controlling strategy are utilized across the RSC and GSC to damp the rotor overcurrent and DC link overvoltage during the fault period in such a way the system stays connected to the grid almost all the time (GANTHIA et al., 2021).

3.4. Wind Speed Model

Wind speed is the fundamental input of a WECS. It varies from time to time and also from place to place in a stochastic way which determines the amount of power drawn by the turbine (Rekioua, 2014). This highly affects both the angular speed and torque of the wind turbine (Tripathi et al., 2019).

A wind speed model consists of four components, such as average, gust, ramp, and turbulence. It can be obtained as follows (Ibrahim & Watson, 2015).

$$V_w(t) = V_{wa}(t) + V_{wg}(t) + V_{wr}(t) + V_{wt}(t) \tag{3.1}$$

where $V_w(t)$ represents wind speed, $V_{wa}(t)$ represents average wind speed, $V_{wg}(t)$ represents the gust wind component, $V_{wt}(t)$ represents turbulence component and $V_{wr}(t)$ represents ramp wind component, all in m/s.

3.5. Wind Turbine Aerodynamic Model

A wind turbine's rotor is a complex aerodynamic device that captures wind energy and converts it to ME. Bernoulli's principle is utilized to comprehend the process simply, as shown in Figure 3.3. Aerodynamic power and torque are two characteristics of a WT (Berhanu et al., 2018a).

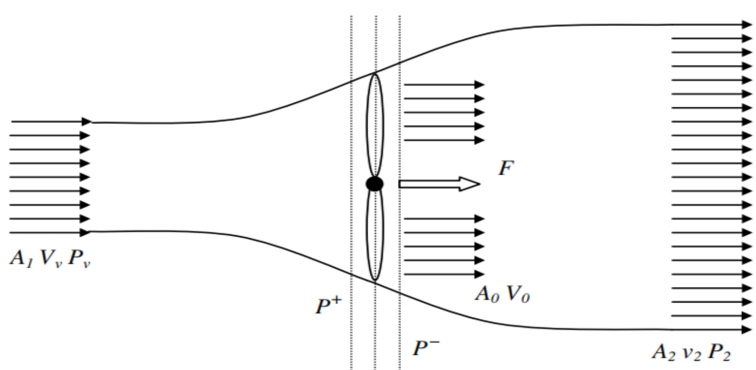

Figure 3.3: Schematic Diagram of Fluid Flow through a Disk-Shaped Actuator (Rekioua, 2014)

With a wind speed V_v, a wind disk radius of R, and a surface A1, the aerodynamic power of the wind, P_w is given by:

$$P_w = \frac{1}{2}\rho\pi R^2 V_v^3 \tag{3.2}$$

Where ρ is the air density [kg/m3], R is the blade radius [m] and Vv is the wind speed [m/s]

The wind turbine's mechanical power, Pm, is calculated using the power coefficient Cp as follows:

$$P_m = Cp * P_w = \frac{1}{2}\rho\pi R^2 V_v^3 Cp(\lambda, \beta) \tag{3.3}$$

where Cp denotes the power coefficient, which indicates how well the WT captures wind energy and converts it to ME. It can be expressed mathematically as follows:

$$Cp(\lambda, \beta) = C_1 * (\frac{C_2}{\lambda i} - C_3\beta - C_4\beta^{C_5} - C6) * \varepsilon^{-C_7/\lambda i} \tag{3.4}$$

and λi is given by:

$$\lambda i = [\frac{1}{\lambda + C8\beta} - \frac{C9}{\beta^3 + 1}]^{-1} \tag{3.5}$$

where λ is the tip speed ratio, β represents pitch angle, and C_1 to C_9 are the wind turbine's characteristic constants.

The ratio of blade tip speed to the incoming speed is known as the tip speed ratio (TSR). It can be expressed mathematically as follow:

$$\lambda = \frac{\Omega * R}{Vv} \tag{3.6}$$

Where the blade tip speed is a product of the rotor's rotating angular speed (Ω) and the blade radius (R).

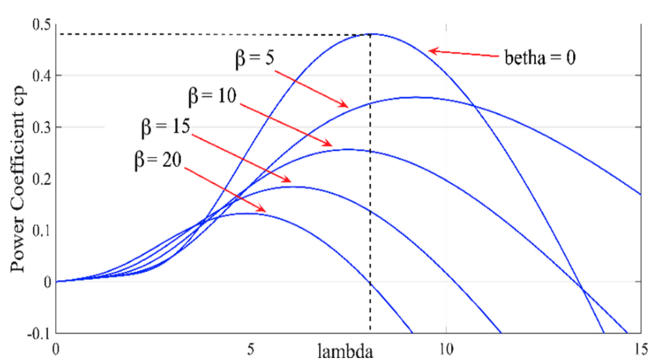

Figure 3.4: Power Coefficient vs Lambda (Rekioua, 2014)

The maximum power drawn by the rotor of WT is only 59.3% of the total available power from the wind at the location of the rotor. This is called Betz’s limit. However, this value is theoretical since it is impossible to obtain this amount of power using real turbines (Adouni et al., 2016).

The theoretical maximum power is given by:

$$P_{\max} = \frac{1}{2}\rho\pi R^2 Vv^3 Cp_{\max}(\lambda,\beta) = 0.3644\pi R^2 Vv^3 \quad (3.7)$$

where $Cp_{max} = 0.593$, $\rho = 1.224 Kg/m^3$

The aerodynamic torque is a ratio of mechanical power to the angular speed of the rotor. It can be obtained by:

$$T_m = \frac{P_m}{\Omega} \quad (3.8)$$

Substitute equations (3.3) and (3.6) for equation (3.8). It results:

$$T_m = \frac{1}{2}\rho\pi R^3 V_v^{\,2} \frac{Cp(\lambda,\beta)}{\lambda} \quad (3.9)$$

The following equation shows the relationship between the power coefficient (Cp) and torque coefficient (Ct).

$$Cp = \lambda Ct \quad (3.10)$$

When equation (3.10) is substituted for equation (3.9), the result is given as follows:

$$T_m = \frac{1}{2}\rho\pi R^3 V_v^{\,2} C_t \quad (3.11)$$

3.6. Gearbox (GB) Model

The turbine and the DFIG are connected via the Gearbox. It multiplies the turbine shaft’s low speed to make it sufficient for the generator. The gearbox is characterized by a ratio G (Jimenez Garibay et al., 2018):

$$\omega_t = \frac{\omega_m}{G} \quad (3.12)$$

where ω_t represents WT's rotating speed and ω_m represents the generator's rotational speed.

The aerodynamic torque, T_{aer} is calculated as follows:

$$T_{aer} = GT_m \tag{3.13}$$

where Tm is the generator's torque.

The shaft connects the gearbox to both the turbine and the generator. The low-speed shaft connects the gearbox to the turbine, while the high-speed shaft connects the gearbox to the generator.

The dynamic equation used for modeling the shaft is characterized by the first order differential equation given by (GANTHIA et al., 2021):

$$J \frac{d\omega_m}{dt} = T_m - T_{em} \tag{3.14}$$

Where J represents inertia.

3.7. Modeling of Double Fed Induction Generator

Double Fed Induction Generator (DFIG) is a variable-speed wind generator with rotor and stator windings. The stator is coupled to the grid directly, while the rotor is connected via two back-to-back converters, the Rotor Side Converter (RSC) and the Grid Side Converter (GSC) (Kuzhali et al., 2019). RSC is used to regulate the amount of active power and reactive power independently so that the DFIG can provide better system stability during fault conditions. GSC, on the other hand, is used to keep the DC link voltage constant independent of the power flow direction (Mohammadi et al., 2017). Furthermore, the utilization of these back-to-back converters enables the movement of power both from the grid to the system and vice versa. This allows the system to support the grid during fault conditions, especially voltage dips so that the grid will retain its nominal voltage within a short period (Akanto & Hazari, 2021).

Since DFIG is the primary component in WECS that generates electricity, proper modeling of it is necessary. This model comprises both steady-state and dynamic modeling, which will be discussed separately in the sections below. However, more emphasis is given to dynamic modeling.

3.7.1. Steady-State Modeling of Double Fed Induction Generator

The steady-state performance of induction generators is investigated using the steady-state model. The following assumptions were used to develop DFIG's steady-state equivalent electrical circuit (Salem Molla, 2021):

- DFIG's stator and rotor windings are linked in a star configuration.
- The grid provides a constant and balanced three-phase voltage amplitude and frequency to the stator.
- Regardless of the stator, the rotor is frequently supplied with a constant and balanced AC voltage amplitude and frequency using a back-to-back voltage source converter.

The relationships between different frequencies of the machine must be defined during steady-state modeling of DFIM (Abu-Rub et al., 2014). This is shown by the following equation.

$$\omega_r = \omega_s - \omega_m \tag{3.15}$$

where ω_s is synchronous frequency, ω_r is rotor frequency and ω_m is rotor electrical speed.

The electrical and the mechanical speed of the shaft Ω_m are related using the following equation (Abu-Rub et al., 2014).

$$\omega_m = p\Omega_m \tag{3.16}$$

Slip (s) shows the relationship between stator and rotor angular frequency.

$$s = \frac{\omega_s - \omega_m}{\omega_s} \tag{3.17}$$

where, ω_s is the synchronous frequency, which has a constant value due to the direct connection of the stator to the grid. On the other hand, ω_r is determined by the shaft's electrical speed ω_m resulting in three different operating modes of the machine.

- $\omega_m < \omega_s \Rightarrow s > 0 \Rightarrow$ Sub- synchronous operation
- $\omega_m > \omega_s \Rightarrow s < 0 \Rightarrow$ Super- synchronous operation
- $\omega_m = \omega_s \Rightarrow s = 0 \Rightarrow$ Synchronous operation

The relationship between the stator and rotor in terms of the number of turns per phase is determined by the "u" coefficient, which is given as:

$$u = \frac{N_s}{N_r} \tag{3.18}$$

where Ns and Nr are the number of turns in the stator and rotor of DFIM, respectively.

The relationship between the induced electromagnetic field in the stator and rotor of DFIM is given by the following equation.

$$E_{rs}' = \frac{E_s}{u} s \tag{3.19}$$

where E_s and E_{rs}' are induced emf in stator and rotor (V).

For practical analysis, the stator and rotor should operate at the same frequency. As a result, the rotor circuit is simply converted to the stator frequency, ω_s using the following formula:

$$V_r - sE_s = (R_r + js\omega_s L_{\sigma r})I_r \quad \Rightarrow \quad \frac{V_r}{s} - E_s = (\frac{R_r}{s} + j\omega_s L_{\sigma r})I_r \tag{3.20}$$

Figure 3.5 illustrates the equivalent circuit which is developed by referring the rotor to the stator with the same frequency for all magnitudes. The equations for this circuit are:

Voltage:

$$\begin{aligned} V_s &= R_s I_s + j\omega_s L_{\sigma s} I_s + j\omega_s L_m (I_s + I_r) \\ \frac{V_r}{s} &= \frac{R_r}{s} I_r + j\omega_s L_{\sigma r} I_r + j\omega_s L_m (I_s + I_r) \end{aligned} \tag{3.21}$$

The stator and rotor fluxes:

$$\begin{aligned} \psi_s &= L_m (I_s + I_r) + L_{\sigma s} I_s \\ \psi_r &= L_m (I_s + I_r) + L_{\sigma r} I_r \end{aligned} \tag{3.22}$$

where, $$\begin{aligned} L_s &= L_m + L_{\sigma s} \\ L_r &= L_m + L_{\sigma r} \end{aligned} \tag{3.23}$$

Substitute equation (3.23) into equation (3.22).

$$\begin{aligned} \psi_s &= L_s I_s + L_m I_r \\ \psi_r &= L_r I_r + L_m I_s \end{aligned} \tag{3.24}$$

Substitute equation (3.23) into equation (3.21)

$$\begin{aligned} V_s &= R_s I_s + j\omega_s L_s I_s + j\omega_s L_m I_r \\ \frac{V_r}{s} &= \frac{R_r}{s} I_r + j\omega_s L_r I_r + j\omega_s L_m I_s \end{aligned} \tag{3.25}$$

where, ψ_s and ψ_r represents stator and rotor flux respectively, on the other hand, Ls, Lr, and Lm are stator, rotor, and mutual inductances, respectively.

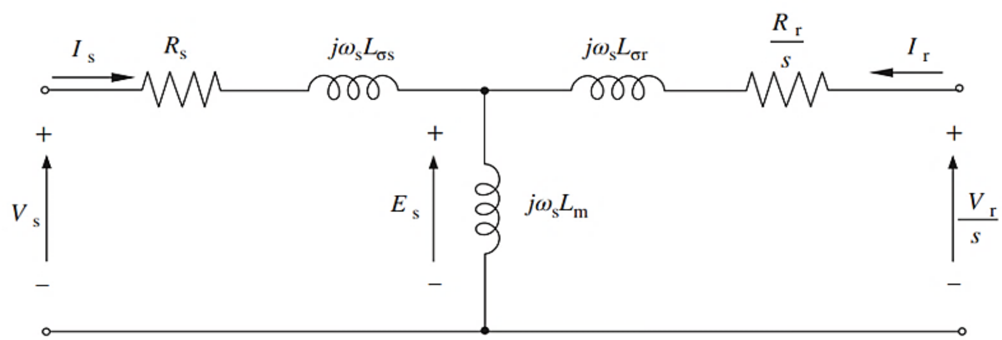

Figure 3.5: Stator Referred One-Phase Steady-State Equivalent Circuit of the DFIG (Abu-Rub et al., 2014)

3.7.1.1. Mode of Operation of Double Fed Induction Generator

The main advantage of using DFIG in WECS is that it permits bidirectional power flows between the grid and the system depending on rotor speed. This enhances system stability by supporting the grid during voltage fluctuations (Xiao et al., 2015).

The DFIG-based WECS has three modes of operation depending on the rotor speed.

- Super- synchronous
- Sub-synchronous and
- Synchronous

i) Super-Synchronous Mode

In this mode of operation, the generator operates above the synchronous speed with negative slip. The mechanical power (Pm) can be delivered to the grid through both the stator and the rotor, as shown in Figure 3.6(a). This power is equivalent to the power delivered to the grid (Pg) when losses in the generator and converters are neglected (Naderi et al., 2019).

ii) Sub-Synchronous Mode

The generator operates at a lower speed than synchronous speed in this mode of operation. Power is supplied to the rotor via the grid. The stator, on the other hand, provides both mechanical (Pm) and rotor (Pr) power to the grid, as shown in Figure 3.6(b). Even though the stator power (Ps) is the sum of Pm and Pr, it will not exceed its rated power since the mechanical power (Pm) from the generator shaft is less in sub-synchronous mode than in super-synchronous mode. The total power supplied to the grid (Pg) equals the difference between the input mechanical power (Pm) and losses (Naderi et al., 2019).

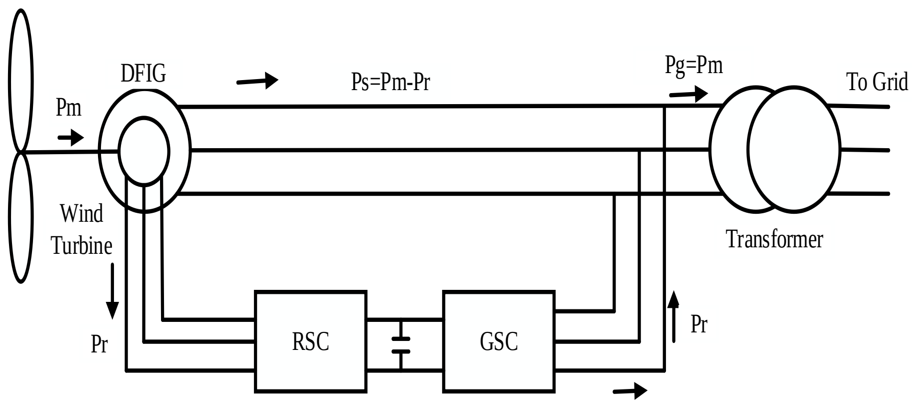

(a) Super-Synchronous Mode

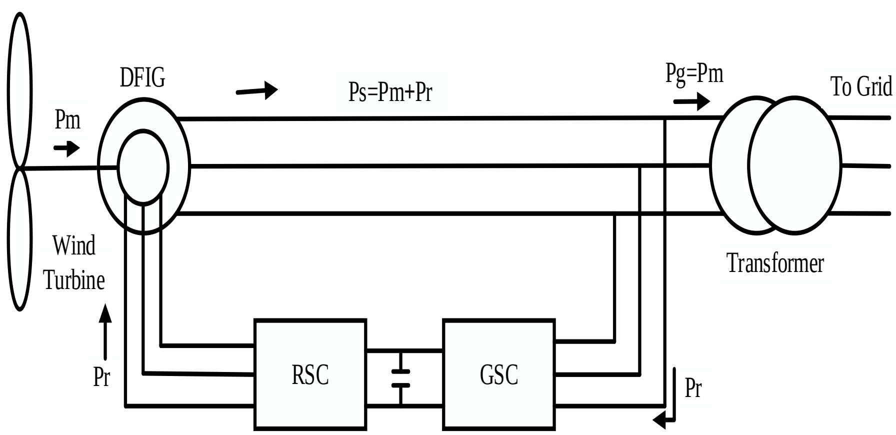

(b) Sub-Synchronous Mode

Figure 3.6: Power Flow in DFIG based WECS (A. Kumar, 2013)

In this thesis, the super synchronous mode of operation is selected. This is due to the fact that the DFIG produces less power in the sub-synchronous mode and the power rating of the converter is determined by the rated or maximum slip in the super-synchronous mode, ensuring that the converters can handle the highest rotor power. In addition to this, during the sub synchronous mode of operation the grid is supplying the power to the grid. To put it in other words the system is consuming reactive power from the grid which delay of the recovery process during the occurrence of voltage dip across the grid terminal (Naderi et al., 2019).

iii) Synchronous Mode

In this mode of operation, the rotor phase sequence is identical to the stator, but no rotor magnetomotive force is generated ($\omega_r = 0$, $\omega_m = \omega_s$). For the generator to function as a synchronous machine and extract energy from a wind turbine, the RSC must supply DC excitation for the rotor. In addition to this, since there is no current or power provided by the rotor winding, the rotor power is zero. The stator winding, on the other hand, feeds the network with a significant quantity of reactive power. Furthermore, since the generated nominal speed is the same as the generator's operational speed, the slip is zero (GANTHIA et al., 2021).

3.7.2. Dynamic Modeling of Double Fed Induction Generator

Dynamic modeling of DFIG is used to evaluate the system's performance under transitory conditions and it is also used to understand machine variables (i.e., torque, flux, current). Due to the complexity of three-phase modeling, converting it to two-phase stationery, rotor, or synchronous frame of reference is desirable (Janssens et al., 2016).

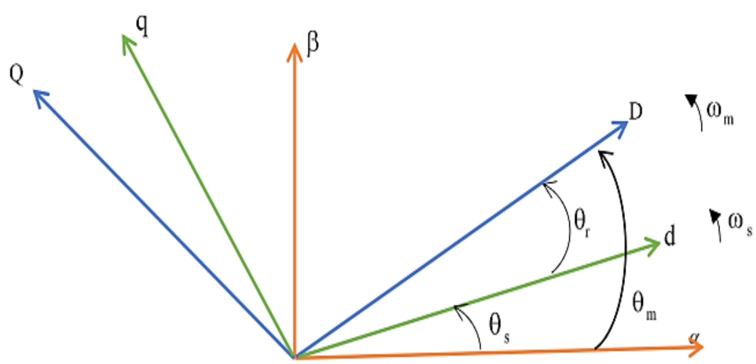

Figure 3.7: Different Reference Frames (Dehong Xu, F. Blaabjerg, 2018)

i) αβ frame of reference

To make the controlling operation easier, three-phase quantities (abc) are transformed into a two-phase stationary frame of reference (αβ) using Clark's transformation. In the matrix, it's written as follows (A. Kumar, 2013):

$$\begin{bmatrix} i_\alpha \\ i_\beta \\ i_0 \end{bmatrix} = Tc \begin{bmatrix} i_a \\ i_b \\ i_c \end{bmatrix} \text{ and } \begin{bmatrix} V_\alpha \\ V_\beta \\ V_0 \end{bmatrix} = Tc \begin{bmatrix} V_a \\ V_b \\ V_c \end{bmatrix} \tag{3.26}$$

where transformation matrix, $Tc = \frac{2}{3}\begin{bmatrix} 1 & \frac{-1}{2} & \frac{-1}{2} \\ 0 & \frac{\sqrt{3}}{2} & \frac{-\sqrt{3}}{2} \\ \frac{1}{2} & \frac{1}{2} & \frac{1}{2} \end{bmatrix}$

Equation (3.26) rewritten as:

$$\begin{bmatrix} i_\alpha \\ i_\beta \\ i_0 \end{bmatrix} = \frac{2}{3}\begin{bmatrix} 1 & \frac{-1}{2} & \frac{-1}{2} \\ 0 & \frac{\sqrt{3}}{2} & \frac{-\sqrt{3}}{2} \\ \frac{1}{2} & \frac{1}{2} & \frac{1}{2} \end{bmatrix} \begin{bmatrix} i_a \\ i_b \\ i_c \end{bmatrix} \text{ and } \begin{bmatrix} V_\alpha \\ V_\beta \\ V_0 \end{bmatrix} = \frac{2}{3}\begin{bmatrix} 1 & \frac{-1}{2} & \frac{-1}{2} \\ 0 & \frac{\sqrt{3}}{2} & \frac{-\sqrt{3}}{2} \\ \frac{1}{2} & \frac{1}{2} & \frac{1}{2} \end{bmatrix} \begin{bmatrix} V_a \\ V_b \\ V_c \end{bmatrix} \tag{3.27}$$

Figure 3.8 shows the dynamic equivalent circuit of DFIG in the αβ frame of reference.

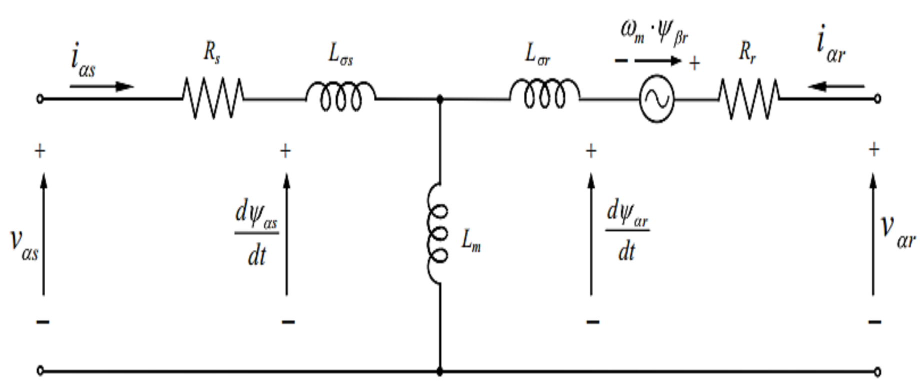

(a) Equivalent Circuit of DFIG in α - axis

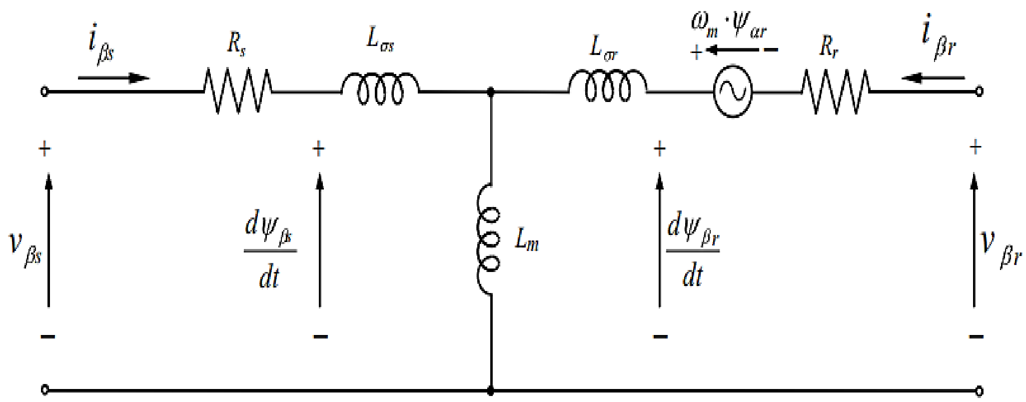

(b) Equivalent Circuit of DFIG in β -axis

Figure 3.8: Equivalent Circuit of DFIG in the αβ Reference Frame (A. Kumar, 2013)

Based on Figure 3.8, the voltage equations for the stator and rotor are given as follows:

$$V_{\alpha s} = R_s i_{\alpha s} + \frac{d\psi_{\alpha s}}{dt}$$
$$V_{\beta s} = R_s i_{\beta s} + \frac{d\psi_{\beta s}}{dt} \qquad (3.28)$$

$$V_{\alpha r} = R_r i_{\alpha r} + \frac{d\psi_{\alpha r}}{dt} + \omega_m \psi_{\beta r}$$
$$V_{\beta r} = R_r i_{\beta r} + \frac{d\psi_{\beta r}}{dt} - \omega_m \psi_{\alpha r} \qquad (3.29)$$

The flux of the stator and rotor can be calculated using the following formulas:

$$\psi_{\alpha s} = L_{\sigma s} i_{\alpha s} + L_m (i_{\alpha s} + i_{\alpha r})$$
$$\psi_{\beta s} = L_{\sigma s} i_{\beta s} + L_m (i_{\beta s} + i_{\beta r})$$
$$\psi_{\alpha r} = L_{\sigma r} i_{\alpha r} + L_m (i_{\alpha s} + i_{\alpha r})$$
$$\psi_{\beta r} = L_{\sigma r} i_{\beta r} + L_m (i_{\beta s} + i_{\beta r}) \qquad (3.30)$$

When equation (3.23) is substituted for equation (3.30), the result is:

$$\psi_{\alpha s} = L_s i_{\alpha s} + L_m i_{\alpha r}$$
$$\psi_{\beta s} = L_s i_{\beta s} + L_m i_{\beta r}$$
$$\psi_{\alpha r} = L_r i_{\alpha r} + L_m i_{\alpha s}$$
$$\psi_{\beta r} = L_r i_{\beta r} + L_m i_{\beta s} \qquad (3.31)$$

where $V_{\alpha s}$, $V_{\beta s}$, and $V_{\alpha r}$, $V_{\beta r}$, $i_{\alpha s}$, $i_{\beta s}$ and $i_{\alpha r}$, $i_{\beta r}$, and $\psi_{\alpha s}$, $\psi_{\beta s}$ and $\psi_{\alpha r}$, $\psi_{\beta r}$ are voltages [V], current [A] and flux linkage [Wb] of stator and rotor in the α and β axis respectively.

The stator and rotor active and reactive power in the αβ frame are computed as follows:

$$\begin{aligned} P_s &= 1.5(V_{\alpha s} i_{\alpha s} + V_{\beta s} i_{\beta s}) \\ P_r &= 1.5(V_{\alpha r} i_{\alpha r} + V_{\beta r} i_{\beta r}) \\ Q_s &= 1.5(V_{\beta s} i_{\alpha s} - V_{\alpha s} i_{\beta s}) \\ Q_r &= 1.5(V_{\beta r} i_{\alpha r} - V_{\alpha r} i_{\beta r}) \end{aligned} \tag{3.32}$$

where Ps and Pr, Qs, and QR are the active and reactive power of the stator and rotor, respectively.

The machine's electromagnetic torque (Tem) can be calculated using the following expressions:

$$\mathrm{Tem} = 1.5\left(\frac{\mathrm{L_m}}{\sigma \mathrm{L_r L_s}}\right) p \mathrm{I_m}\{\varphi_\mathrm{r}, \varphi_\mathrm{s}\} \tag{3.33}$$

where p is the pole pair of the machine and σ is the leakage coefficient.

ii) dq frame of reference

The transformation of two-phase orthogonal stationary frames of reference quantities (αβ) into two-phase rotating frames of reference is known as Park's transformation (dq). In the matrix, it's written as (A. Kumar, 2013):

$$\begin{bmatrix} i_d \\ i_q \end{bmatrix} = Tp(\theta)\begin{bmatrix} i_\alpha \\ i_\beta \end{bmatrix} \text{ and } \begin{bmatrix} V_d \\ V_q \end{bmatrix} = Tp(\theta)\begin{bmatrix} V_\alpha \\ V_\beta \end{bmatrix} \tag{3.34}$$

where transformation matrix, $Tp(\theta) = \begin{bmatrix} C\theta & S\theta \\ -S\theta & C\theta \end{bmatrix}$

Equation (3.34) is rewritten as follows:

$$\begin{bmatrix} i_d \\ i_q \end{bmatrix} = \begin{bmatrix} C\theta & S\theta \\ -S\theta & C\theta \end{bmatrix}\begin{bmatrix} i_\alpha \\ i_\beta \end{bmatrix} \text{ and } \begin{bmatrix} V_d \\ V_q \end{bmatrix} = \begin{bmatrix} C\theta & S\theta \\ -S\theta & C\theta \end{bmatrix}\begin{bmatrix} V_\alpha \\ V_\beta \end{bmatrix} \tag{3.35}$$

Figure 3.9 shows the dynamic equivalent circuit of DFIG in the dq frame of reference.

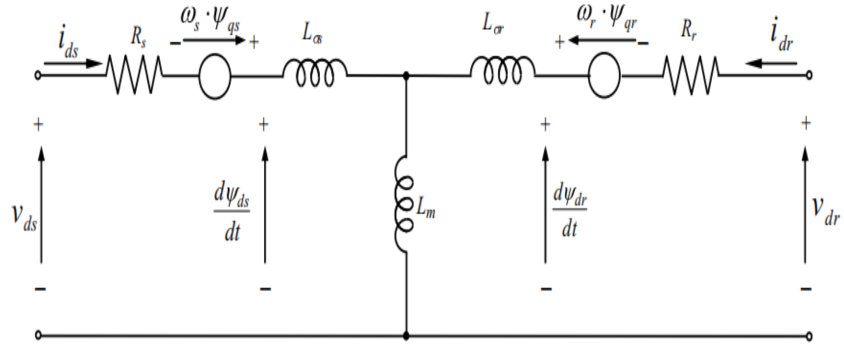

(a) Equivalent Circuit of DFIG in d-axis

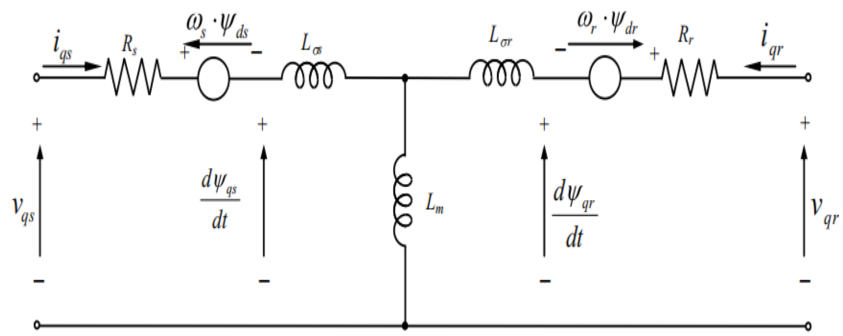

(b) Equivalent Circuit of DFIG in q-axis

Figure 3.9: Equivalent Circuit of DFIG in dq Frame of Reference (A. Kumar, 2013)

Based on Figure 3.9, the voltage equations for the stator and rotor are given as follows:

$$\begin{aligned} V_{ds} &= R_s i_{ds} + \frac{d\psi_{ds}}{dt} - \omega_s \psi_{qs} \\ V_{qs} &= R_s i_{qs} + \frac{d\psi_{qs}}{dt} + \omega_s \psi_{ds} \\ V_{dr} &= R_r i_{dr} + \frac{d\psi_{dr}}{dt} - \omega_r \psi_{qr} \\ V_{qr} &= R_r i_{qr} + \frac{d\psi_{qr}}{dt} + \omega_r \psi_{dr} \end{aligned} \tag{3.36}$$

The flux of the stator and rotor can be calculated using the following formulas:

$$\begin{aligned} \psi_{ds} &= L_{\sigma s} i_{ds} + L_m (i_{ds} + i_{dr}) \\ \psi_{qs} &= L_{\sigma s} i_{qs} + L_m (i_{qs} + i_{qr}) \\ \psi_{dr} &= L_{\sigma r} i_{dr} + L_m (i_{ds} + i_{dr}) \\ \psi_{qr} &= L_{\sigma r} i_{qr} + L_m (i_{qs} + i_{qr}) \end{aligned} \tag{3.37}$$

When equation (3.23) is substituted for equation (3.37), the result is:

$$\begin{aligned} \psi_{ds} &= L_s i_{ds} + L_m i_{dr} \\ \psi_{qs} &= L_s i_{qs} + L_m i_{qr} \\ \psi_{dr} &= L_r i_{dr} + L_m i_{ds} \\ \psi_{qr} &= L_r i_{qr} + L_m i_{qs} \end{aligned} \tag{3.38}$$

The stator and rotor active and reactive power in the dq frame are computed as follows:

$$\begin{aligned} P_s &= 1.5(V_{ds} i_{ds} + V_{qs} i_{qs}) \\ P_r &= 1.5(V_{dr} i_{dr} + V_{qr} i_{qr}) \\ Q_s &= 1.5(V_{qs} i_{ds} - V_{ds} i_{qs}) \\ Q_r &= 1.5(V_{qr} i_{dr} - V_{dr} i_{qr}) \end{aligned} \tag{3.39}$$

where V_{ds}, V_{qs} and V_{dr}, V_{qr}, i_{ds}, i_{qs} and i_{dr}, i_{qr}, and ψ_{ds}, ψ_{qs} and ψ_{dr}, ψ_{qr} and are voltages [V], current [A], and flux linkage [Wb] of the stator and rotor in the d and q axis, respectively.

The electromagnetic torque equation is:

$$T_{em} = \frac{3}{2} p(\psi_{dr} i_{qs} - \psi_{qr} i_{ds}) = \frac{3}{2} pLm(i_{dr} i_{qs} - i_{qr} i_{ds}) \tag{3.40}$$

3.8. Power Converter Model

Power converters are frequently used in wind energy conversion systems due to their high transmission capacity of the electricity generated by wind turbines to the grid as well as their quick and accurate responses. These converters are employed in fixed-speed WECS to avoid torque oscillations and inrush current during the system's starting. Variable speed WECS, on the other hand, uses these converters to control the generator torque and speed, as well as active and reactive power transported to the grid independently. DFIG-based WECS employs back-to-back converters (i.e., RSC and GSC) connected by a DC Link (GANTHIA et al., 2021).

3.8.1. Rotor Side Converter (RSC)

A rotor-side converter is a converter that is coupled to the generator's rotor winding as shown in Figure 3.10. RSC acts as either an inverter or rectifier, depending on the rotor speed. During the super-synchronous mode of operation of DFIG, it operates as a PWM rectifier, whereas during the sub-synchronous mode of operation, it acts as a PWM inverter. The major goal of this converter is to maintain the active power and torque of the generator under control. In addition, it is also in charge of managing the reactive power that is supplied to the grid (Jagadeeshwaran & Kumar, 2017).

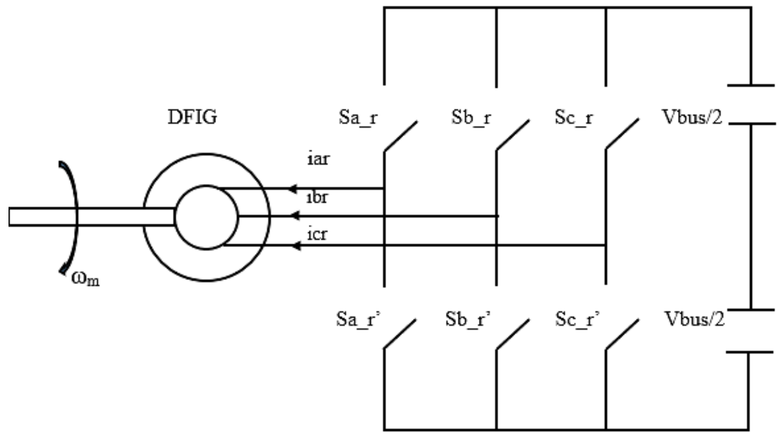

Figure 3.10: Rotor Side Converter (Ganthia, 2020)

DC at the rotor terminal, irdc, is given by:

$$i_{rdc} = -S_{a\_r} i_{ar} - S_{b\_r} i_{br} - S_{c\_r} i_{cr} \tag{3.41}$$

3.8.2. Grid Side Converter (GSC)

A grid-side converter is a converter that is connected between RSC and the grid. The major goal of this converter is to maintain the DC link voltage constant. Furthermore, it is also in charge of managing the reactive power exchange (Ganthia, 2020).

Similar to RSC, GSC can operate as an inverter or a rectifier depending on the rotor speed. In the sub-synchronous mode of operation, the voltage across the DC link terminal decreases since the rotor is powered by the capacitor on the DC link. As a result, power flows from the grid to the capacitor. In this scenario, the GSC serves as a rectifier. In contrast, when the system is in a super synchronous mode of operation, the rotor supplies the capacitor, increasing its voltage. As a result, power is transferred from the rotor to the grid via GSC. In this case, the GSC serves as the an inverter (Jagadeeshwaran & Kumar, 2017). As shown in Figure 3.11, the grid-side system includes GSC, filters, and a grid.

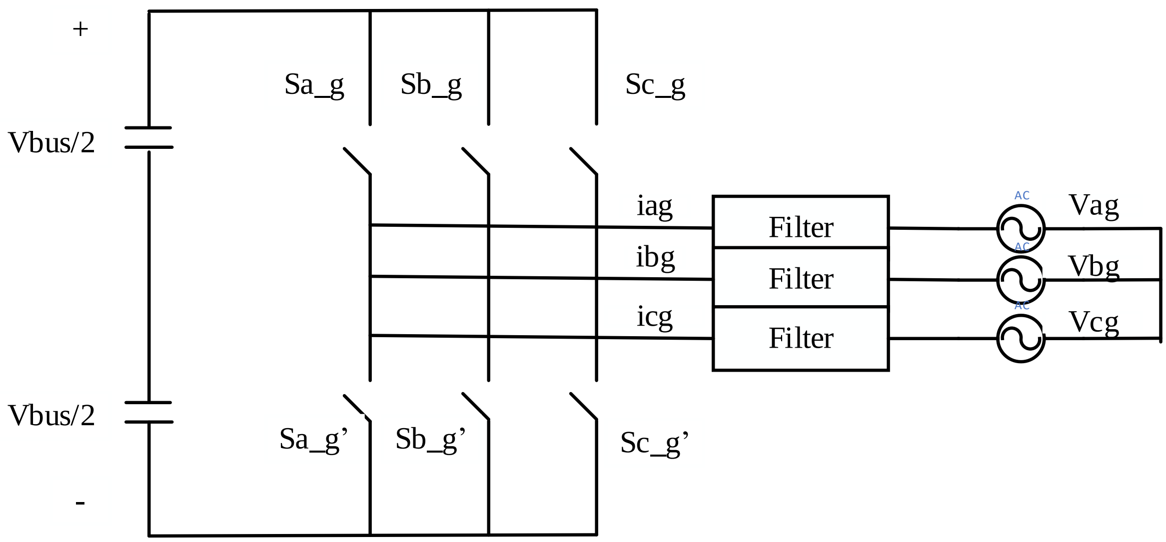

Figure 3.11: Simplified Converter, Filter, and Grid Model (Berhanu et al., 2018b)

The following assumptions are taken into account while modeling grid-side converters (Singh, 2015).

- Ideal bidirectional switches, which allow current to flow in both directions, are used to model the grid-side converter. This makes it possible to transfer power in both modes (either in rectifier mode or inverter mode).
- The grid-side filter, which connects the converter to the grid, is usually composed of inductances and resistors.
- To simplify the system for analysis, an ideal transformer and transmission line is utilized.

There are eight possible combinations of output voltages based on the Sag, Sbg, and Scg's permitted switching states, as listed in Table 3.1. Two switches within the same leg cannot be activated simultaneously to avoid short circuits. Therefore, as shown by the equations below, the relationship between these switches is complimentary.

$$\begin{aligned} S_{a\_g} + S'_{a\_g} &= 1 \\ S_{b\_g} + S'_{b\_g} &= 1 \\ S_{c\_g} + S'_{c\_g} &= 1 \end{aligned} \tag{3.42}$$

The following equation provides the voltage reference to the DC bus' zero point:

$$V_{jo} = V_{bus} S_{j\_g} \tag{3.43}$$

where Sj_g ϵ {0,1} and j = a, b and c

$$\begin{aligned} V_{ao} &= V_{bus} S_{a\_g} \\ V_{bo} &= V_{bus} S_{b\_g} \\ V_{co} &= V_{bus} S_{c\_g} \end{aligned} \tag{3.44}$$

The following formulas are used to calculate the converter output voltages referred to as the grid's three-phase system's neutral point (n):

$$\begin{aligned} V_{an} &= V_{ao} - V_{no} \\ V_{bn} &= V_{bo} - V_{no} \\ V_{cn} &= V_{co} - V_{no} \end{aligned} \tag{3.45}$$

Assume that, under normal operating conditions, the grid AC voltage is balanced and sinusoidal.

$$V_{an} + V_{bn} + V_{cn} = 0 \tag{3.46}$$

By substituting equation (3.45) into (3.46), the relationship between voltages at the neutral point (n) and the zero point of the DC bus (o) can be obtained as follows:

$$V_{no} = \frac{1}{3}(V_{ao} + V_{bo} + V_{co}) \tag{3.47}$$

Inserting equation (3.47) into equation (3.45) results:

$$\begin{aligned} V_{an} &= \frac{2}{3}V_{ao} - \frac{1}{3}(V_{bo} + V_{co}) \\ V_{bn} &= \frac{2}{3}V_{bo} - \frac{1}{3}(V_{ao} + V_{co}) \\ V_{cn} &= \frac{2}{3}V_{co} - \frac{1}{3}(V_{ao} + V_{bo}) \end{aligned} \tag{3.48}$$

Inserting equation (3.44) into equation (3.48) results:

$$\begin{aligned} V_{an} &= \frac{V_{bus}}{3}(2S_{a\_g} - S_{b\_g} - S_{c\_g}) \\ V_{bn} &= \frac{V_{bus}}{3}(2S_{b\_g} - S_{a\_g} - S_{c\_g}) \\ V_{cn} &= \frac{V_{bus}}{3}(2S_{c\_g} - S_{a\_g} - S_{b\_g}) \end{aligned} \tag{3.49}$$

Table 3.1: Different Grid-Side Converter Output Voltage Combinations

S_{a_g}	S_{b_g}	S_{c_g}	V_{ao}	V_{bo}	V_{co}	V_{an}	V_{bn}	V_{cn}
0	0	0	0	0	0	0	0	0
0	0	1	0	0	V_{bus}	$-\frac{1}{3}V_{bus}$	$-\frac{1}{3}V_{bus}$	$\frac{2}{3}V_{bus}$
0	1	0	0	V_{bus}	0	$-\frac{1}{3}V_{bus}$	$\frac{2}{3}V_{bus}$	$-\frac{1}{3}V_{bus}$
0	1	1	0	V_{bus}	V_{bus}	$-\frac{2}{3}V_{bus}$	$\frac{1}{3}V_{bus}$	$\frac{1}{3}V_{bus}$
1	0	0	V_{bus}	0	0	$\frac{2}{3}V_{bus}$	$-\frac{1}{3}V_{bus}$	$-\frac{1}{3}V_{bus}$
1	0	1	V_{bus}	0	V_{bus}	$\frac{1}{3}V_{bus}$	$-\frac{2}{3}V_{bus}$	$\frac{1}{3}V_{bus}$
1	1	0	V_{bus}	V_{bus}	0	$\frac{1}{3}V_{bus}$	$\frac{1}{3}V_{bus}$	$-\frac{2}{3}V_{bus}$
1	1	1	V_{bus}	V_{bus}	V_{bus}	0	0	0

DC at the grid terminal, igdc can be computed as:

$$i_{gdc} = S_{a\_g} i_{ag} + S_{b\_g} i_{bg} + S_{c\_g} i_{cg} \qquad (3.50)$$

3.9. Filter Model

As shown in Figure 3.11, a filter is placed in between the GSC and grid. The purpose of this filter is to minimize the voltage and current harmonics generated when the converter switches. There are various topologies of filters due to the different characteristics of converters. Among these, an inductive or L filter is considered in the modeling and simulation of this study. It is a type of filter that contain inductive filter (Lf) with resistance (Rf). This type of filter is selected since it is simple to design and also has very low ripple factor (Muluneh & Teame, 2021).

The three-phase system can be described as three independent but equivalent single-phase systems. Figure 3.12 shows a simplified equivalent single-phase grid circuit in “a” phase.

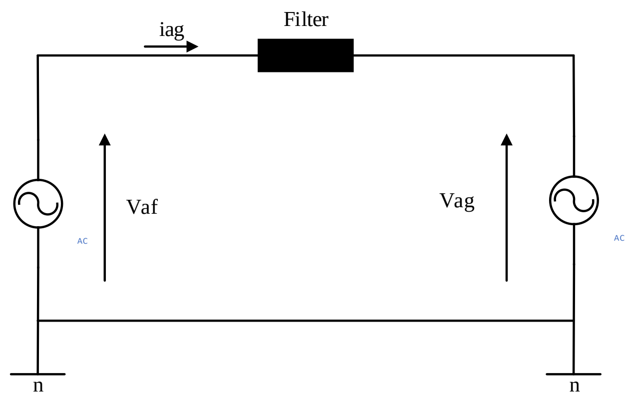

Figure 3.12: Simplified Equivalent Single-Phase Grid Circuit (a phase) (Abad, 2017)

The voltage across the filter is given by:

$$
\begin{aligned}
V_{af} &= R_f i_{ag} + L_f \frac{di_{ag}}{dt} + V_{ag} \\
V_{bf} &= R_f i_{bg} + L_f \frac{di_{bg}}{dt} + V_{bg} \\
V_{cf} &= R_f i_{cg} + L_f \frac{di_{cg}}{dt} + V_{cg}
\end{aligned}
\tag{3.51}
$$

It is possible to rewrite the equation (3.51) as follows:

$$
\begin{aligned}
\frac{di_{ag}}{dt} &= \frac{1}{L_f} * (V_{af} - R_f i_{ag} - V_{ag}) \\
\frac{di_{bg}}{dt} &= \frac{1}{L_f} * (V_{bf} - R_f i_{bg} - V_{bg}) \\
\frac{di_{cg}}{dt} &= \frac{1}{L_f} * (V_{cf} - R_f i_{cg} - V_{cg})
\end{aligned}
\tag{3.52}
$$

where L_f and R_f are inductance [H] and resistance [Ω] of the grid side filter, V_{ag}, V_{bg}, and V_{cg} are grid voltages [V], i_{ag}, i_{bg}, and i_{cg} are currents flowing through the GSC [A], V_{af}, V_{bf}, and V_{cf} are output voltages of filter [V], and Sa_g, Sb_g, and Sc_g are GSC switch signals.

3.10. DC Link Model

It is a connection between the RSC and the GSC, as shown in Figure 3.13, that makes use of the capacitor's energy to keep the voltage on its terminal constant. This model describes the fluctuations in DC link capacitor voltage as a function of its input power (Berhanu et al., 2018b).

The energy stored, W_{dc}, is given by:

$$W_{dc} = \int P_{dc} dt = \frac{1}{2} C V_{dc}^{\ 2} \tag{3.53}$$

where P_{dc} is the DC link's input power, V_{dc} is the voltage at the DC link, and C is the capacitance of the capacitor.

The input power to DC link can be calculated as:

$$P_{dc} = P_{in} - P_c = \frac{dW_{dc}}{dt} \tag{3.54}$$

where P_{in} refers to the RSC's input power and P_c represents the GSC's output power.

The DC link voltage, V_{bus}, is given by:

$$V_{bus} = \frac{1}{C_{bus}} \int i_c dt \tag{3.55}$$

where C_{bus} is the DC Link capacitance and i_c is the capacitance current.

The following equation is used to obtain the current through the capacitance:

$$i_c = i_{r\_dc} - i_{g\_dc} - i_{res} \tag{3.56}$$

where i_{g_dc} denotes direct current flowing from the DC link to the grid [A], i_{r_dc} denotes direct current that flows from the rotor to the DC link [A], and i_{res} denotes current in the resistance [A].

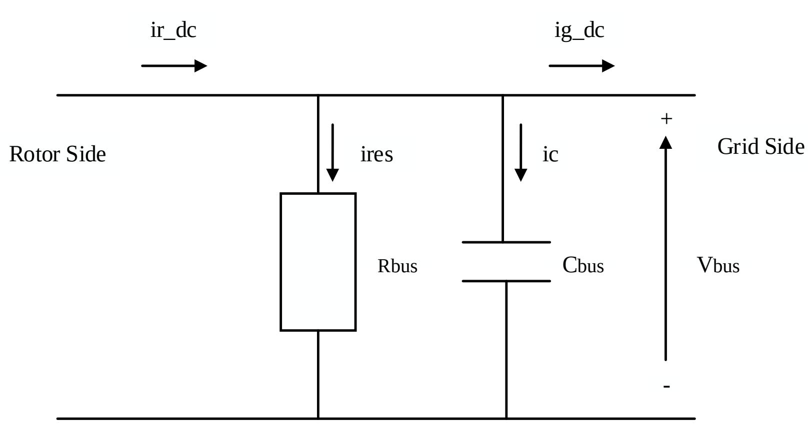

Figure 3.13: DC Link System (Berhanu et al., 2018b)

On the other hand, the rotor and grid Direct Currents (DCs) can be calculated as follows:

$$\begin{aligned} i_{r\_dc} &= -s_{a\_r} i_{ar} - s_{b\_r} i_{br} - s_{c\_r} i_{cr} \\ i_{g\_dc} &= s_{a\_g} i_{ag} + s_{b\_g} i_{bg} + s_{c\_g} i_{cg} \end{aligned} \qquad (3.57)$$

where Sa_g, Sb_g, and Sc_g are GSC's switch signals and Sa_r, Sb_r, and Sc_r are RSC's switch signals.

The following equation is used to obtain the current flow through the resistor.

$$i_{res} = \frac{V_{bus}}{R_{bus}} \qquad (3.58)$$

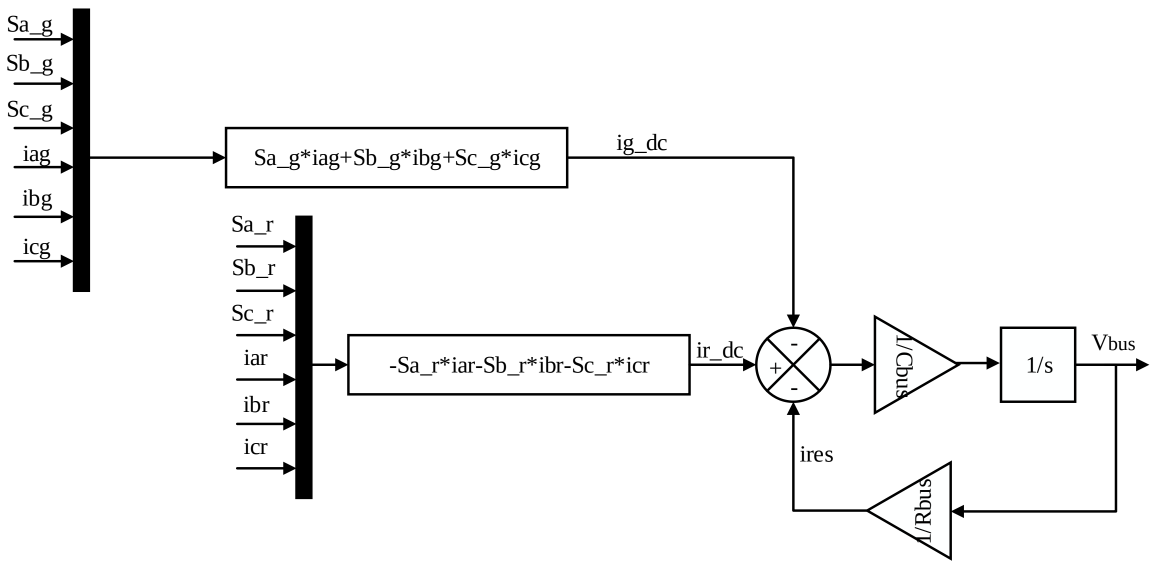

Figure 3.14: DC Link Model (Berhanu et al., 2018b)

3.11. Double Fed Induction Generator (DFIG) Control

It is employed to control the performance of power converters and DFIG during both normal and abnormal operating conditions (such as voltage dips, voltage swells, harmonics, and so on). The presence of excessive current at the rotor terminal due to these grid disturbances damages power converters and the DC Link capacitor. Therefore, the implementation of an effective control mechanism is required to avoid the occurrence of such a problem. The Vector Control (VC) technique is the most widely used controlling mechanism for grid-connected WECS. It is also termed "field-oriented control" (Kumhar, 2018).

To make the control procedure easier, the reference frame is transformed into the dq axis. Based on the orientation of the reference frame, VC can be divided into two main categories. These are Stator Flux Oriented Vector Control (SFOVC) and Grid Voltage Oriented Vector Control (GVOVC). SFOVC is a VC that is used when the direct axis is aligned with the stator flux, whereas GVOVC is used when it is aligned with the grid voltage. In this thesis, SFOVC is used in RSC while GVOVC is used in GSC (Agha Kashkooli et al., 2020). This control strategy is employed in combination with other controllers like ANFIS, to make the controller's performance more effective and accurate. The major benefits of the VC strategy include ease of parameter implementation, high accuracy, good response during faults, fixed switching frequency, etc (Kumhar, 2018).

3.11.1. Vector Control of Rotor Side Converter

As already mentioned, Vector Control is utilized in RSC to individually control the rotor's active and reactive power. To archive this, voltages and currents are converted into a dq frame of reference with the direct axis lined up with the stator flux as indicated in Figure 3.15. This happens because of the direct connection between the DFIG's stator and the grid. As a result, ψ_s is constant and ψ_{qs} is equal to zero (J. Chen et al., 2016).

$$\psi_s = \psi_{ds} = const, \frac{d\psi_{ds}}{dt} = 0 \tag{3.59}$$

$$\psi_{qs} = 0, \frac{d\psi_{qs}}{dt} = 0 \tag{3.60}$$

By neglecting the small drop in stator resistance, equation (3.36) becomes:

$$\begin{aligned} V_{ds} &= 0 \\ V_{qs} &= V_g \approx \omega_s \psi_s \end{aligned} \tag{3.61}$$

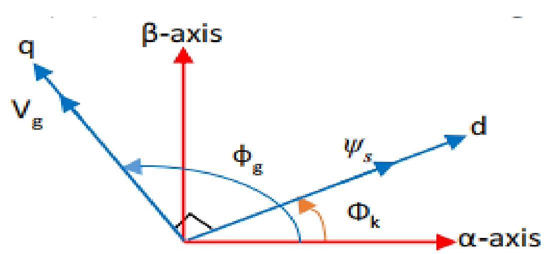

Figure 3.15: Vector Control of the d-q Reference Aligned with Stator Flux Space Vector (Tuka & Leidhold, 2017)

Equation (3.38) can be also rewritten as:

$$\begin{aligned} \psi_{ds} &= L_s i_{ds} + L_m i_{dr} = \psi_s \\ \psi_{qs} &= L_s i_{qs} + L_m i_{qr} = 0 \end{aligned} \tag{3.62}$$

From equation (3.62), the dq-axis stator currents can be calculated as follows:

$$\begin{aligned} i_{ds} &= \frac{\psi_s - L_m i_{dr}}{L_s} = \frac{V_g}{\omega_s L_s} - \frac{L_m}{L_s} i_{dr} \\ i_{qs} &= -\frac{L_m}{L_s} i_{qr} \end{aligned} \tag{3.63}$$

When the d-axis is aligned with the stator flux, the voltage aligns with the quadrature axis. As a result, Vds = 0 and Vqs = Vg. When these values are substituted into equation (3.39), it results:

$$\begin{aligned} P_s &= \frac{3}{2} * V_g * i_{qs} \\ Q_s &= \frac{3}{2} * V_g * i_{ds} \end{aligned} \tag{3.64}$$

Substituting equation (3.63) into equation (3.64):

$$\begin{aligned} P_s &= -\frac{3}{2} V_g \frac{L_m}{L_s} i_{qr} \\ Q_s &= \frac{3}{2} V_g \left[\frac{\psi_s - L_m i_{dr}}{L_s} \right] \end{aligned} \tag{3.65}$$

According to equation (3.65), independent control of the stator’s active and reactive power is archived by controlling the rotor current. The rotor currents in d and q axis can be also derived from this equation, as follows:

$$\begin{aligned} i_{dr} &= \frac{V_g}{L_m \omega_s} - \frac{2}{3} \frac{L_s Q_s *}{V_g L_m} \\ i_{qr} &= -\frac{2}{3} \frac{L_s}{L_m V_g} P_s * \end{aligned} \tag{3.66}$$

3.11.2. Vector Control of Grid Side Converter

In contrast to RSC, GSC is controlled by employing the Grid Voltage Oriented Vector Control approach (GVOVC). Due to the grid voltage's alignment with the synchronous frame's d axis, its q-axis component has a value of zero (Berhanu et al., 2018b).

$$\begin{aligned} P_g &= 1.5*(V_{dg}i_{dg} + V_{qg}i_{qg}) \\ Q_g &= 1.5*(V_{qg}i_{dg} - V_{dg}i_{qg}) \end{aligned} \tag{3.67}$$

For Vqg = 0, equation (3.67) becomes:

$$\begin{aligned} P_g &= 1.5V_{dg}i_{dg} \\ Q_g &= -1.5V_{dg}i_{qg} \end{aligned} \tag{3.68}$$

Where Vdg, Vqg, idg, and iqg represent grid voltages [V] and current [A] in the d and q axes, respectively.

By adjusting the grid current in the d and q-axes, it is possible to independently regulate the grid's active and reactive power, similar to RSC. The reference grid currents in the d and q-axes are obtained from Equation (3.68) as follows:

$$\begin{aligned} i_{dg}* &= \frac{2}{3}*\frac{P_g*}{V_{dg}} \\ i_{qg}* &= -\frac{2}{3}*\frac{Q_g*}{V_{dg}} \end{aligned} \tag{3.69}$$

3.12. Controllers Design

3.12.1. Proportional Integral (PI) Controller

The PI controller is utilized in combination with vector control for minimizing errors and optimizing the process output. In this thesis, it is employed to regulate the DC link voltage and rotor currents so that the actual values of each component track their reference values. Since PID has poor performance for integral processes, significant time delays, high overshoots, and settling times, using a PI controller is preferable (Mohammadi et al., 2017).

3.12.1.1. Proportional Integral (PI) Controller Design for Rotor Side Converter

When a fault, such as a voltage dip, occurs on the grid side, the actual values of rotor currents deviate from their reference values. This may cause some serious damage to the RSC due to the increase in rotor current beyond the limit. Therefore, the PI controller is utilized to avoid the occurrence of such a problem by minimizing the error. To maintain its performance at its optimum value the controller parameters, (i.e., Kpi and Kii) must be designed properly (GONZALO ABAD, 2017).

The voltages at the rotor terminal are given by:

$$\begin{aligned} V_{dr} &= R_r i_{dr} - \omega_r \sigma L_r i_{qr} + \sigma L_r \frac{d}{dt} i_{dr} \\ V_{qr} &= R_r i_{qr} + \omega_r \sigma L_r i_{dr} + \sigma L_r \frac{d}{dt} i_{qr} \end{aligned} \tag{3.70}$$

Let,

$$\begin{aligned} e_1 &= -\omega_r \sigma L_r i_{qr} \\ e_2 &= \omega_r \sigma L_r i_{dr} \end{aligned} \tag{3.71}$$

Substituting equation (3.71) into equation (3.70):

$$\begin{aligned} V_{dr} &= R_r i_{dr} + \sigma L_r \frac{d}{dt} i_{dr} + e_1 \\ V_{qr} &= R_r i_{qr} + \sigma L_r \frac{d}{dt} i_{qr} + e_2 \end{aligned} \tag{3.72}$$

The laplace transform of equation (3.72) is given by:

$$\begin{aligned} V_{dr}(s) &= R_r i_{dr}(s) + s\sigma L_r i_{dr}(s) + e_1(s) \\ V_{qr}(s) &= R_r i_{qr}(s) + s\sigma L_r i_{qr}(s) + e_2(s) \end{aligned} \tag{3.73}$$

Equation (3.73) can be written in terms of current as follows:

$$\begin{aligned} i_{dr}(s) &= \frac{(V_{dr}(s) - e_1(s))}{R_r + s\sigma L_r} \\ i_{qr}(s) &= \frac{(V_{qr}(s) - e_2(s))}{R_r + s\sigma L_r} \end{aligned} \tag{3.74}$$

Assume that there is the ideal decoupling effect of the back-emf, the plant model is given by:

$$\frac{i_{dr}(s)}{V_{dr}(s)} = \frac{i_{qr}(s)}{V_{qr}(s)} = \frac{1}{R_r + s\sigma L_r} \tag{3.75}$$

On the other hand, the d and q-axis rotor current control loop form:

$$\frac{V_{dr}(s)}{e_{dr}(s)} = \frac{V_{qr}(s)}{e_{qr}(s)} = (Kpi + \frac{Kii}{s}) \tag{3.76}$$

Where $\begin{matrix} e_{dr}(s) = i_{dr}*(s) - i_{dr}(s) \\ e_{qr}(s) = i_{qr}*(s) - i_{qr}(s) \end{matrix}$

Equation (3.76) can be rewritten as:

$$\begin{aligned} V_{dr}(s) &= (Kpi + \frac{K_{ii}}{s})*(i_{dr}* - i_{dr}) \\ V_{qr}(s) &= (Kpi + \frac{K_{ii}}{s})*(i_{qr}* - i_{qr}) \end{aligned} \tag{3.77}$$

Equating equations (3.75) and (3.77)

$$\begin{aligned} V_{dr}(s) = (R_r + s\sigma L_r)i_{dr} &= \left(Kpi + \frac{K_{ii}}{s}\right)(i_{dr}* - i_{dr}) \\ V_{qr}(s) = (R_r + s\sigma L_r)i_{qr} &= \left(Kpi + \frac{K_{ii}}{s}\right)(i_{qr}* - i_{qr}) \end{aligned} \tag{3.78}$$

The transfer function between the actual and reference rotor current is given by:

$$\frac{i_{dr}(s)}{i_{dr}*(s)} = \frac{i_{qr}(s)}{i_{qr}*(s)} = \frac{sKpi + Kii}{s^2 + s\left(\frac{R_r + Kpi}{\sigma L_r}\right) + \frac{Kii}{\sigma L_r}} \tag{3.79}$$

Where Kpi and Kii are the parameters of the PI controller for controlling the current across the rotor terminal.

Parameters of the PI controller are obtained by equating the denominator of equation (3.79) with the second order standard denominator of classical control theories.

$$s^2 + s\left(\frac{R_r + Kpi}{\sigma L_r}\right) + \frac{Kii}{\sigma L_r} = s^2 + 2\xi\omega_n s + \omega_n^2 \tag{3.80}$$

Assuming $\xi = 1$, that the value of Kpi and Kii is obtained by:

$$\begin{aligned} Kpi &= 2\omega_n \sigma L_r - R_r \\ Kii &= \omega_n^2 \sigma L_r \end{aligned} \tag{3.81}$$

3.12.1.2. Proportional Integral (PI) Controller Design for Grid Side Converter

The occurrence of faults like voltage dip at the grid side prevents the power flow from the system to the grid. This may result in the concentration of high voltage across the DC Link terminal**.** There are three PI controllers in the GSC. One is responsible for controlling the voltage at the DC Link terminal, whereas the remaining two are employed to regulate grid current in the d and q-axes. The PI controller parameters for controlling the grid current are obtained as follows (Abad, 2017):

The d and q-axis components of grid voltage are given by:

$$\begin{aligned} V_{df} &= R_f i_{dg} - \omega_e L_f i_{qg} + L_f \frac{d}{dt} i_{dg} \\ V_{qf} &= R_f i_{qg} + \omega_e L_f i_{dg} + L_f \frac{d}{dt} i_{qg} \end{aligned} \tag{3.82}$$

Where Vdg and Vqg are the grid voltages [V] in the d-q axis, idg and iqg are the grid currents [A] in the d-q axis, ω_e is the electrical angular velocity of the grid voltage [rad/s].

Similar to that of RSC control, the equation that relates voltage to the current can be obtained as follows:

$$\begin{aligned} V_{df} &= (R_f i_{dg} + L_f \frac{d}{dt} i_{dg}) \\ V_{qf} &= (R_f i_{qg} + L_f \frac{d}{dt} i_{qg}) \end{aligned} \tag{3.83}$$

Laplace transform of equation 3.83 is given as:

$$\frac{i_{dg}(s)}{V_{df}(s)} = \frac{i_{qg}(s)}{V_{qf}(s)} = \frac{1}{R_f + sL_f} \tag{3.84}$$

On the other hand, the d and q-axis grid current control loop forms:

$$\frac{V_{df}(s)}{e_{dg}(s)} = \frac{V_{qf}(s)}{e_{qg}(s)} = \left(Kp_g + \frac{Ki_g}{s} \right) \tag{3.85}$$

Where $\begin{aligned} e_{dg}(s) &= i_{dg}*(s) - i_{dg}(s) \\ e_{qg}(s) &= i_{qg}*(s) - i_{qg}(s) \end{aligned}$

Equation (3.85) can be rewritten as:

$$V_{df}(s) = \left(Kp_g + \frac{Ki_g}{s} \right)(i_{dg}* - i_{dg})$$
$$V_{qf}(s) = \left(Kp_g + \frac{Ki_g}{s} \right)(i_{qg}* - i_{qg}) \qquad (3.86)$$

Equating equations (3.84) and (3.86)

$$V_{df}(s) = (R_f + sL_f)i_{dg} = \left(Kp_g + \frac{Ki_g}{s} \right)(i_{dg}* - i_{dg})$$
$$V_{qf}(s) = (R_f + sL_f)i_{qg} = \left(Kp_g + \frac{Ki_g}{s} \right)(i_{qg}* - i_{qg}) \qquad (3.87)$$

The transfer function between the actual and reference grid current is given by:

$$\frac{i_{dg}(s)}{i_{dg}*(s)} = \frac{i_{qg}(s)}{i_{qg}*(s)} = \frac{\left(\frac{1}{L_f}\right)(sKp_g + Ki_g)}{s^2 + s\left(\frac{Kp_g + R_f}{L_f}\right) + \frac{Ki_g}{L_f}} \qquad (3.88)$$

Where Kpg and Kig are the parameters of the PI controller for controlling the current along the grid terminal.

Parameters of PI controller are obtained by equating the denominator of equation (3.88) with the second order standard denominator of classical control theories.

$$s^2 + s\left(\frac{Kp_g + R_f}{L_f}\right) + \frac{Ki_g}{L_f} = s^2 + 2\xi\omega_n s + \omega_n{}^2 \qquad (3.89)$$

Assuming $\xi = 1$, that the values of Kpg and Kig are obtained by:

$$Kp_g = 2\omega_n L_f - R_f$$
$$Ki_g = \omega_n{}^2 L_f \qquad (3.90)$$

Similarly, the PI controller parameters for controlling the DC Link voltage are obtained as follows.

The DC Link Voltage, Vdc, can be computed as:

$$V_{dc} = \frac{1}{C}\int i_c dt \qquad (3.91)$$

The current across the DC Link terminal, idc, can be calculated as:

$$i_{dc} = C\frac{dV_{dc}}{dt} \tag{3.92}$$

Where C is DC Link's capacitance.

Laplace transform of equation (3.92) becomes:

$$i_{dc}(s)^* = sCV_{dc}(s) \tag{3.93}$$

The voltage at the DC Link terminal can be controlled similarly to the rotor and grid current.

$$i_{dc}{}^*(s) = \left(Kp_v + \frac{Ki_v}{s}\right)\left(V_{dc}{}^* - V_{dc}\right) \tag{3.94}$$

Equating equations (3.93) and (3.94):

$$i_{dc}{}^*(s) = sCV_{dc}(s) = \left(Kp_v + \frac{Ki_v}{s}\right)\left(V_{dc}{}^* - V_{dc}\right) \tag{3.95}$$

The transfer function between the actual and reference DC Link voltage is given by:

$$\frac{V_{dc}}{V_{dc}{}^*} = \frac{\left(\frac{1}{C}\right)\left(sKp_v + Ki_v\right)}{s^2 + \frac{Kp_v}{C}s + \frac{Ki_v}{C}} \tag{3.96}$$

where Kpv and Kiv are the PI controller's parameters for regulating the DC Link voltage.

By equating the denominator of equation (3.96) to the denominator of a standard second-order characteristic equation, the value of Kpv and Kiv becomes:

$$\begin{aligned} Kp_v &= 2\omega_n C \\ Ki_v &= \omega_n{}^2 C \end{aligned} \tag{3.97}$$

3.12.1.3. Anti-Windup (AW)

In a PI control, due to the integrator, the saturation phenomenon that practically occurs in all control systems will bring a nonlinear effect which is called wind up. The PI controller of actual systems in a plant is typically modeled as a linear system. However, since linear PI controllers lack output magnitude limiters, the output can take on quite high values. As a result, the real system may be damaged by the large control action. Therefore, the maximum integrator output value must be kept within the limits in order to prevent the undesirable windup phenomenon. This strategy is referred as Anti-Windup (AW). The main objective of the AW scheme or saturation limiters to prevent the overvalue in the Integrator; therefore, the Integration output will be kept within a specific range. For the PI controller, the Anti Windup gain, Kt=1/Ti (Gomez et al., 2020).

Figure 3.16 shows a block diagram of a PI controller with AW. The system has an extra path that is generated by measuring the actual actuator's output and forming error signal (es). This signal is fed to the integrator's input through Kt.

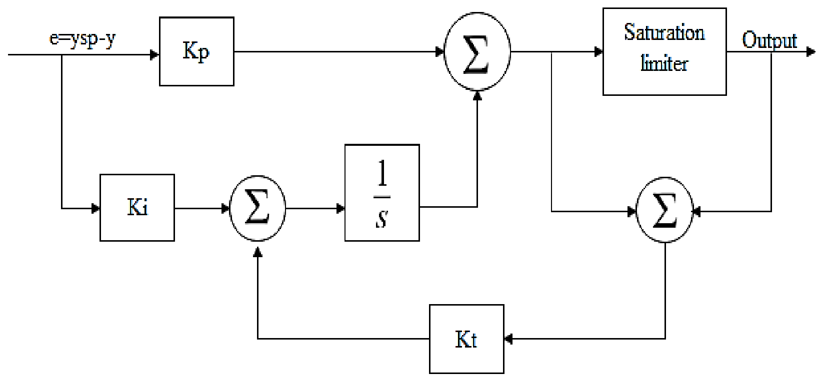

Figure 3.16: PI Controller with Anti-Windup (AW) (Rashid & Hasan, 2017)

The difference between the actual and reference value (i.e., error) is given to the PI controller whose output is used as an input for the AW scheme. When there is no saturation (i.e, es=0), the additional feedback does not affect the normal operation of the system. However, when the error is different from zero, it will pass through the integral feedback path until it becomes zero.

Although the PI controllers are capable of meeting the control requirement in a normal operating environment, the system's performance will deteriorate when disturbances like voltage dip occur. As a result, to avoid the occurrence of such issue, in this thesis, ANFIS is used to replace the traditional PI controller in the regulation of rotor current and DC link voltage. This controller is preferred over the PI controller because it is robust and also has the best performance in fault cases (Merahi & Berkouk, 2016).

3.12.2. Overview of Fuzzy Logic Controller (FLC)

There are three main stages while designing the FLC as illustrated in Figure 3.17. These are fuzzification, Fuzzy Inference System (FIS), and Defuzzification (Rached et al., 2019).

Figure 3.17: General Structure of FLC (Rached et al., 2019)

i. Fuzzification

It is a process of obtaining a membership function (MF) and converting real values (crisp inputs) to fuzzy values. There are several MFS that are used during this process. These are triangular, trapezoidal, Gaussian, and the like (Rached et al., 2019).

ii. Fuzzy Inference System (FIS)

A Fuzzy Inference System (FIS) is used to develop a relationship between fuzzy input and output by building IF-THEN rules. Mamdani and Sugeno inference system are the main types of FIS. The critical difference between them is based on the defuzzification technique they employ. The Center of Gravity (COG) is used by the Mamdani type FIS to defuzzify fuzzy output and produce a crisp output. On the other hand, Sugeno-type FIS computes the crisp output using a weighted average (Rached et al., 2019).

iii. Defuzzification

The process of converting the fuzzy output to a crisp output is called defuzzification (Rached et al., 2019). Inspite of its numerous advantages, the main drawback of this controller is that it necessitates expert knowledge in order to determine the input and output ranges as well as the rules. To address these FLC limitations, an ANFIS controller is used in this thesis.

3.12.3. Adaptive Neuro Fuzzy Inference System (ANFIS) Controller

ANFIS is a type of neural network which is designed based on sugeno FIS. It combines the best features of neural networks (NN) and FLC into a single framework. The structure of the network is composed of five interconnected layers (Rezaie et al., 2018). Figure 3.18 depicts the single-input, single-output ANFIS structure.

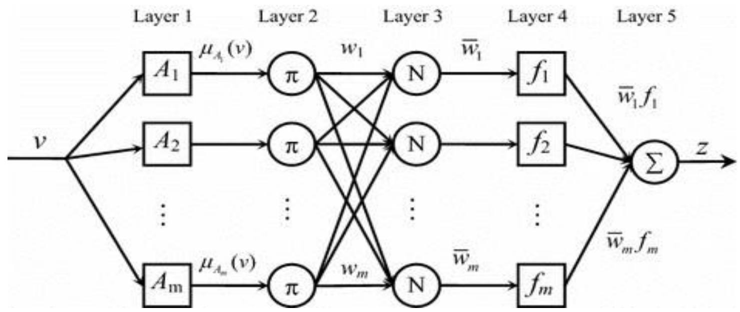

Figure 3.18: ANFIS Structure (Rezaie et al., 2018)

Layer 1: Fuzzification layer. It is a layer where the Membership Function (MF) of input is obtained. It is an adaptive layer whose output is given by:

$$O_i^1 = \mu_{Ai}(e) \text{ where i=1, 2,..m} \tag{3.98}$$

Where e is error (input), Ai is linguistic Variable and μ is membership function.

There are several types of membership functions. Among those, in this thesis, triangular-based MF is selected since it is popular and simpler to design than the others. It can be expressed as:

$$\mu_{Ai}(e) = trimf\,(e, ai, bi, ci) \tag{3.99}$$

$$\mu_{Ai}(e) = \max(\min(\frac{e-ai}{bi-ai}, \frac{ci-e}{ci-ai}), 0) \text{, i= 1,2,…m} \tag{3.100}$$

Where ai, bi and ci are premise or antecedent parameters.

Layer 2: Rule layer: It is a fixed layer whose output is the firing strength (weight) of the rule. It multiplies the incoming inputs and provide output for the next layer. However, in this case since only one input is used the output from this layer will be the same as the first layer. It can be represented as:

$$O_i^2 = \mu_{Ai}(e) \tag{3.101}$$

Layer 3: Normalization layer: It is also a fixed layer whose output is normalized firing strength (weight) of the rule obtained from layer 2. It is the ratio of the weight of each node to the total weight. It is given by:

$$O_i^3 = \overline{wi} = \frac{wi}{\sum_i wi} \text{, i=1,2,..m} \tag{3.102}$$

Layer 4: Defuzzification layer. It is adaptive layer which takes the normalized weight as an input and provides consequent parameter set. It can be obtained as:

$$O_i^4 = \overline{wi} * fi = \overline{wi}(ki * e + ri) \text{ ,i=1,2,…m} \tag{3.103}$$

Where ki and ri are consequent or output parameters.

Layer 5: Output layer. It is a fixed layer whose output is obtained by the summation of incoming signals. It can be expressed as follows:

$$O_i^5 = \sum_i \overline{wi} * fi = \frac{\sum_i wi * fi}{\sum_i wi} \text{ , i=1, 2, …m} \tag{3.104}$$

As previously stated, the layer 1 and 4 are adaptive layers whose value at each node is changed with the error so that the optimized relation between the input and output is obtained. This can be done by proper tuning of the premise and consequent parameters. Therefore, in order to archive this, in this thesis, hybrid algorism is employed for training purpose. It is a combination of Least Square Method (LSM) and Back Propagation (BP). The LSM is utilizes to determine the consequent parameters on the fourth layer. On the other hand, BP is used to reduce the error and to make the model more reliable. This is archived by propagating the error backward and tuning the premise parameters (Noureldeen & Hamdan, 2018).

3.12.3.1. ANFIS Design for Rotor Current and DC Link Voltage Control

In this thesis, ANFIS controller is employed to control the DC link voltage and rotor currents. There are some steps that should followed while designing this controller in MATLAB. First the training data (i.e., error and output) are generated from the PI controllers of the rotor currents as well as the DC link voltage and saved in the MATLAB's workspace. These datas are arranged in the form matrix in which the first column indicates the error and the last indicates the output. Then these data are loaded into ANFIS GUI of MATLAB tool box. Then the training is started after the selection of the type of MF for the inputs, the learning algorism and the number of iterations. In this thesis, triangular MF and hybrid algorism are selected. Triangular MF is selected for the inputs due to its simplicity and computational efficiency. On the other hand, the hybrid algorism, which is the combination of the Least square method (LSM) and Back propagation (BP), is used to obtain the consequent and premise parameters. Once the training is completed, the defuzzification process takes place and then fis file is extracted. Finally, this fis file is inserted and simulated in the MATLAB Simulink to obtain the required results (i.e., rotor currents and DC link voltage). Based on the parameters in Appendix C, the optimized architecture of the ANFIS and the obtained MF of premise parameter (i.e., error) ae shown in figures 3.19 and 3.20, respectively.

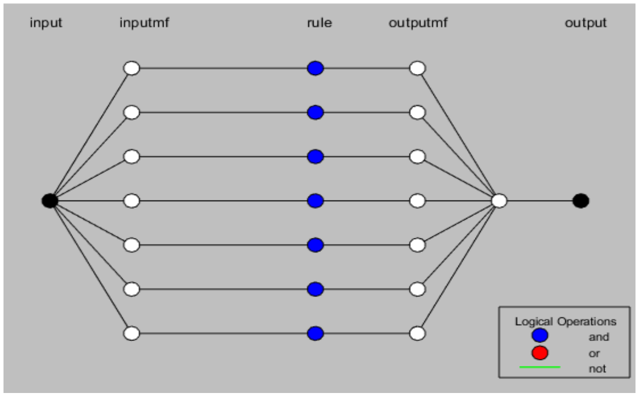

Figure 3.19: Optimized ANFIS Structure

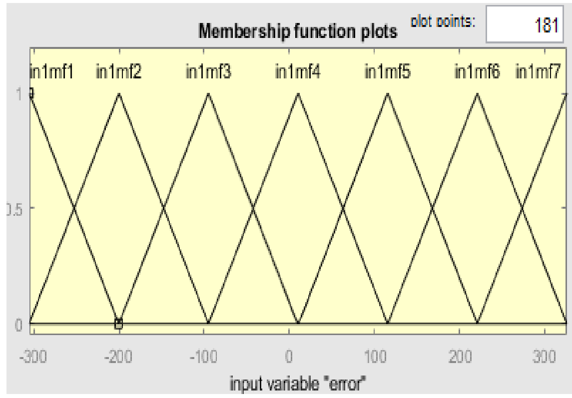

Figure 3.20: MF of error

CHAPTER FOUR

4. RESULTS AND DISCUSSIONS

4.1. Introduction

This chapter discusses the operation of a DFIG-based WECS under both normal and fault conditions. Additionally, a crowbar and an Adaptive Neuro Fuzzy Inference System (ANFIS) controller are utilized to analyze the performance of the system during a fault condition and also to enhance the system's LVRT capability. The parameters provided in Appendix A served as the basis for the model, which was created using MATLAB/Simulink 2021a.

4.2. MATLAB Simulink Model Description

In this section, the model of DFIG-based WECS is developed using MATLAB/Simulink 2021a as illustrated in Figure 4.1. WT, generator, converters, DC link, and grid are the main components that are used while modeling this system. A DFIG with a power rating of 1.5 MW is employed. This generator was selected mainly due to its operation in a wide range of wind speeds. It also requires converters of reduced size, which makes it more cost-effective than the others. It has a stator that is directly coupled to the grid and a rotor that is connected to the grid via back-to-back converters called a RSC and a GSC. A vector control technique is applied to help the converters successfully achieve their goals. Furthermore, crowbar protection technique and an Adaptive Neuro Fuzzy Inference System (ANFIS) controller are integrated with the system to improve the Low Voltage Ride Through (LVRT) capacity of the system as per the grid code requirement.

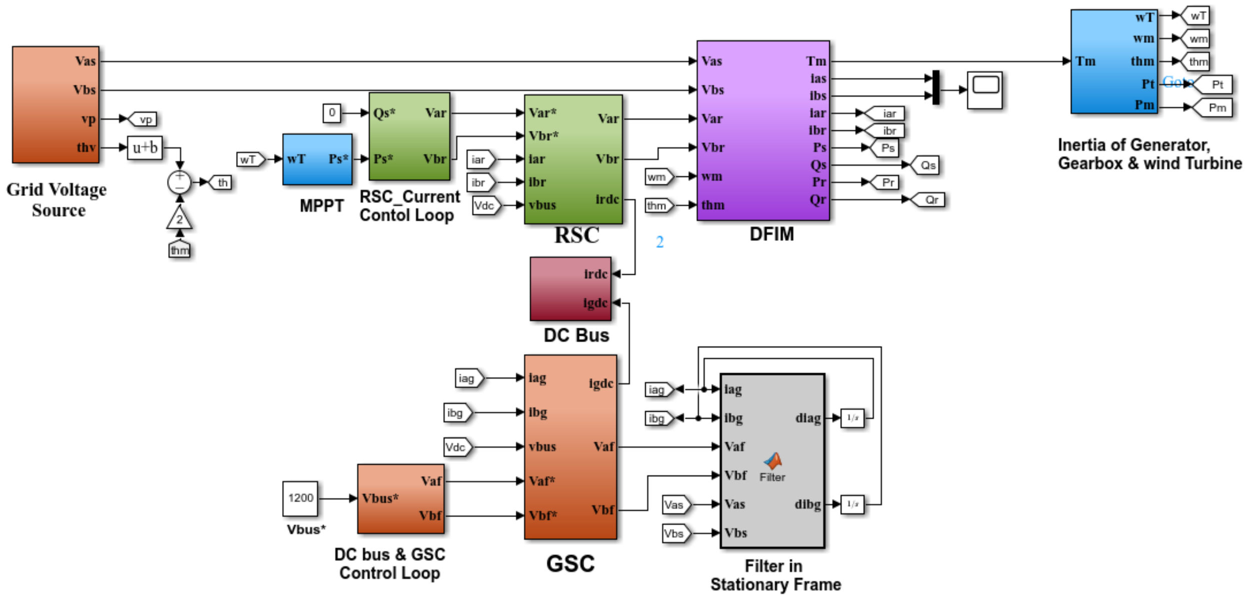

Figure 4.1: Simulink Model of DFIG-based WECS with its Control System

4.2.1. Rotor Side Converter Control Simulink Model

The RSC control model is shown in Figure 4.2. As previously stated, RSC is responsible for independent regulation of both active and reactive power. To reduce control complexity, three phase components are converted in to two phase. As a result, voltages and currents are converted to a dq frame of reference. Maximum Power Point Tracking (MPPT) is used to obtain the maximum power and also provides the reference for the stator active power (Ps*), whereas stator reactive power (Qs*) takes zero as its reference value. On the other hand, the Park transformation is employed to determine the actual direct and quadrature axis rotor currents (idr and iqr), whereas equation (3.66) is employed to determine their reference values (idr_ref and iqr_ref). Then the actual and reference values of these currents are compared and the error is sent as an input to the PI controller, whose output is rotor reference voltages (Vdr* and Vqr*). The Inverse Park transformation is used to obtain the alpha-beta component from these voltages (Vdr and Vqr) which is then converted to three phase voltage using inverse Clark transformation. Finally, the converter output voltage is obtained using Vdc and RSC's switching signals. On the other hand, the rotor current obtained from the generator's rotor is converted into three phases in the RSC to obtain the direct current across the rotor terminal (i_{r_dc}) as given in the equation (3.41). An angle (th) is an angle used for park's transformation.

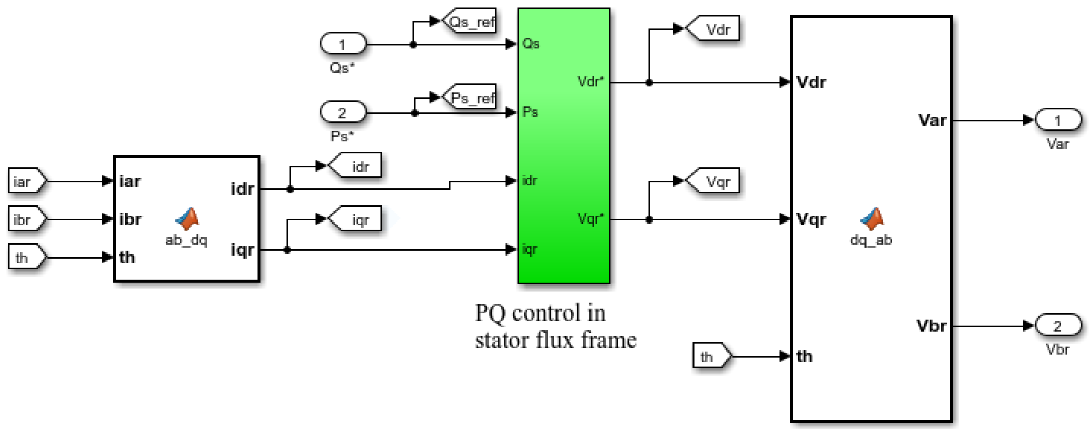

Figure 4.2: Rotor Side Converter Control Simulink Model

4.2.2. Grid Side Converter Control Simulink Model

The primary objective of GSC is to keep the DC link voltage constant. The controller starts its operation by comparing the actual DC link voltage (Vdc) with its reference value (Vdc_ref), and the error is sent as an input for the PI controller, which provides the reference value for the grid active power (Pg*) as shown in Figure 4.3. Similar to the RSC, zero is taken as the reference value for the grid reactive power (Qg*), and Park's transformation is also employed to determine the actual d and q components of grid currents (idg and iqg). On the other hand, equation (3.69) is used to obtain the reference values of these currents (idg_ref and iqg_ref). Then the actual and reference values of these currents are compared, and the error is again sent as an input to the PI controller, whose output is the reference voltages of the converter (Vdf* and Vqf*). The Inverse Park transformation is used to obtain the alpha-beta component from these voltages (Vaf and Vbf) which is then converted to three phase voltage using inverse Clark transformation. Finally, the converter output voltage is obtained using Vdc and GSC's switching signals as given as equation (3.59). On the other hand, the grid current is converted into three phases in the GSC to obtain the direct current across the grid terminal (i_{g_dc}) as given in the equation (3.50).

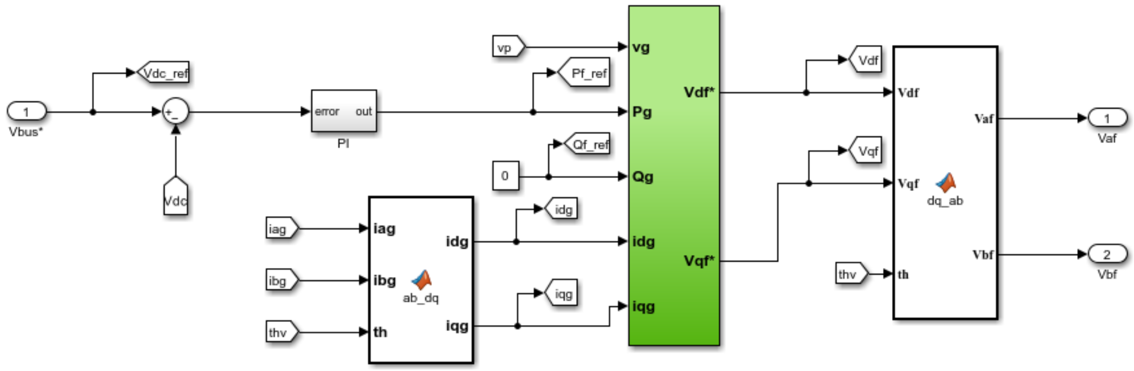

Figure 4.3: Grid Side Converter Control Simulink Model

4.3. Results

4.3.1. RSC and GSC Operation under Normal Condition

As previously stated, the main objective of RSC is to manage active and reactive power independently by adjusting the d and q-axis components of the rotor current. To accomplish this, both voltage and current must be converted to a dq frame of reference. In this case, the d-axis is aligned with the stator flux while the q-axis component has a value of zero. Furthermore, in steady state operation, the stator flux is proportional to the grid voltage, thereby the direct component of the stator voltage is zero where its quadrature component is constant. On the other hand, GSC is responsible for keeping the grid voltage constant by controlling the d-axis component of the grid current while its q-axis component is in charge of controlling the reactive power.

4.3.1.1 RSC under Normal Operation

Stator flux-oriented vector control is used to control the RSC of WECS. The simulation results are demonstrated as follows:

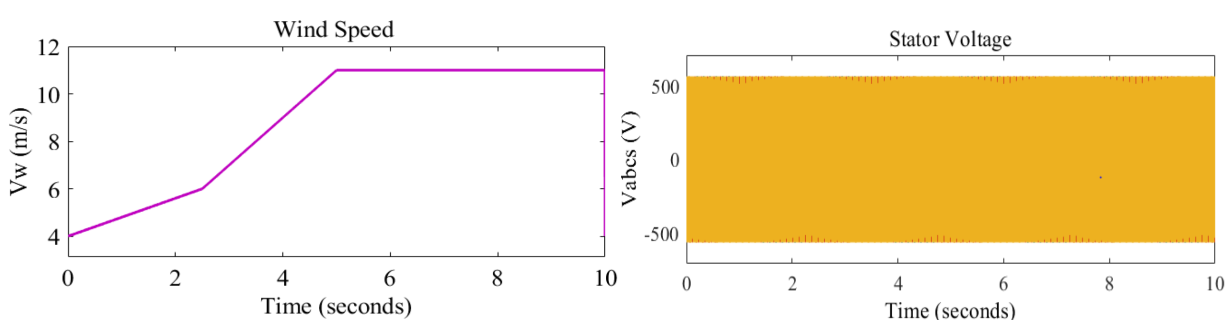

(a) Wind Speed (b) Stator Voltage

Figure 4.4: Wind Speed and Stator Voltage

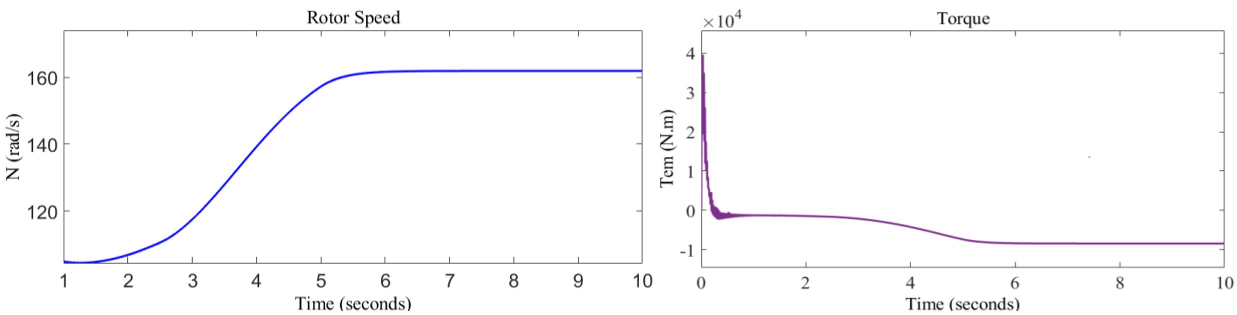

(a) Rotor Speed (b) Torque

Figure 4.5: Rotor Speed and Torque

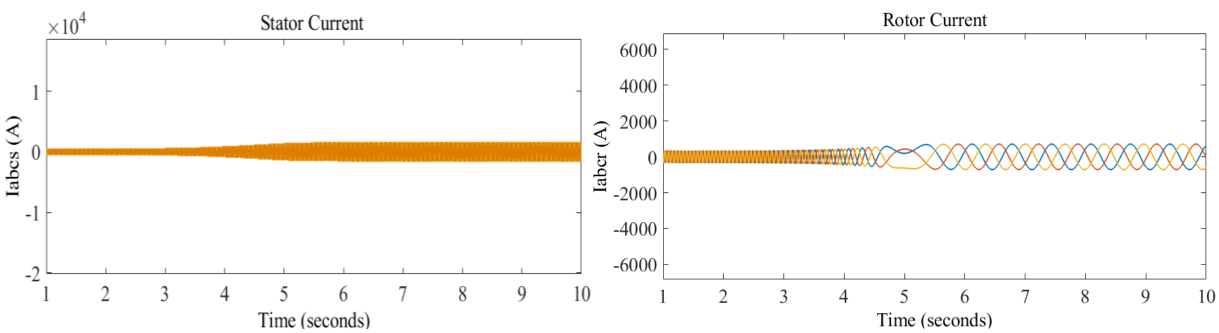

(a) Stator Current (b) Rotor Current

Figure 4.6: Stator and Rotor current

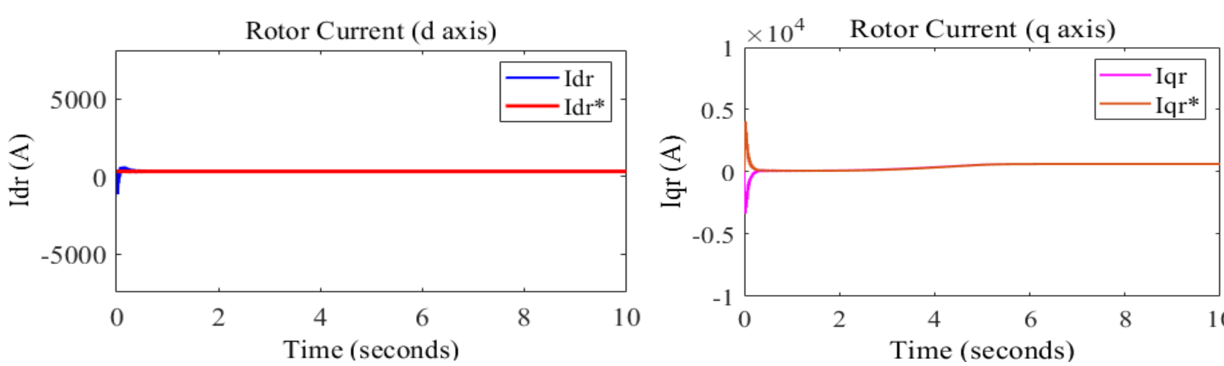

(a) Rotor Current (d axis) (b) Rotor Current (q axis)

Figure 4.7: Rotor Current in d and q axis

The wind speed that varies between 4 and 11 m/s is applied as shown in Figure 4.4(a). Figure 4.4(b) demonstrates the steady state operation of stator voltage. The rotor speed in normal operation is shown in Figure 4.5(a). As shown in Figure 4.5(b), the torque has a negative value which indicates the generator mode operation of a machine. The steady-state operation of the rotor and stator current, on the other hand, is depicted in Figure 4.6. The variation of stator and rotor currents after 5 seconds is due to the increase in rotor speed at the 5th second of simulation time. Figure 4.7 illustrates the steady state operation of d axis and q-axis components of rotor current. Since the system is operating under normal conditions, reactive power compensation isn't necessary (Qs = 0)

4.3.1.2 GSC under Normal Operation

A GVOVC technique is employed to control the GSC where the d-axis component is aligned with the grid voltage. As a result, the grid voltage's direct axis component is constant, whereas its quadrature axis component has a value of zero. The simulation results are demonstrated as follows:

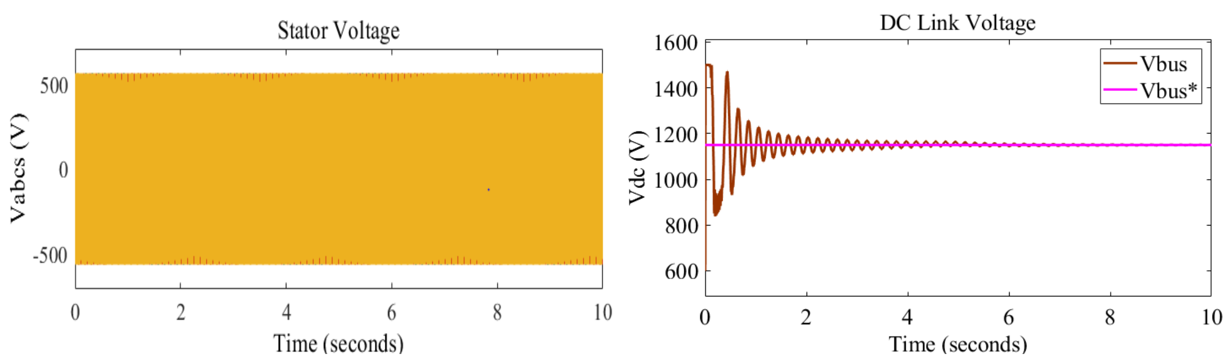

(a) Stator Voltage (b) DC Link Voltage

Figure 4.8: Stator and DC Link Voltage

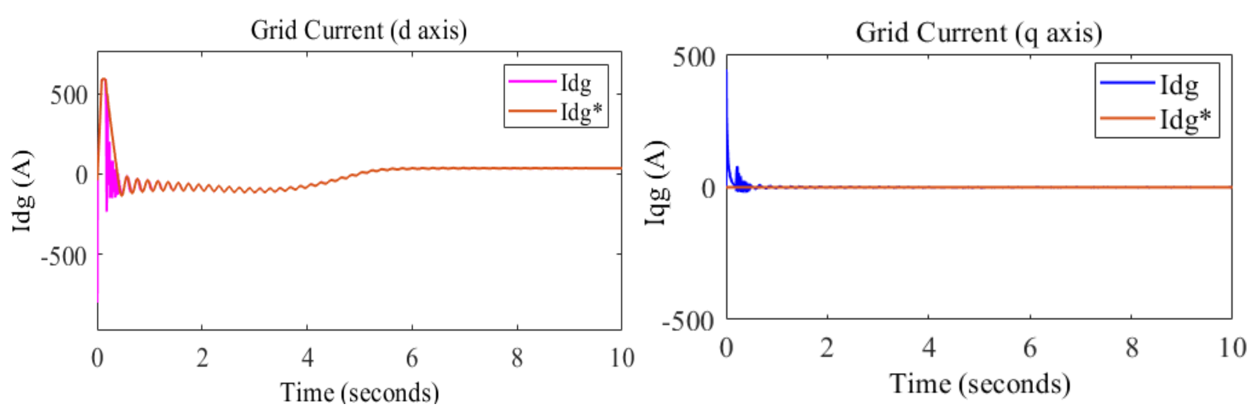

(a) Grid Current (d axis) (b) Grid Current (q axis)

Figure 4.9: Grid Current in d and q axis

The steady-state operation of stator voltage is shown in Figure 4.8(a). Figure 4.8(b) demonstrates that the DC link voltage is held at its nominal value which is 1150V with a few oscillations. The steady-state operation of grid current in the d and q axis is shown in Figure 4.9.

4.3.2. RSC and GSC Operation under Symmetrical Fault Condition

Faults on the grid-like symmetrical and asymmetrical cause reductions in grid voltage and also in stator and rotor flux. The reduction of voltage causes the induction of a high amount of current in stator terminals, which leads to a high rotor current due to magnetic coupling. This will prevent the GSC from providing power to the grid which causes overvoltage across the DC Link terminal which results in some serious damage to the capacitor at the DC Link terminal. Therefore, to avoid such kinds of problems, an appropriate protection technique or controlling strategies must be utilized. In this thesis, the effect of symmetrical fault on the steady-state performance of DFIG-based WECS is analyzed.

4.3.2.1. RSC Operation during Symmetrical Fault Condition

In this section, the performance of the system under symmetrical fault conditions without additional controlling mechanisms or protection techniques is analyzed. To analyze the system's performance, a voltage dip with a magnitude of 0.1pu is applied at the third second of the simulation time. The analysis is done according to the German grid code requirement since it is the most suitable one for practical applications. For a voltage sag of 0.1pu, the German GC requires the wind turbine to remain connected to the grid for at least 150 milliseconds and to maintain 90 percent of its nominal voltage within 1500 milliseconds after the fault has been cleared. The simulation results are demonstrated as follows:

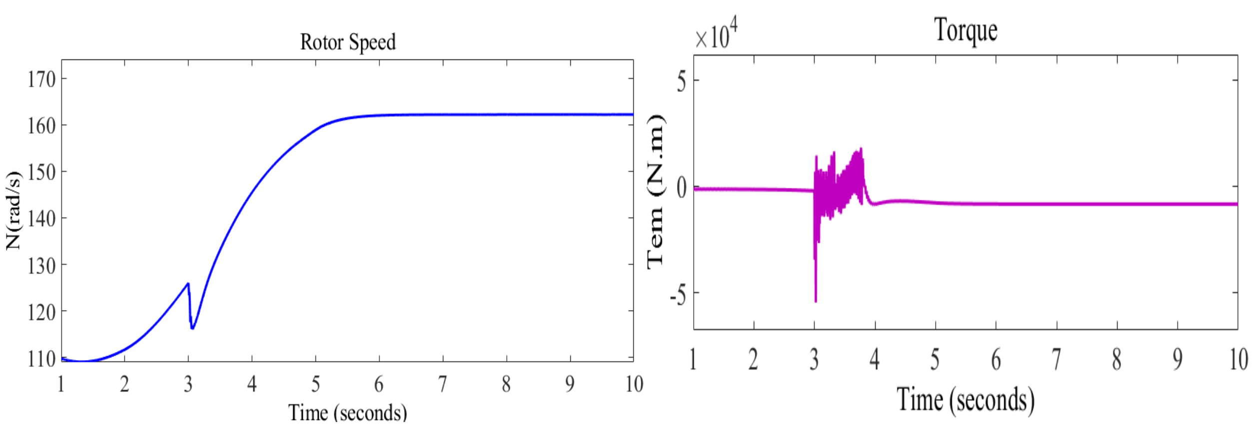

(a) Rotor Speed (b) Torque

Figure 4.10: Rotor Speed and Torque

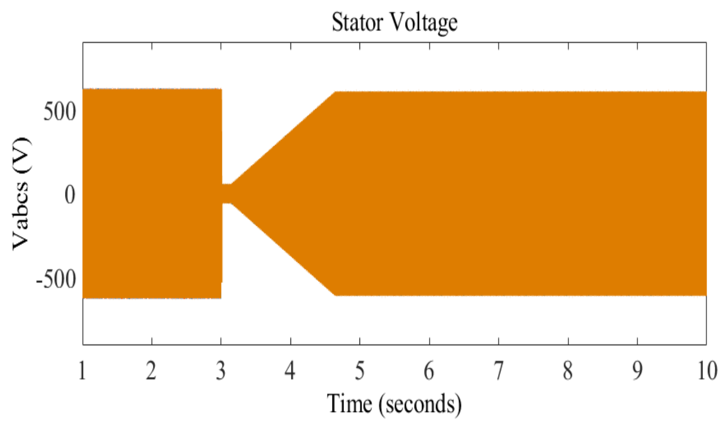

Figure 4.11: Stator Voltage

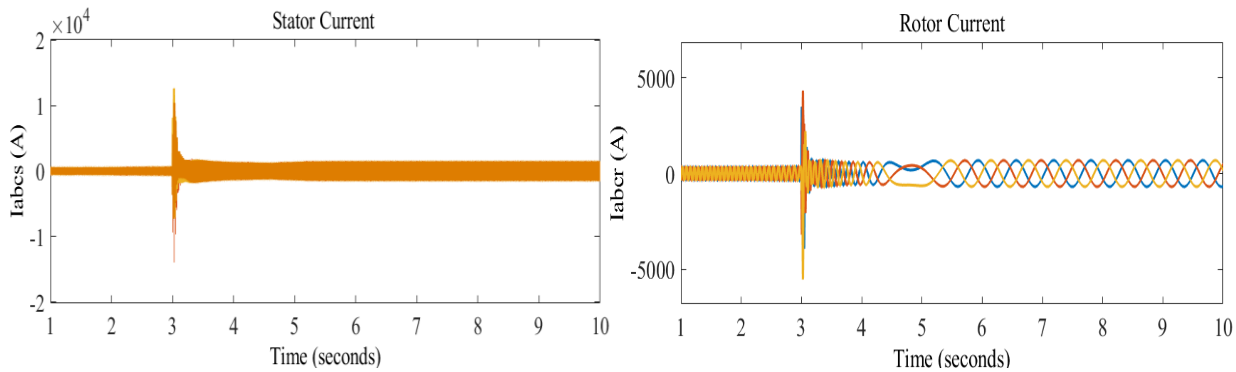

(a) Stator Current (b) Rotor Current

Figure 4.12: Stator and Rotor Current

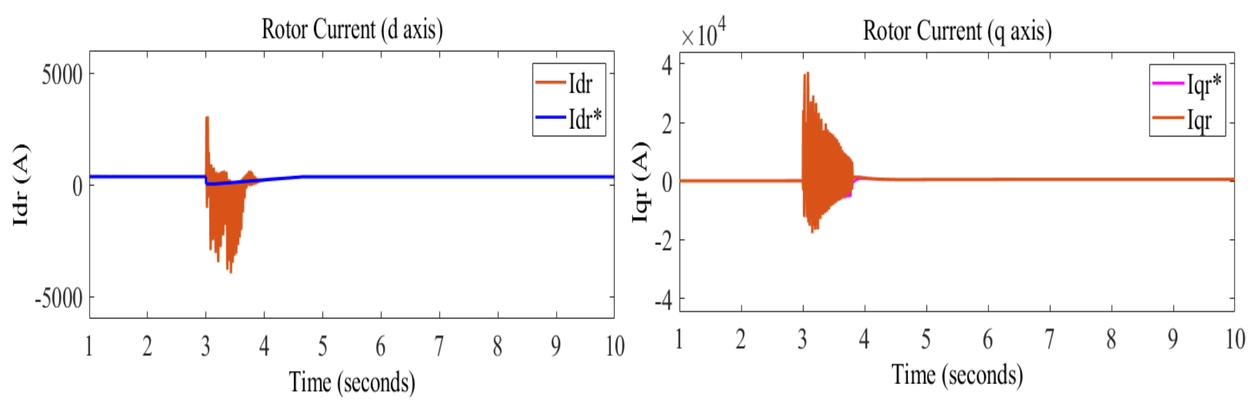

(a) Rotor Current (d axis) (b) Rotor Current (d axis)

Figure 4.13: Rotor Current in d and q axis

Figures 4.10 indicate the effect of the fault on the rotor speed and torque. The stator voltage drops 90% of its normal value at the 3rd sec and continues to operate at this voltage up to 3.15 sec, as shown in Figure 4.11. When the fault is removed from the system, it begins to retain its nominal value. Then it will return to its steady state operation after 1500 seconds. The impact of a grid fault on the stator and rotor current is illustrated in Figure 4.12. As shown in these Figures, both the stator and rotor currents are at their steady state operation during the pre-fault period, whereas the occurrence of voltage dip across the grid terminal causes the induction of high amount voltage across the rotor terminals. However, both return to their steady state operation after the complete clearance of the fault. Similarly, the occurrence of fault also causes the rise in current in the d and q-axis components of rotor. However, Finally, Figure 4.13 depicts during a grid fault condition. And similar to stator and rotor currents, these currents regained their nominal values after the fault is completely cleared from the system.

4.3.2.2. GSC Operation during Symmetrical Fault Condition

Similar to that of RSC, the voltage dip with a magnitude of 0.1pu is applied from 3 to 3.15 seconds for 150ms. The simulation results are demonstrated as follows:

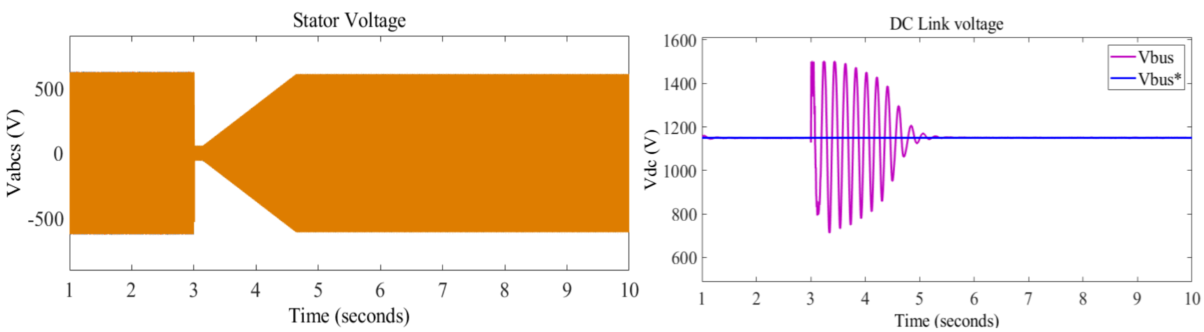

(a) Stator Voltage (b) DC Link Voltage

Figure 4.14: Stator and DC Link Voltage

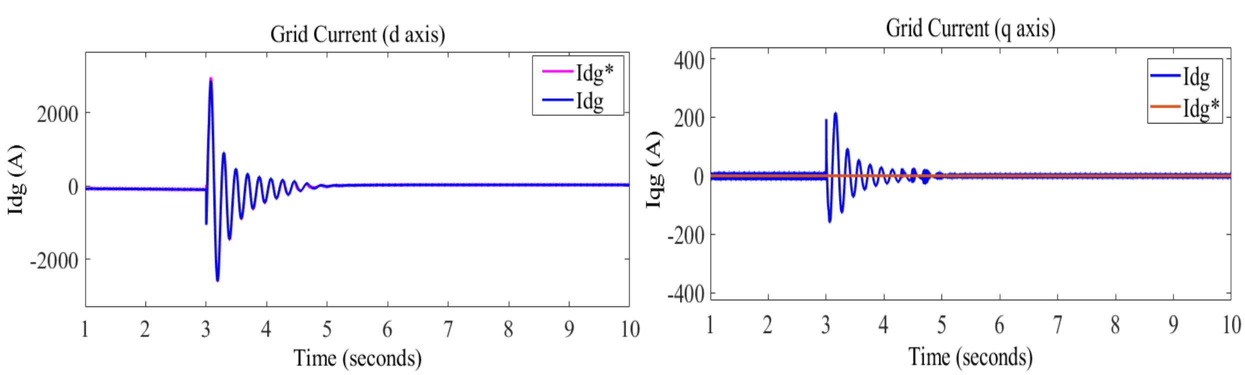

(a) Grid Current (d axis) (b) Grid Current (d axis)

Figure 4.15: Grid Current in d and q axis

As shown in Figure 4.14(a), when the fault occurs in the 3rd second of the simulation time, the stator voltage drops 90% of its nominal voltage and continuous operating with this voltage magnitude for 150ms. However, once the fault is removed it started regaining its nominal value. And finally, after 1500ms of the fault occurrence, it returns to its steady state operation as required by the German Grid Code. Furthermore, as mentioned in the previous section, when a fault occurs, the GSC loses control over the DC link voltage and it is also unable to transfer power to the grid. This led to the concentration of power at the DC link terminal charging the DC link’s capacitor which subsequently causes overvoltage. The rise of DC link voltage during the fault period is shown in Figure 4.14(b). However, it will start regaining its nominal value once the fault is completely cleared. On the other hand, the impact of these faults on the d and q axes of grid current is illustrated in Figure 4.15. Similar to that of the DC link voltage, these currents also start to follow their reference value after the complete clearance of the fault.

4.3.3. RSC and GSC Operation under Fault Condition with Crowbar

As stated earlier, the voltage dip on the grid side due to different grid faults causes an increase in rotor current, which prevents the transfer of power to the grid. However, since DFIG-based WECS uses converters with reduced size, it has limited overcurrent handling capability. Therefore, the occurrence of a high amount of current across the rotor terminals will cause some serious damage to the RSC. So, to avoid this problem, some protection mechanisms or appropriate control techniques should be used.

In this section, a crowbar protection mechanism is used. A crowbar is a group of resistance that is connected between the rotor winding and RSC. When a fault occurs, it creates a low resistance path to the fault current by disconnecting the RSC temporarily. Therefore, the machine stays secure. In order to archive these the value of the crowbar resistance should be high enough (i.e., greater than the rotor resistance) to handle the high amount of current that appears across the rotor terminal during the fault period.

4.3.3.1. RSC Operation during Symmetrical Fault Condition with Crowbar

In this section, the performance of the RSC during the occurrence of a symmetrical fault is analyzed. The severity of the voltage dip determines the fault's impact. This is due to the fact that the fault current also increases in proportion to the voltage dip. In this study, a voltage dip of 0.1pu magnitude is applied for 3 seconds to evaluate the RSC's performance. The simulation results are demonstrated as follows:

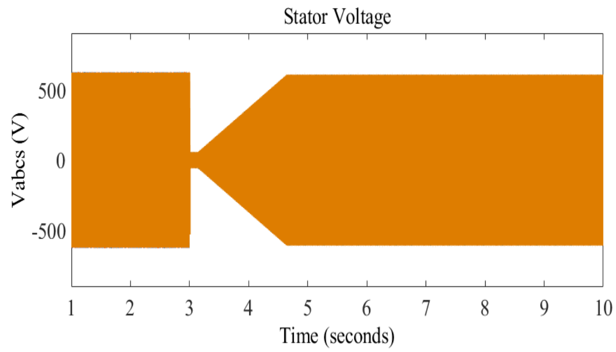

Figure 4.16: Stator Voltage

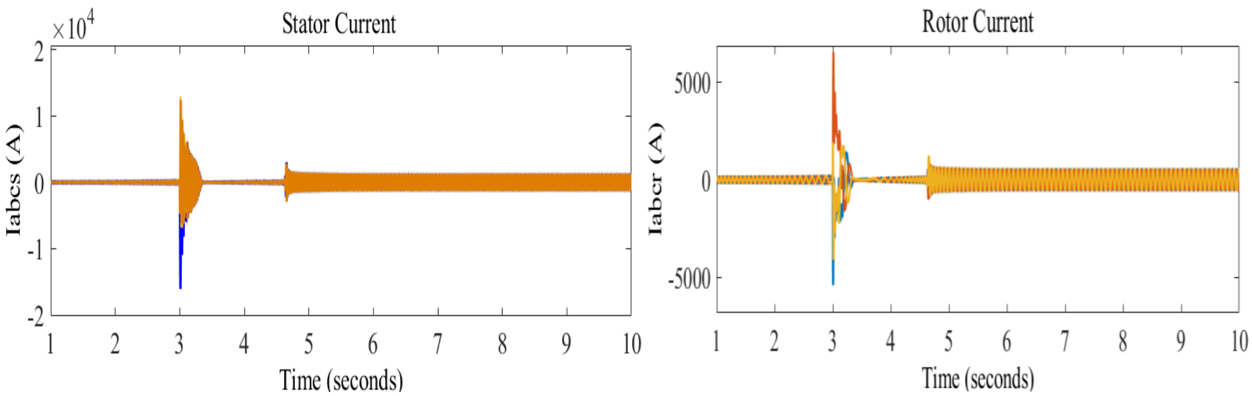

(a) Stator Current (b) Rotor Current

Figure 4.17: Stator and Rotor Current

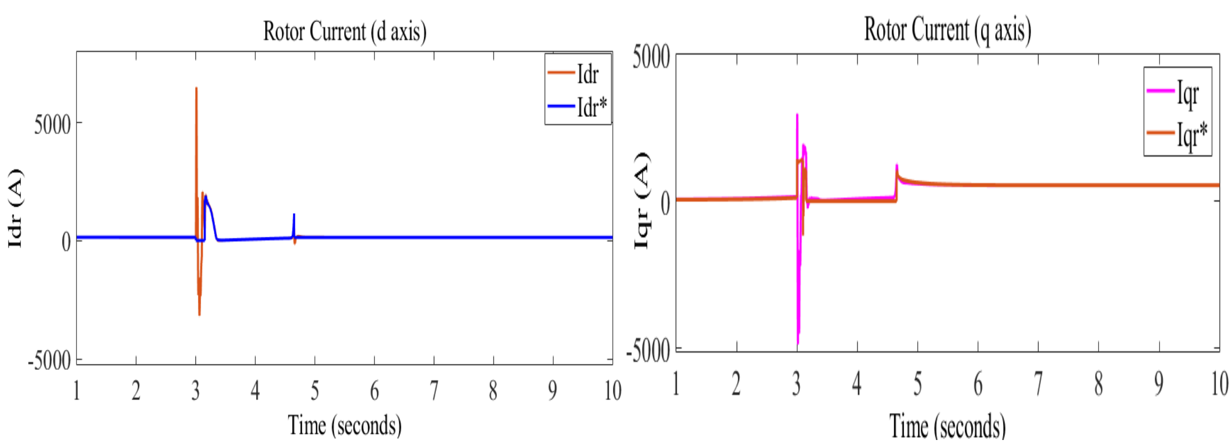

(a) Rotor Current (d axis) (b) Rotor Current (q axis)

Figure 4.18: Rotor Current in d and q axis

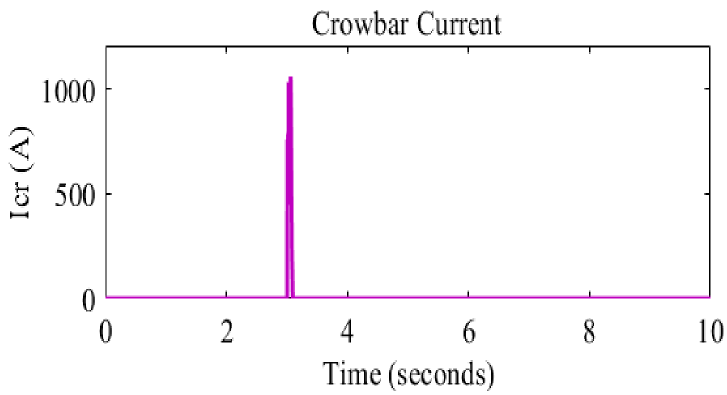

Figure 4.19: Crowbar Current

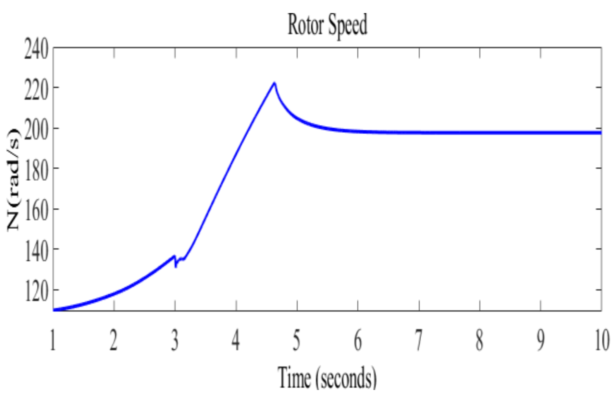

(a) Rotor Speed

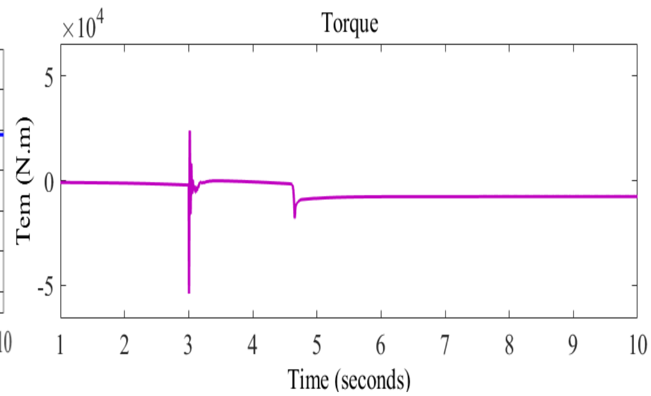

(b) Torque

Figure 4.20: Rotor Speed and Torque

Figure 4.16 shows that the stator voltage was operating at its steady state before the fault, but its magnitude was reduced when the fault occurred, and it continued its operation with this magnitude for the subsequent 150ms. However, it returns to its normal operation 1500ms after the occurrence of the fault, as required by the German Grid Code. This is archived because of the crowbar since it comes to operation by disabling RSC for 100ms after the occurrence of the dip and protecting it from high currents appearing around the rotor winding during the fault. After 100ms of the fault occurrence, the crowbar is disabled, and the RSC returns to its operational state, as shown in figure 4.19. The flow of a high amount of current across the stator, rotor, and crowbar terminal during the fault period is shown in Figures 4.17, and 4.19. However, once the fault has been completely cleared, all currents are restored to their pre-fault operation. Similarly, the occurrence of fault also causes the rise in current in the d and q-axis components of rotor. However, similar to stator and rotor currents, these currents regained their nominal values after the fault is completely cleared from the system as shown in figure 4.18. And finally, the effect of the fault on rotor speed and torque is shown in figure 4.20.

4.3.3.2. GSC Operation during Symmetrical Fault Condition with Crowbar

Similar to RSC, a voltage dip of 0.1pu magnitude is applied at the 3rd second to evaluate the performance of DFIG at GSC during balanced three-phase faults or symmetrical faults with the crowbar protection technique. The simulation results are demonstrated as follows:

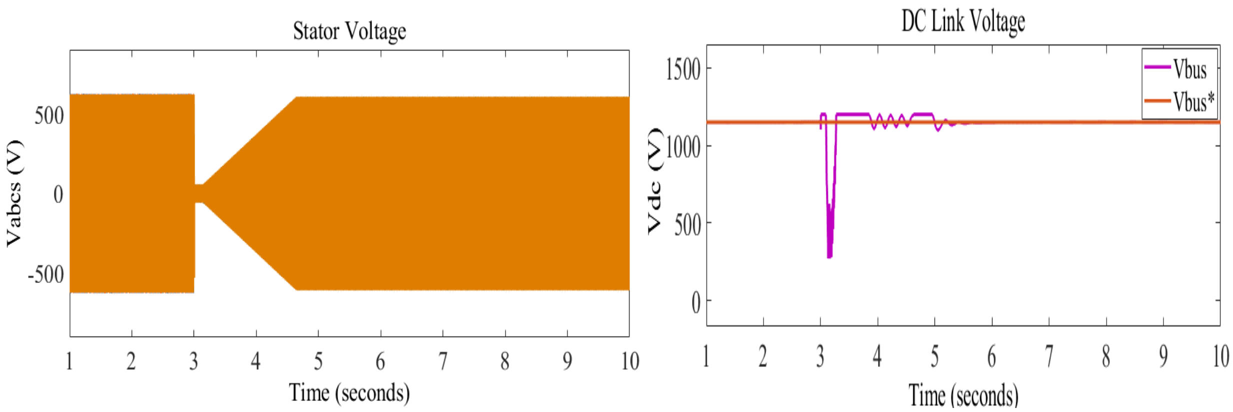

(a) Stator Voltage (b) DC Link Voltage

Figure 4.21: Stator and DC Link Voltage

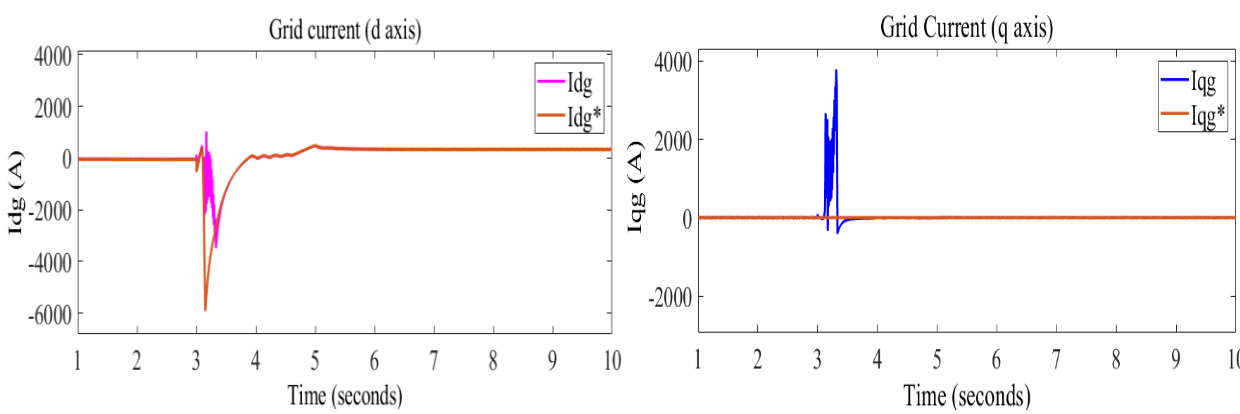

(a) Grid current (d axis) (b) Grid current (q axis)

Figure 4.22: Grid Current in d and q axis

Figure 4.21(a) demonstrates the stator voltage; whose value drops during the occurrence of a fault but starts regaining it once the fault is cleared. As previously stated, a voltage dip on the grid terminal will cause an overcurrent on the rotor winding. During this time, the crowbar will be triggered by decoupling the RSC from the rotor winding for protection. Due to the RSC's inability to supply the generated power to the grid, the voltage at the DC link terminal is decreased. However, once the fault is completely cleared, the DC link starts restoring its nominal voltage, as shown in figure 4.21(b). Similarly, the effect of this fault on the d and q-axis components of grid current is illustrated in figure 4.22.

4.3.4. RSC and GSC Operation under Fault Condition with ANFIS

As stated in the previous section, when symmetrical faults occur, the voltage across the grid terminals will decrease. This will result in the rise of rotor current to its peak value on the RSC terminals. But it is known that the controlling capacity of the RSC is limited since the DFIG-based WECS employs a power converter with reduced size. This phenomenon will get worse as the voltage dip increases, which consequently leads to the induction of an enormous amount of current across the RSC. Due to this, the controlling capacity of the RSC is completely lost. Not only that, but the occurrence of this fault also prevents the GSC from transferring power to the grid which led to the concentration of a high amount of power at the DC link terminal causing overvoltage. Therefore, to prevent the occurrence of such problems, the proper protection mechanism or controlling technique must be utilized.

Crowbars are the most popular protective devices used to both protect the system from excessive currents that appear across the rotor terminal during a fault and also to enhance the LVRT capacity of the system. However, employing this device has its own drawbacks. The main disadvantage of using a crowbar is that it converts a machine into a conventional squirrel-cage induction generator (SCIG), which absorbs a significant amount of reactive power from the grid and slows down the grid voltage recovery process. Therefore, to avoid this issue in this thesis, ANFIS is used to regulate the rotor current and DC Link voltage within their respective ranges without utilizing any additional devices. It also improves system stability since it performs its operation without disconnecting the RSC. Furthermore, it serves as a protection mechanism in the event of a grid terminal's fault in comparison to a PI controller and also satisfies GC requirements. In order to archive this first it generates data using the error and output parameters of PI controller (i.e., error and output) and by using the hybrid algorism it minimizes the error so that the actual values always follow their reference value. In such way it allows the system to return to its normal operation within a short period of time.

4.3.4.1. RSC Operation during Symmetrical Fault Condition with ANFIS

As previously mentioned, when a three-phase symmetrical fault occurs in the system, the RSC will lose its controlling capability due to the rise of rotor current beyond the limit. In other words, the rotor currents (i.e., both idr and iqr) deviate from their nominal values during this fault period. The performance of DFIG at RSC during balanced three-phase faults or symmetrical faults with an Adaptive Neuro Fuzzy Inference System (ANFIS) controller is shown in the following figures. Similarly, the voltage dip with a magnitude of 0.1pu occurred from 3 to 3.15 seconds for 150ms, and it restored 90% of its nominal value within 1500ms after the clearance of the fault as required by the German Grid Code. The simulation results are demonstrated as follows:

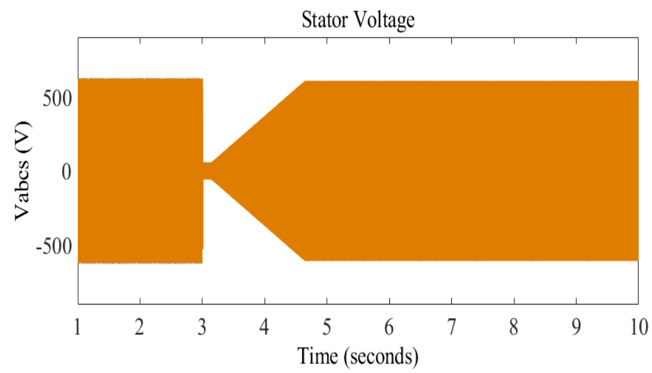

Figure 4.23: Stator Voltage

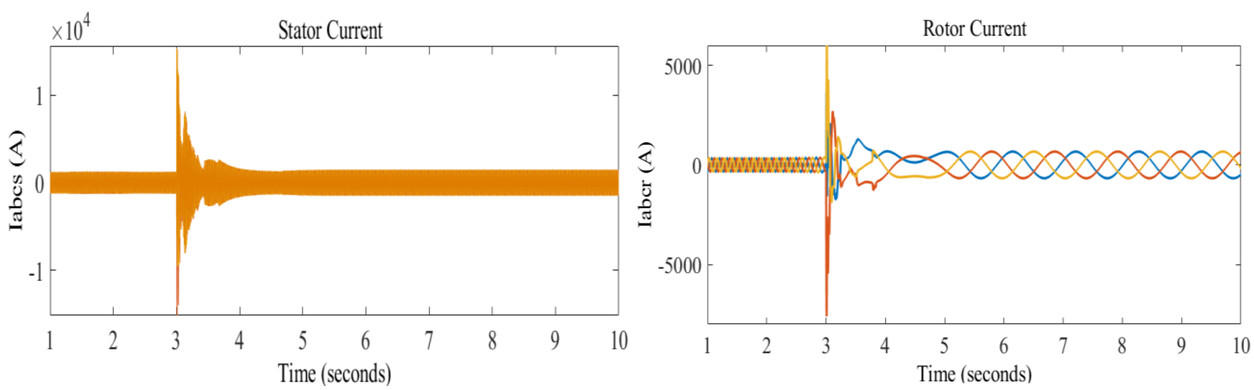

(a) Stator Current (b) Rotor Current

Figure 4.24: Stator and Rotor Current

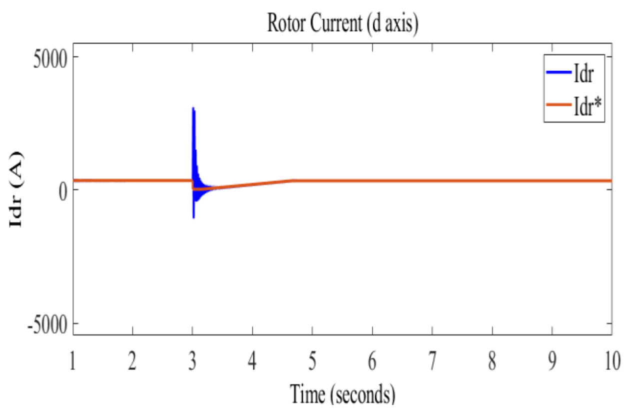

(a) Rotor current (d axis)

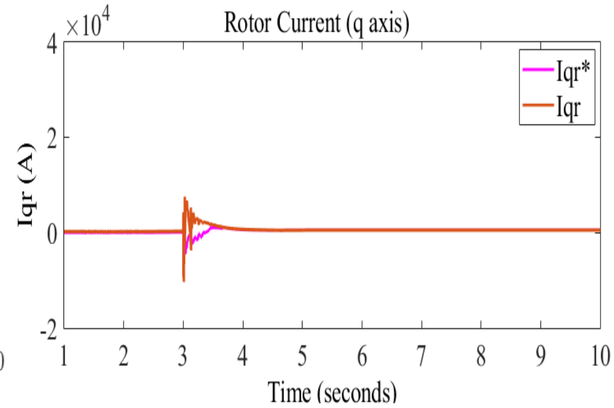

(b) Rotor current (q axis)

Figure 4.25: Rotor Current in d and q axis

When a symmetrical fault occurred at a grid terminal, the stator voltage dropped 90% of its nominal value and continued to operate at this voltage magnitude, as shown in Figure 4.23. However, after 3.15 seconds, it started retaining its nominal value. And finally, after the complete clearance of the fault i.e, 3.65 seconds, it is returned to its steady state operation again. As shown in Figure 4.24, currents in both the stator and rotor terminals were in their normal operation during the pre-fault period. However, when a fault occurred at the grid terminal, the currents across both terminals raised to pick values. And finally, these currents are regained their nominal values when the fault is completely cleared from the system. The rise in the d and q-axis components of rotor current during the fault period is shown in Figure 4.25. And similar to that of rotor and stator current, these currents are returned to their normal operation once the fault is completely removed from the system.

4.3.4.2. GSC Operation during Symmetrical Fault Condition with ANFIS

Similar to that of RSC, GSC also loses its controlling capability when a fault occurs. In other words, during the fault period, the DC Link voltage deviates from its nominal values. The following figures demonstrate the performance of the DFIG at GSC under balanced three-phase or symmetrical fault with an Adaptive Neuro Fuzzy Inference System (ANFIS) controlling strategy. The voltage drops occurred for 150ms between 3 and 3.15 seconds and must be restored within 1500ms after the fault clearance, as required by the German Grid Code. The simulation results are demonstrated as follows:

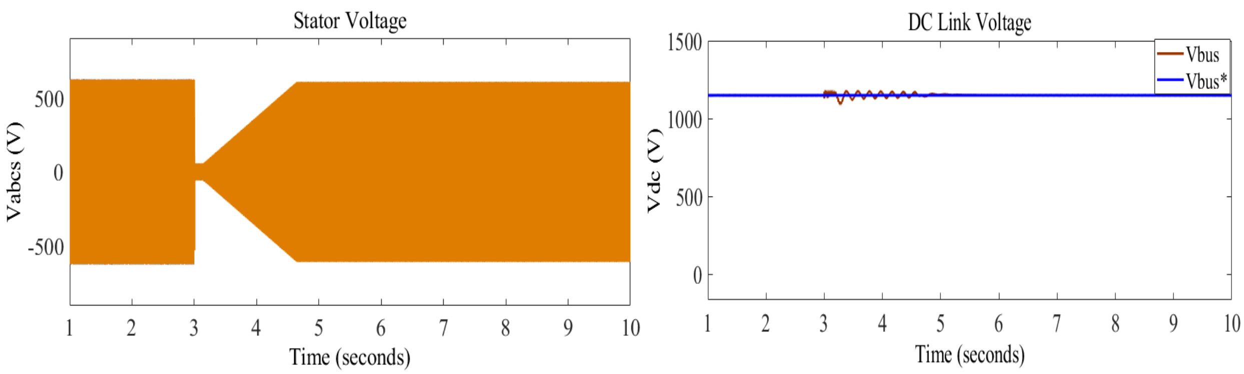

(a) Stator Voltage (b) DC Link Voltage

Figure 4.26: Stator and DC Link Voltage

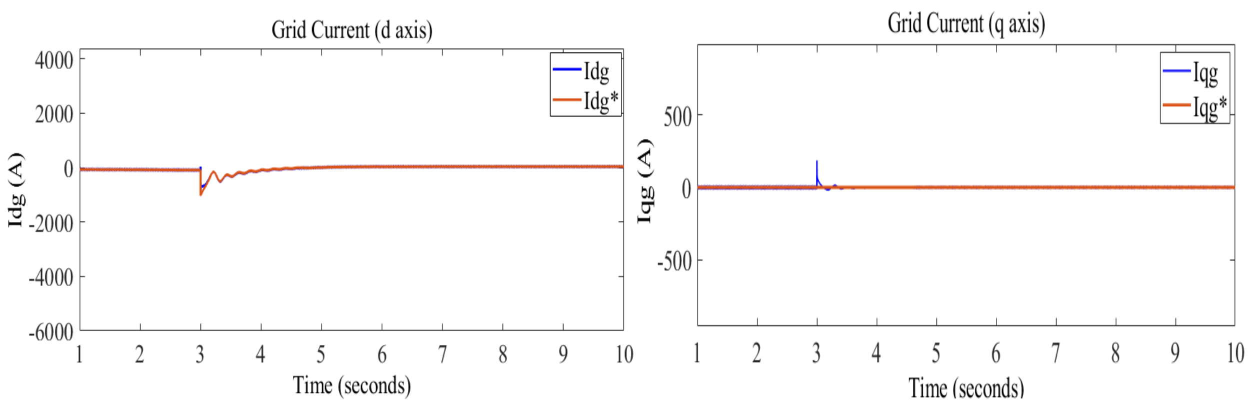

(a) Grid Current (d axis) (b) Grid Current (q axis)

Figure 4.27: Grid Current in d and q axis

As shown in Figure 4.26(a), during the pre-fault period, the stator voltage was at its steady state operation. However, when a fault occurs at 3 seconds, its magnitude dropped and operates with this magnitude for 150ms. And, once the fault is cleared, it will retain its nominal voltage again. Figure 4.26(b) shows that the DC link voltage is maintained at a steady state value with a few oscillations. And finally, the effect of this fault on the d and q-axis components of the grid's current is illustrated in Figure 4.27.

4.4. Comparative Analysis

In this section, the performance of the system while employing the PI, crowbar, and ANFIS is compared and the conclusion is drawn based on this analysis.

4.4.1. Comparison in Rotor Side Converter

In this section, the parameters at the RSC are compared when PI, crowbar, and ANFIS are employed in the system. Figure 4.28 illustrates different parameters in RSC. A distinct number is assigned to each figure to differentiate them from each other. The parameters with the PI controller are denoted by ‘1', the parameters with the crowbar protection system are denoted by ‘2', and the parameters with the ANFIS controller are denoted by ‘3'.

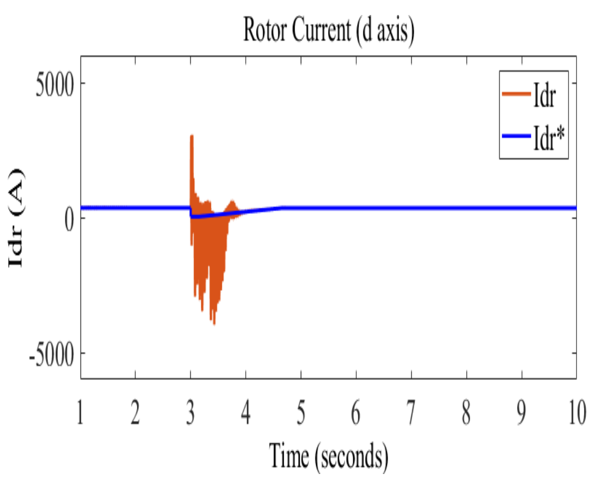

(a1)

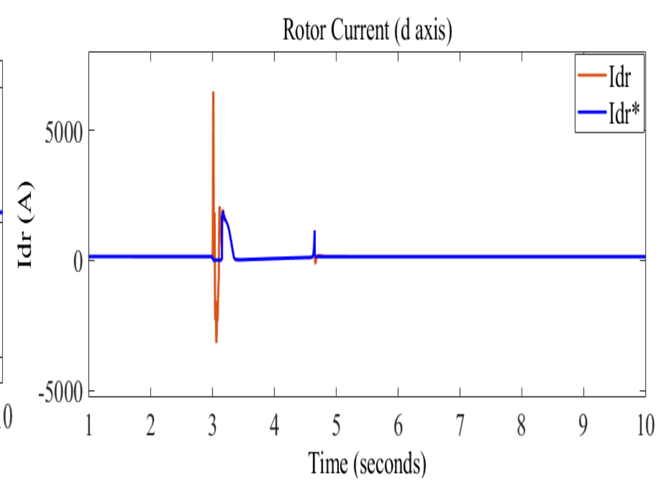

(a2)

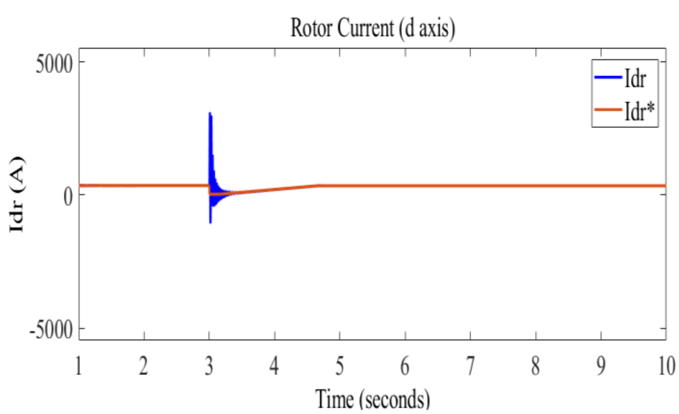

(a3)

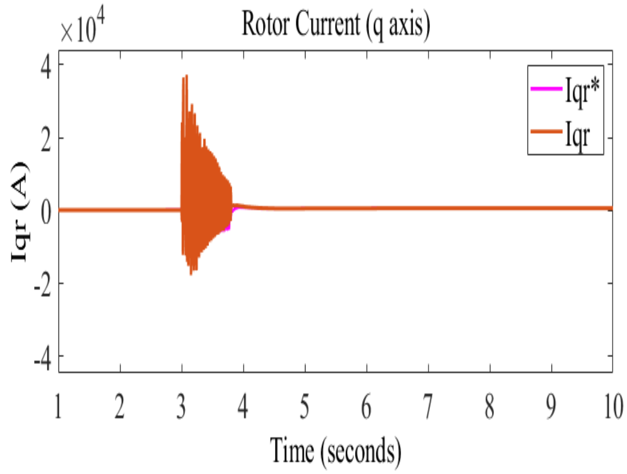

(b1)

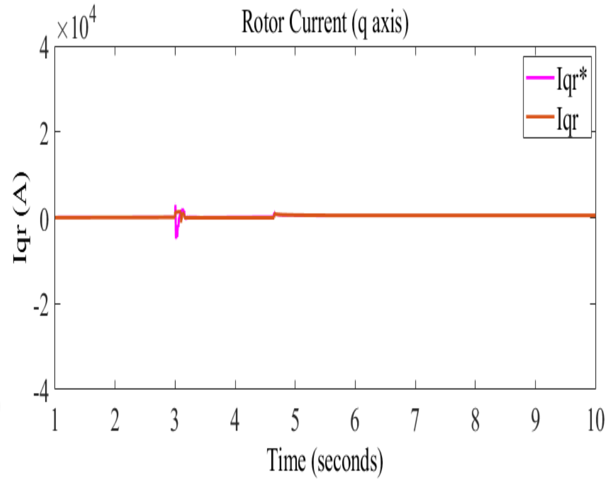

(b2)

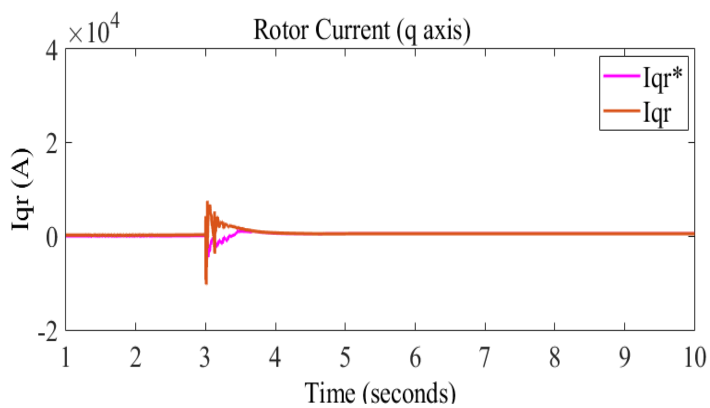

(b3)

Figure 4.28: Comparative Analysis in RSC

Figure 4.28(a1, a2, and a3) show that during the fault period, a high amount of current flows in the d axis of the rotor terminal in all cases (PI, crowbar, and ANFIS). However, the system with ANFIS retains its nominal value within a short period compared to the remaining two techniques. In addition, it is also able to suppress a high amount of current flowing in the rotor terminal during the occurrence of a fault. In addition, similar to the d axis rotor current, the rotor current in the q axis also regains its nominal value when the fault is completely cleared, as shown in Figure 4.28(b1, b2, and b3). In addition to this, it is also observed that the system with ANFIS regains its nominal value within a short period compared to the others.

4.4.2 Comparison in Grid Side Converter

In this section, the parameters at the GSC are compared when PI, crowbar, and ANFIS are employed in the system. Figure 4.29 illustrates different parameters in GSC.

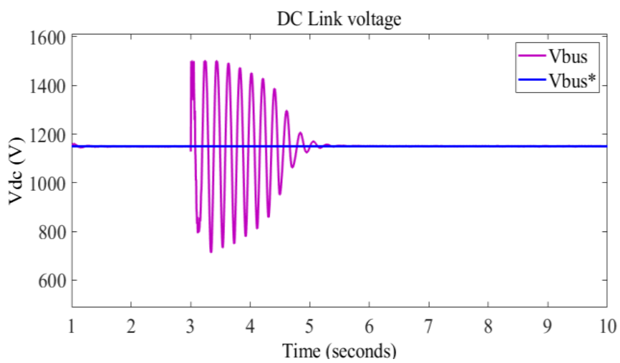

(a1)

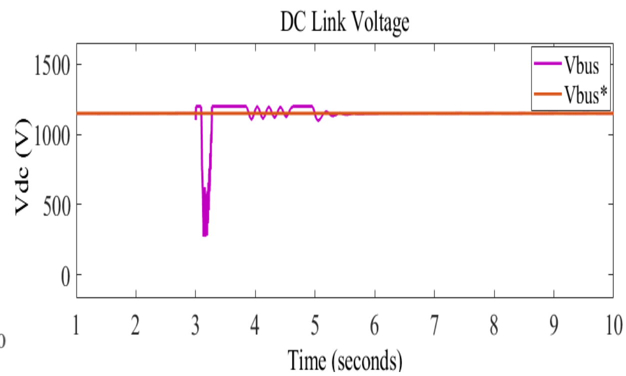

(a2)

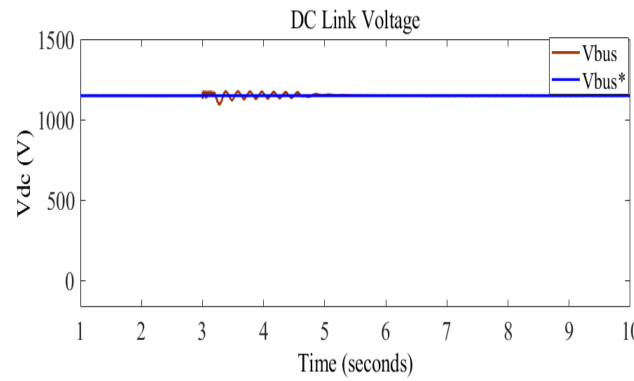

(a3)

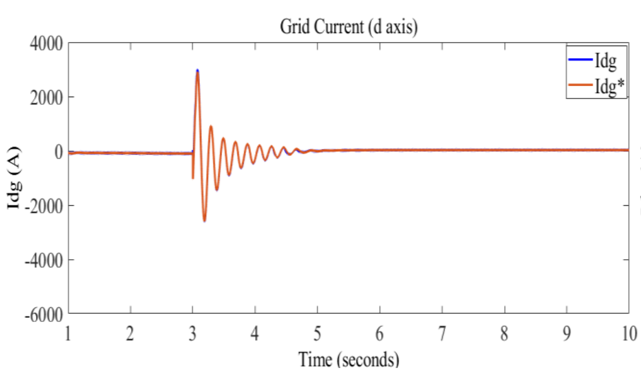

(b1)

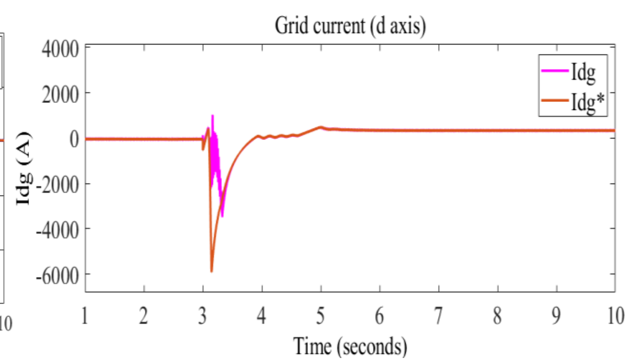

(b2)

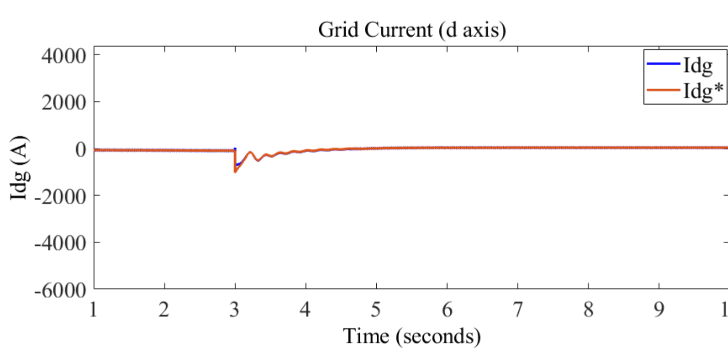

(b3)

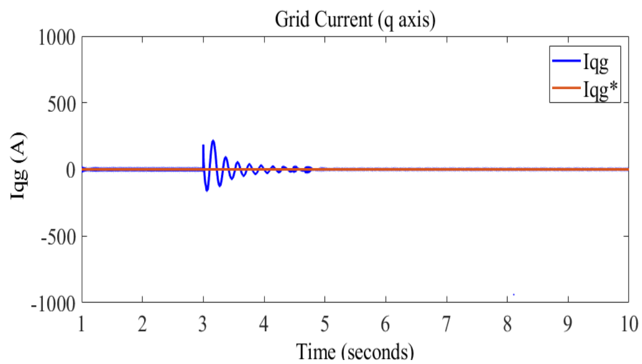

(c1)

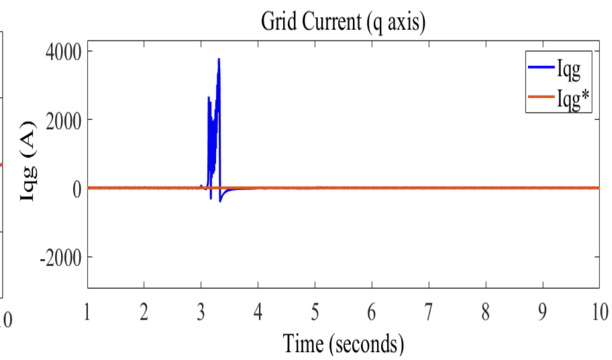

(c2)

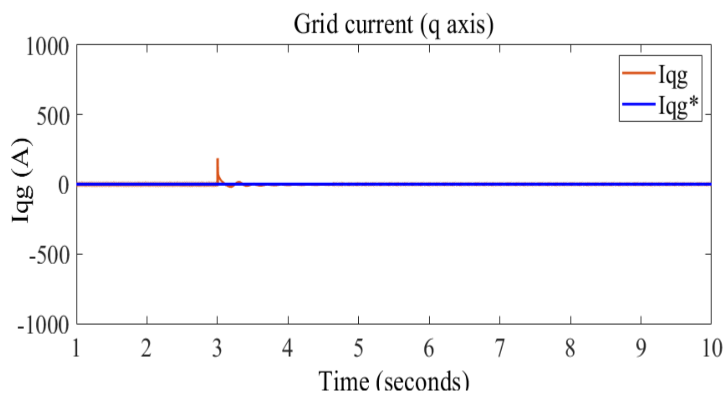

(c3)

Figure 4.29: Comparative Analysis in GSC

Figure 4.29(a1, a2, and a2) illustrates the DC link voltage obtained while employing PI, crowbar, and ANFIS in the system, respectively. As shown in Figure 4.29(a1), this voltage is raised to 1500V, which may cause some serious damage to the capacitor at the DC link terminal unless an appropriate protection technique or controlling strategy is employed. On the other hand, it is observed that there is a reduction in DC link voltage when the crowbar is employed in the system, as shown in Figure 4.29(a2). This is due to the fact that the crowbar prevents the RSC from supplying power to the grid when it comes to operation. Figure 4.29(a3) showed that the DC Link voltage is maintained at its nominal value (i.e., 1150V) but with few oscillations during the fault period. On the other hand, the effect of the fault on the d and q axis of grid current is shown in Figure 4.29(b1, b2, b3, c1, c2, and c3). It is observed that after the complete clearance of the fault, the system regained its nominal value in all cases. However, the system with ANFIS regained its nominal value within a short period of time compared to the others.

Table 5.1: Numerical Comparison of Parameters of RSC and GSC

Parameters	PI Controller	Crowbar	ANFIS Controller
Rotor current across the d and q axis	The rotor current in the d axis regains its nominal value at the 4th seconds.	The Rotor current in the d axis recovers after 4.65 seconds.	The settling time of Idr is 3.6 seconds.
	The rotor current in the q axis regains its nominal value at 3.91 seconds.	The rotor current in the q axis regains its nominal value at 4.65 seconds.	The settling time of Iqr is 3.57 seconds.
Grid current across the d and q axis	The d-axis component of the grid current recover after 4.5 seconds.	The d-axis component of the grid current recover at 3.8 seconds.	The settling time of Idg is 3.6 seconds.
	The grid current in the q axis regains its nominal value after 5 seconds.	The current in the q axis of the rotor terminal is settled down at 4 seconds.	The settling time of Iqg is 3.4 seconds.
DC-Link Voltage	It fluctuates between 1500V and 700V and regains its nominal value after 5.2 seconds.	It drops to 280V and regains its nominal value after 4.9 seconds with a few oscillations.	It is maintained nominal voltage with a few oscillations after 3.4 seconds.

As previously stated, the Low Voltage Ride Through (LVRT) capability of the system is the ability of the system to stay connected to the grid when a voltage dip occurs on the grid terminals and support it to retain its nominal value within a short period of time. And from the analysis given in the above sections, it can be concluded that the ANFIS controller performs better in protecting the system from damage and also in enhancing the LVRT capacity of the system than the remaining two techniques (i.e., PI and crowbar).

CHAPTER FIVE

5. CONCLUSION AND FUTURE WORKS

5.1. Conclusion

Double Fed Induction Generators (DFIGs) are the most commonly used generators for variable speed wind energy generation systems due to their great energy efficiency and controllability. Despite all of its advantages, it is incredibly vulnerable to grid faults like voltage dips. This is mainly due to the direct coupling of the generator's stator to the grid and also due to converters' limited capacity. This fault results in excessive current flowing through both the rotor and stator terminals. However, regardless of all of these issues, the current GC requires the system to remain connected to the grid almost all the time. Therefore, in order to archive this appropriate protection mechanism or controlling technique must be utilized. In this thesis, the performance of DFIG-based WECS under both normal and fault conditions is analyzed. Furthermore, two methods are used to enhance the system's LVRT capabilities and to meet the GC requirement. The first approach is the crowbar protection technique. During steady state operation, the rotor current flows through the RSC. However, when the voltage drop occur in the system, the crowbar isolates the RSC and creates a low-resistance path for the high rotor current caused by the fault. In such a way, this mechanism protects the RSC from being damaged. Nevertheless, blocking RSC has its own disadvantages, including a loss of power control that results in a severe transient happening after the fault which ultimately causes the system to be detached from the grid. Moreover, during the crowbar action, the generator is converted to a squirrel-cage induction generator, absorbing a significant amount of reactive power from the grid and extending the recovery time. Therefore, the second approach, an Adaptive Neuro Fuzzy Inference System (ANFIS) controller, is used to overcome problems associated with these issues. Unlike crowbar, this approach performs its operation by limiting the variance of steady-state stator and rotor currents, as well as the DC Link voltage, both during and after the fault, without disconnecting the RSC and also without employing an additional protective mechanism. In addition to this, according to the simulation results obtained the settling time of ANFIS for controlling the rotor currents in d and q axes (idr and iqr) and DC link voltage is 3.6 seconds, 3.57 seconds, and 3.4 seconds, respectively. On the other hand, the settling times of the PI controller for the controlling the rotor currents in d and q axis and the DC link voltage are 4 seconds, 3.91 seconds, and 45.2 seconds, respectively, while the crowbar protection technique's settling times are 4, 6, and 4.9 seconds, respectively Therefore, based on these results as well as based on the given justifications, it can be concluded that employing the latter approach is preferable to that of the former one.

5.2. Future Works

This study analyzes the influence of voltage dips on DFIG-based wind energy systems that are primarily caused by symmetrical faults, and it also employs a crowbar protection technique and an Adaptive Neuro Fuzzy Inference System (ANFIS) controller strategy to improve the system's Low Voltage Ride Through Capability (LVRT). As a result, future research should focus on:

- Analyzing DFIG’s performance under unsymmetrical faults;
- Investigating the DFIG’s performance considering other issues (i.e., harmonics) and also using other countries’ GC requirements;
- Comparative investigation by employing additional control strategies and better optimization techniques to enhance the controlling capacity.

Research Fund Acknowledgement

This research project is funded by Adama Science and Technology University under the grant number ASTU/SM-R/577/22, Adama, Ethiopia.

REFERENCES

Abad, A. M. and G. (2017). *Power Electronics and Electric Drives for Traction Applications*.

Abu-Rub, H., Malinowski, M., & Al-Haddad, K. (2014). Power Electronics for Renewable Energy Systems, Transportation and Industrial Applications. In *Power Electronics for Renewable Energy Systems, Transportation and Industrial Applications* (Vol. 9781118634). https://doi.org/10.1002/9781118755525

Adouni, A., Chariag, D., Diallo, D., Ben Hamed, M., & Sbita, L. (2016). FDI based on Artificial Neural Network for Low-Voltage-Ride-Through in DFIG-based Wind Turbine. *ISA Transactions*, *64*, 353–364. https://doi.org/10.1016/j.isatra.2016.05.009

Agha Kashkooli, M. R., Madani, S. M., & Lipo, T. A. (2020). Improved direct torque control for a DFIG under symmetrical voltage dip with transient flux damping. *IEEE Transactions on Industrial Electronics*, *67*(1), 28–37. https://doi.org/10.1109/TIE.2019.2893856

Akanto, J. M., & Hazari, R. (2021). *LVRT and Stability Enhancement of Grid-Tied Wind Farm Using DFIG-Based Wind Turbine*.

Benali, A., Khiat, M., Allaoui, T., & Denaï, M. (2018). Power Quality Improvement and Low Voltage Ride Through Capability in Hybrid Wind-PV Farms Grid-Connected Using Dynamic Voltage Restorer. *IEEE Access*, *6*. https://doi.org/10.1109/ACCESS.2018.2878493

Berhanu, M., Mekonnen, Y., Leidhold, R., Mamo, M., Muluneh, Z., & Sarwat, A. (2018a). Analysis of a Doubly Fed Induction Generator Through Modeling and Simulation. *2018 IEEE PES/IAS PowerAfrica*, *2018*, 652–657. https://doi.org/10.1109/PowerAfrica.2018.8521094

Berhanu, M., Mekonnen, Y., Leidhold, R., Mamo, M., Muluneh, Z., & Sarwat, A. (2018b). Analysis of a Doubly Fed Induction Generator Through Modeling and Simulation. *2018 IEEE PES/IAS PowerAfrica*, *2018*, 652–657. https://doi.org/10.1109/PowerAfrica.2018.8521094

Chen, J., Zhang, W., Chen, B., & Ma, Y. (2016). Improved vector control of brushless doubly fed induction generator under unbalanced grid conditions for offshore wind power generation. *IEEE Transactions on Energy*, 293–302. https://doi.org/10.1109/TEC.2015.2479859

Chen, L., Zhang, B., & Fan, X. (2020). Asymmetrical Fault Ride-Through Control Strategy for Rotor-Side Converter of DFIG. *IEEE Transactions on Energy Conversion*, *35*(2), 1046–1053.

https://doi.org/10.1109/TEC.2019.2963086

Controllers, F. P. I., & Al-zabin, O. (2019). Rotor Current Control Design for DFIG-based Wind Turbine Using Rotor Current Control Design for DFIG-based Wind Turbine Using PI , FLC and Fuzzy PI Controllers. *Thesis*, *9*, 4.

Dehong Xu, F. Blaabjerg, W. C. and N. Z. (2018). *Advanced Control of Double Fed Induction Generator for Wind Power System*.

E.A.D. Kumara K.G.R.M. Jayathilake, N. K. H. (2017). Review Paper- Overview of the Vertical Axis Wind Turbines. *International Journal of Scientific Research and Innovative Technology*, *4*(September), 56–67.

Echiheb, F., & Ghamrasni, M. (2022). *Robust Sliding-Backstepping Mode Control of a wind system based on the DFIG Generator based on the DFIG Generator*. 0–18.

Energy Statistics Course – Paris – 2nd of March 2015. (2015). *IEA.*

Falehi, A. D., & Rafiee, M. (2017). Enhancement of DFIG-Wind Turbine's LVRT capability using novel DVR based Odd-nary Cascaded Asymmetric Multi-Level Inverter. *Engineering Science International Journal*, *20*(3), 805–824. https://doi.org/10.1016/j.jestch.2017.05.004

Ganthia, B. P. (2020). *Shunt Connected FACTS Devices for LVRT Capability Enhancement in WECS*. *10*(3), 5819–5823.

GANTHIA, B. P., BARIK, S. K., & NAYAK, B. (2021). Low voltage ride through capability enhancement using series connected fact devices in wind energy conversion system. *Journal of Engineering Science and Technology*, *16*(1), 365–384.

Gholizadeh, M., Tohidi, S., Oraee, A., & Oraee, H. (2018). Appropriate crowbar protection for improvement of brushless DFIG LVRT during asymmetrical voltage dips. *International Journal of Electrical Energy Systems*, *95*, 1–10. https://doi.org/10.1016/j.ijepes.2017.07.018

Gomez, L. A. G., Grilo, A. P., Salles, M. B. C., & Filho, A. J. S. (2020). Combined control of DFIG-based wind turbine and battery energy storage system for frequency response in microgrids. *Energies*, *13*(4). https://doi.org/10.3390/en13040894

GONZALO ABAD. (2017). *Power Electronics and Electric Drives for Traction Applications*.

Hamdan, I., & Noureldeen, O. (2021). An Overview of Control Method with Various Crowbar

Techniques of Wind Turbines during Power System Faults. *SVU-International Journal of Engineering Applications*, *2*(1), 35–45. https://doi.org/10.21608/svusrc.2021.80571.1010

Haq, I. U., Khan, M. I., & Zeb, K. (2016). Siding Mode Control for PMSG based Wind Energy Conversion System connected to the grid. *2016 International Conference on Computing, Electronic and Electrical Engineering, ICE Cube 2016 - Proceedings*, 277–282. https://doi.org/10.1109/ICECUBE.2016.7495238

Ibrahim, R. K., & Watson, S. (2015). Wind turbine simulation model for the study of combined mechanical and electrical faults. *European Wind Energy Association Annual Conference and Exhibition 2015, EWEA 2015 - Scientific Proceedings*, *November*.

Ismail, M. M., & Bendary, A. F. (2016). Protection of DFIG wind turbine using fuzzy logic control. *Alexandria Engineering Journal*, *55*(2), 941–949. https://doi.org/10.1016/j.aej.2016.02.022

Jagadeeshwaran, K., & Kumar, K. R. (2017). Fuzzy sliding mode control strategy for grid side control of wind energy conversion system. *IEEE International Conference on Innovations in Green Energy 2017, IGEHT 2017*, 1–7. https://doi.org/10.1109/IGEHT.2017.8094080

Janssens, O., Noppe, N., Devriendt, C., Walle, R. Van de, & Hoecke, S. Van. (2016). Data-driven multivariate power curve modeling of offshore wind turbines. *Engineering Applications of Artificial Intelligence*, *55*, 331–338. https://doi.org/10.1016/j.engappai.2016.08.003

Jayanthi, P., & Devaraj, D. (2019a). Enhancement of LVRT Capability in Grid Connected Wind Energy Systems using Crowbar. *2019 International Conference on Clean Energy and Energy Efficient Electronics Circuit for Sustainable Development, INCCES 2019*, 3–7. https://doi.org/10.1109/INCCES47820.2019.9167746

Jayanthi, P., & Devaraj, D. (2019b). Performance Study of DFIG Based Grid Connected WECS using Crowbar and Without Crowbar. *IEEE International Conference on Intelligent Techniques in Control, Optimization and Signal Processing, INCOS 2019*, 1–3. https://doi.org/10.1109/INCOS45849.2019.8951426

Jimenez Garibay, A., Juvenal Rodriguez-Resendiz, J. R. R., & Jauregui Correa, J. (2018). Analysis of Rotor Current Impact on DFIG-WECS under Fault Condition. *IEEE Latin America Transactions*, *16*(2), 329–334. https://doi.org/10.1109/TLA.2018.8327383

Johari, M. K., Jalil, M. A. A., & Shariff, M. F. M. (2018). Comparison of horizontal axis wind turbine (HAWT) and vertical axis wind turbine (VAWT). *International Journal of Engineering and Technology(UAE)*, *7*(4), 74–80. https://doi.org/10.14419/ijet.v7i4.13.21333

Karad, S., & Thakur, R. (2021). Recent Trends of Control Strategies for Doubly Fed Induction Generator Based Wind Turbine Systems: A Comparative Review. *Archives of Computational Methods in Engineering*, *28*(1), 15–29. https://doi.org/10.1007/s11831-019-09367-3

Kumar, A. (2013). *Study on Dynamic Performance of Grid Connected Double Fed Induction Generator*.

Kumar, V., Pandey, A. S., & Sinha, S. K. (2020). Stability improvement of DFIG-based wind farm integrated power system using ANFIS controlled STATCOM. *Energies*, *13*(18), 1–18. https://doi.org/10.3390/en13184707

Kumhar, A. R. (2018). Vector Control Strategy to Control Active and Based Wind Energy Conversion system. *2018 2nd International Conference on Trends in Electronics and Informatics (ICOEI), Icoei*, 1–9.

Kuzhali, M., Joyal Isac, S., & Poongothai, S. (2019). Improvement of Low Voltage Ride Through Capability of Grid-Connected DFIG WTs Using Fuzzy Logic Controller. In *Advances in Intelligent Systems and Computing* (Vol. 846). Springer Singapore. https://doi.org/10.1007/978-981-13-2182-5_33

Liu, R., Yao, J., Wang, X., Sun, P., Pei, J., & Hu, J. (2020). Dynamic stability analysis and improved LVRT Schemes of DFIG-Based wind turbines during a symmetrical fault in a weak grid. *IEEE Power Electronics*, *35*(1), 303–318. https://doi.org/10.1109/TPEL.2019.2911346

Madan, C. J., & Kumar, N. (2019). Fuzzy grey wolf optimization for controlled low-voltage ride-through conditions in grid-connected wind turbine with doubly fed induction generator. *Simulation*, *95*(4), 327–338. https://doi.org/10.1177/0037549718777607

Mengistu, A. (2017). *Analaysis of Dynamic voltage stability on the penetration of Adama II Wind farm in Ethiopia grid*.

Merahi, F., & Berkouk, E. M. (2016). DC-BUS IMBALANCE MINIMIZATION FOR WIND ENERGY CONVERSION SYSTEM WITH FIVE-LEVEL BACK-TO-BACK CONVERTERS USING FUZZY LOGIC. *Renewable Energy*, *60*(7), 137–149. https://doi.org/10.1016/j.renene.2013.05.001

Mohammadi, J., Afsharnia, S., Ebrahimzadeh, E., Mohammadi, J., Afsharnia, S., Ebrahimzadeh, E., & Blaabjerg, F. (2017). An Enhanced LVRT Scheme for DFIG-based WECSs under Both Balanced and Unbalanced Grid Voltage Sags. *Electric Power Components and Systems*, *0*(0), 1–12. https://doi.org/10.1080/15325008.2017.1333547

Muluneh, Z., & Teame, G. (2021). Dynamic Modeling and Performance Analysis of PMSG- based Variable Speed WTG: Case Study of Adama Wind Farm I, Ethiopia. *Momona Ethiopian Journal of Science*, *12*(2), 155–172. https://doi.org/10.4314/mejs.v12i2.1

Naderi, S. B., Negnevitsky, M., & Muttaqi, K. M. (2019). A Modified DC Chopper for Limiting the Fault Current and Controlling the DC-Link Voltage to Enhance Fault Ride-Through Capability of Doubly-Fed Induction-Generator-Based Wind Turbine. *IEEE Transactions on Industry Applications*, *55*(2), 2021–2032. https://doi.org/10.1109/TIA.2018.2877400

Nafar, A., Arab Markadeh, G. R., Elahi, A., & Pouraghababa, R. (2016). Low Voltage Ride Through Enhancement Based on Improved Direct Power Control of DFIG under Unbalanced and Harmonically Distorted Grid Voltage. *University of Mohaghegh Ardabili*, *4*(1), 16–28. http://joape.uma.ac.ir/article_424.html

Noureldeen, O., & Hamdan, I. (2018). An efficient ANFIS crowbar protection for dfig wind turbines during faults. *2017 International Middle-East Power Systems Conference, MEPCON , 2018-Febru*(December), 263–269. https://doi.org/10.1109/MEPCON.2017.8301192

Rached, B., Elharoussi, M., & Abdelmounim, E. (2019). Fuzzy logic control for wind energy conversion system based on DFIG. *2019 International Conference on Wireless Technologies, Embedded Systems, WITS 2019*, *2*(1), 1–6. https://doi.org/10.1109/WITS.2019.8723722

Rao, V. V., & Nanajee, K. (2016). DC-BUS IMBALANCE MINIMIZATION FOR WIND ENERGY CONVERSION SYSTEM WITH FIVE-LEVEL BACK-TO-BACK. *International Journal of Industrial Electronics and Electrical Engineering, ISSN*, *4*(7), 2347–6982.

Rashid, G., & Hasan, M. (2017). Fault ride through capability improvement of DFIG based wind farm by fuzzy logic controlled parallel resonance fault current limiter. *Electric Power Systems Research*, *146*, 1–8. https://doi.org/10.1016/j.epsr.2017.01.018

Rekioua, D. (2014). *Wind Power Electric Systems*.

Rezaie, B., Nikoo, S. Y., & Rahmani, Z. (2018). A novel intelligent fast terminal sliding mode control for a class of nonlinear systems: application to atomic force microscope. *International Journal of Dynamics and Control*, *6*(3), 1335–1350. https://doi.org/10.1007/s40435-017-0376-9

Salem Molla. (2021). *Fault ride through capability analysis of wind turbine with double fed induction generator*.

Shukla, R. D., & Tripathi, R. K. (2012). Low voltage ride through (LVRT) ability of DFIG based wind energy conversion system-I. *2012 Students Conference on Engineering and Systems, SCES 2012*. https://doi.org/10.1109/SCES.2012.6199113

Singh, N. (2015). *Modeling of DFIG Based Wind Turbine Mitigating Dynamic Behavior under Varying Load and Asymmetrical Fault Conditions*. *32*.

Sitharthan, R., Sundarabalan, C. K., Devabalaji, K. R., Nataraj, S. K., & Karthikeyan, M. (2018). Improved fault ride through capability of DFIG-wind turbines using customized dynamic voltage restorer. *Sustainable Society, 39*, 114–125. https://doi.org/10.1016/j.scs.2018.02.008

Sourkounis, C., & Tourou, P. (2013). Grid Code Requirements for Wind Power Integration in Europe. *Conference Papers in Energy*, *2013*, 1–9. https://doi.org/10.1155/2013/437674

Thapa, K. J. and K. (2021). An Enhanced Low Voltage Ride-Through Control Scheme of a DIFG based WTG Using Crowbar and Braking Chopper. *Journal of the Institute of Engineering*, *16*(1), 61–67.

Tohidi, S., & Behnam, M. I. (2016). A comprehensive review of low voltage ride through of doubly fed induction wind generators. *Renewable and Sustainable Energy Reviews*, *57*, 412–419. https://doi.org/10.1016/j.rser.2015.12.155

Tripathi, P. M., Sekhar Sahoo, S., & Chatterjee, K. (2019). Enhancing the fault ride through capability of DFIG-based wind energy system using saturated core fault current limiter. *The Journal of Engineering*, *2019*(18), 4916–4921. https://doi.org/10.1049/joe.2018.9296

Tuka, M. B., & Leidhold, R. (2017). Modeling and Control of a Doubly Fed Induction Generator Using a Back-to-Back Converters in Grid Tied Wind Power System. *IEEE PEC- IAS PowerAfrica*, 75–80.

Vats, S., Sahoo, S. S., Tripathi, P. M., & Chatterjee, K. (2018). LOW VOLTAGE RIDE

THROUGH ENHANCEMENT OF DFIG BASED WECS USING FLUX CONTROL. *2018 4th International Conference on Recent Advances in Information Technology (RAIT)*, 1–6.

Vivek, C. M. (2017). A Review on Vertical and Horizontal Axis Wind Turbine. *International Research Journal of Engineering and Technology*, *September*, 247–250. www.irjet.net

Xiao, F., Zhang, Z., & Yin, X. (2015). Fault current characteristics of the DFIG under asymmetrical fault conditions, *8*(10), 10971–10992. https://doi.org/10.3390/en81010971

Zheng, Z., Yang, G., & Geng, H. (2013). *Coordinated Control of a Doubly-Fed Induction Generator-Based Wind Farm and a Static Synchronous Compensator for Low Voltage Ride-through Grid Code Compliance during Asymmetrical Grid Faults*. *6*(Dc), 4660–4681. https://doi.org/10.3390/en6094660

APPENDICES

Appendix A

Table A.1: ADAMA-II Generator and Wind Turbine Parameters

Parameters	Value
Rated Power	1.5MW
Rated Stator Line to Line Voltage	690V
Rated Mechanical Torque	8292N-m
Frequency	50Hz
DC Link Voltage	1150V
Number of Poles	2
Transformer Ratio, u	0.42
Gear Box Ratio	94.7
Cpmax	0.4865
Lambda Optimum	9
Inertia	67
Blade Length	37.8m
Stator Winding Resistance, Rs	0.006243Ω
Rotor Winding Resistance, Rr	0.011074Ω
Stator Leakage Inductance, Lls	0.00008674H
Rotor Leakage Inductance, Llr	0.0000723H
Magnetizing Inductance, Lm	0.0055H

Appendix B

The parameters for the PI controllers are obtained by using equations (4.23), (4.32), and (4.39), which are computed with the MATLAB code in Appendix F. Table B.1 illustrates the gains of PI controllers for rotor current, grid current, and DC link voltage.

Table B.1: Parameters for PI Controllers

Parameters	Values
Kp_ir	2.2037
Kp_ig	0.3042
Kp_v	9.4248
Ki_ir	7776
Ki_ig	49.3480
Ki_v	1480
Kt_ir	3529
Kt_ig	162.3
Kt_v	157
Cbus	0.015F
Rf	0.01Ω
Lf	0.0005H
Rcrow	0.11074Ω

Appendix C

Table C.1: Parameters for ANFIS Structure

Parameters	Values
Number of inputs	1
Number of outputs	1
Number of rules	7
Number of epochs/ iterations	100
Total number of training data	250
Number of input MF	7
Types of input MF	Triangular
Number of output MF	7
Type of Inference system	Sugeno
Optimization Method	Hybrid

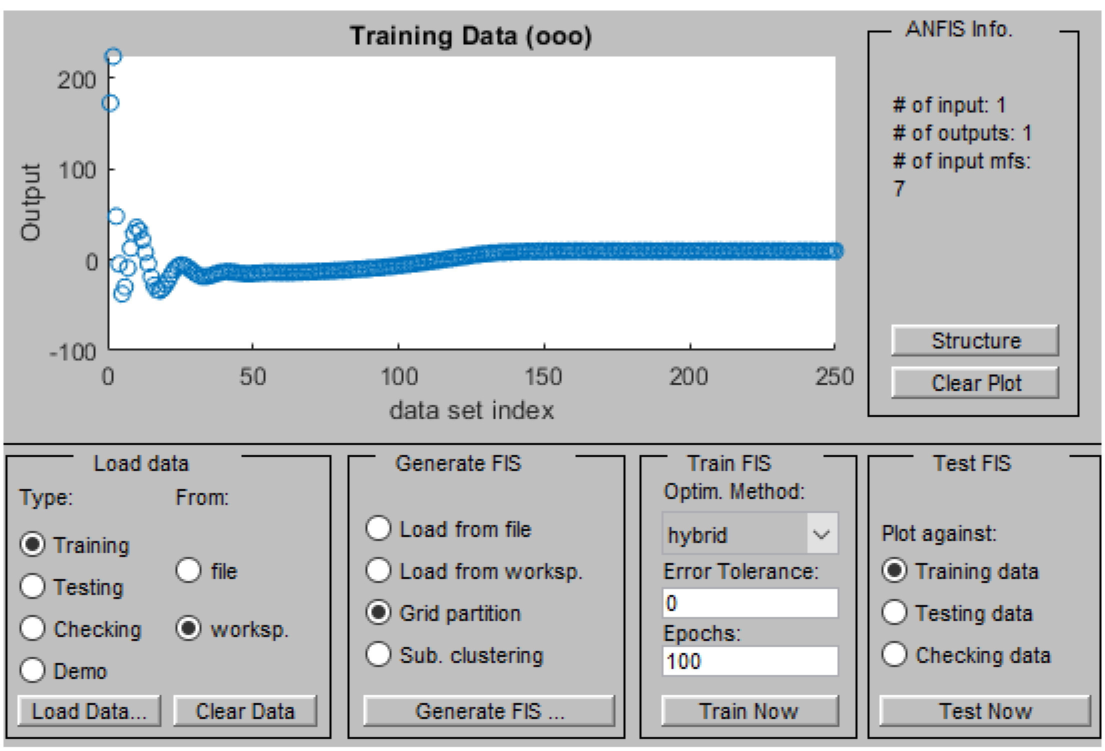

Figure C.1: Training Data for the Proposed ANFIS Controller

Appendix D

Reference Frame Transformation

Inverse Clark's transformation

It is the conversion of a two-phase stationary frame of reference (α, β) to a three-phase (abc). It's written in the matrix as (Abad, 2017):

$$\begin{bmatrix} x_a \\ x_b \\ x_c \end{bmatrix} = Tc^T \begin{bmatrix} x_\alpha \\ x_\beta \\ x_0 \end{bmatrix} \tag{D.1}$$

Where, $Tc^T = \begin{bmatrix} 1 & 0 & 1 \\ \frac{-1}{2} & \frac{\sqrt{3}}{2} & 1 \\ \frac{-1}{2} & \frac{-\sqrt{3}}{2} & 1 \end{bmatrix}$

The inverse of Park's transformation

It is the transformation of two-phase rotating frames of reference (dq) into two-phase stationary frames of reference (α, β). It is represented in the matrix as (Abad, 2017):

In the matrix, it's written as:

$$\begin{bmatrix} x_\alpha \\ x_\beta \end{bmatrix} = Ta^T \begin{bmatrix} x_d \\ x_q \end{bmatrix} \tag{D.2}$$

Where, $Ta^T = \begin{bmatrix} C\theta & -S\theta \\ S\theta & C\theta \end{bmatrix}$

There is also a direct transformation from the dq frame of reference to the three phase and vice versa using the following transformation matrixes (Abad, 2017).

- abc to dq transformation:

$$\begin{bmatrix} x_d \\ x_q \\ x_0 \end{bmatrix} = \frac{2}{3}\begin{bmatrix} C\theta & C(\theta-\frac{2\pi}{3}) & C(\theta+\frac{2\pi}{3}) \\ -S\theta & -S(\theta-\frac{2\pi}{3}) & -S(\theta+\frac{2\pi}{3}) \\ \frac{1}{2} & \frac{1}{2} & \frac{1}{2} \end{bmatrix}\begin{bmatrix} x_a \\ x_b \\ x_c \end{bmatrix} \tag{D.3}$$

- dq to abc transformation:

$$\begin{bmatrix} x_a \\ x_b \\ x_c \end{bmatrix} = \begin{bmatrix} C\theta & -S(\theta) & 1 \\ C(\theta-\frac{2\pi}{3}) & -S(\theta-\frac{2\pi}{3}) & 1 \\ C(\theta+\frac{2\pi}{3}) & -S(\theta+\frac{2\pi}{3}) & 1 \end{bmatrix}\begin{bmatrix} x_d \\ x_q \\ x_0 \end{bmatrix} \tag{D.4}$$

Appendix E

MATLAB Simulink Models

Wind Turbine Model

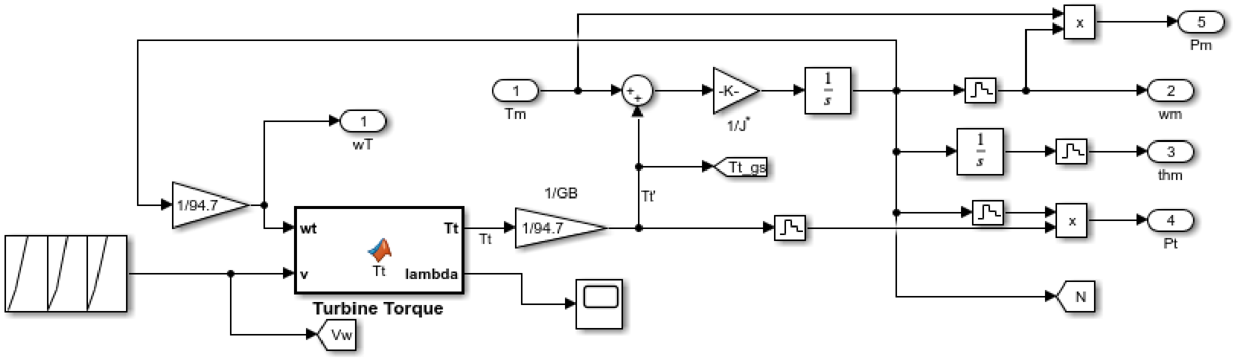

Figure E.1: WT Model

Rotor Side Converter (RSC) Control

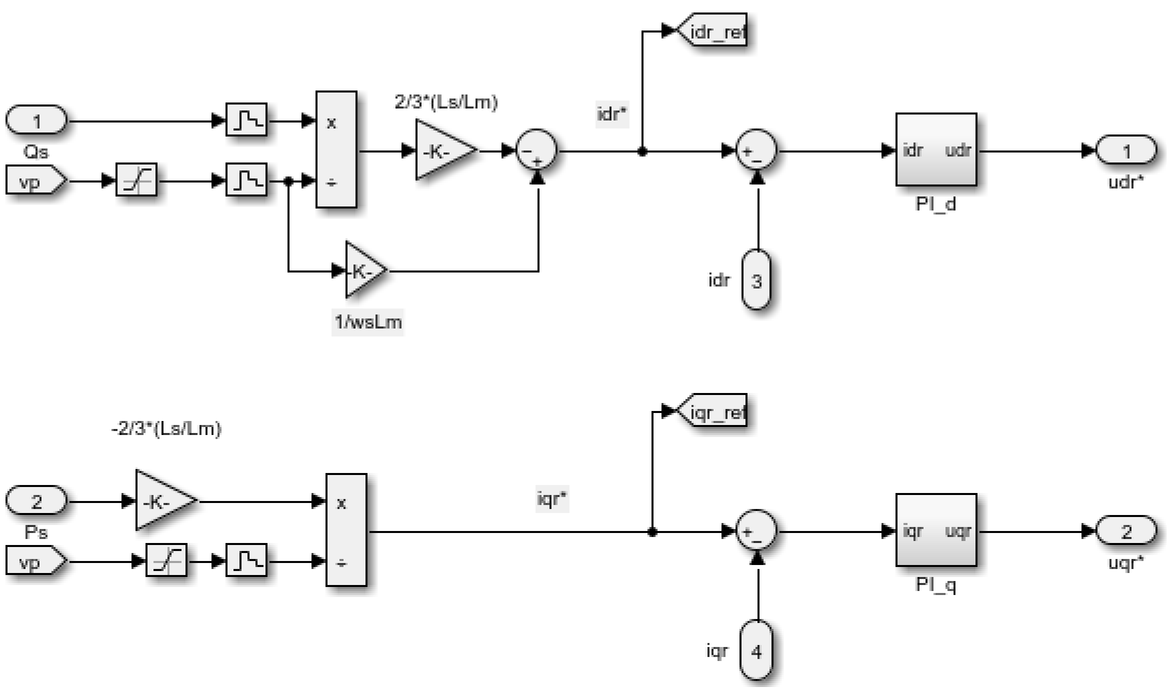

Figure E.2: RSC Control

Grid Side Converter (GSC) Control

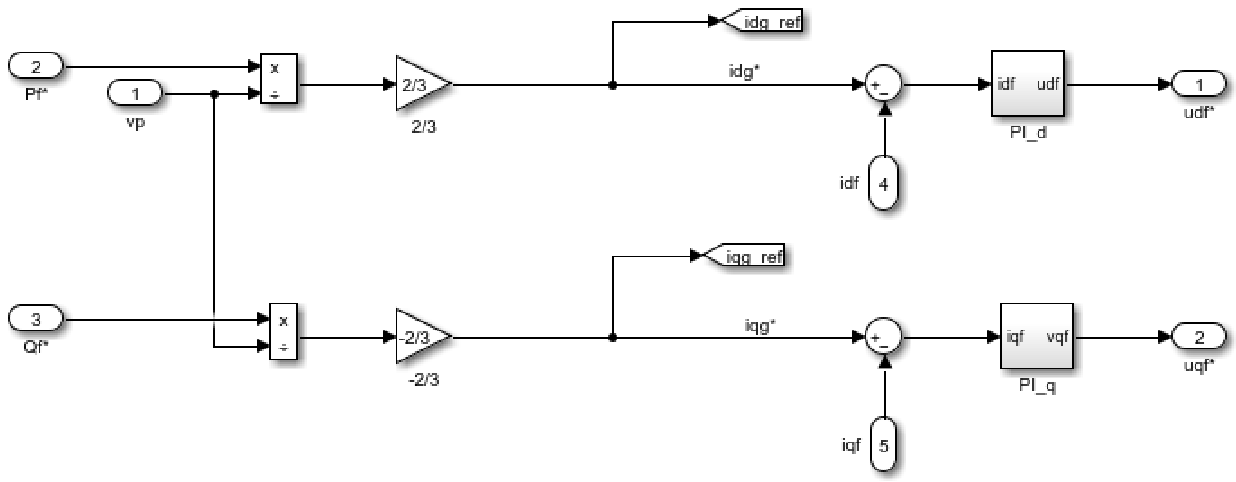

Figure E.3: GSC Control

Appendix F

Matlab Code

```
f=50;
Rs=0.006243;
Rr=0.011074;
Lm=0.0055;
Lls=0.00008674;
Llr=0.0000723;
Ls=Lls+Lm;
Lr=Llr+Lm;
Rf=0.01;
Lf=0.0005;
C=0.015;
%Rotor side converter PI controller
sigma=1-Lm^2/(Ls*Lr);
tau_i=(sigma*Lr)/Rr;
wni=100*(1/tau_i);
kp_ird=(2*wni*sigma*Lr)-Rr;
kp_irq=kp_ird;
ki_ird=(wni^2)*sigma*Lr;
ki_irq=ki_ird;
%Grid side converter PI controller
wng=2*pi*50;
kp_idg=(2*wng*Lf)-Rf;
kp_iqg=kp_idg;
ki_idg=(wng^2)*Lf;
ki_iqg=ki_idg;
kp_v=2*wng*C;
ki_v=(wng^2)*C;
```